Radiation Hardness Study of AlGaN/GaN High Electron Mobility Transistors (HEMTs)

by

Min Prasad Khanal

A dissertation submitted to the Graduate Faculty of
Auburn University
in partial fulfillment of the
requirements for the Degree of
Doctor of Philosophy

Auburn, Alabama
May 5, 2019

Keywords: AlGaN/GaN HEMTs, Radiation effects, Proton/Gamma irradiation, Photocurrent, Optical & Electrical, Defects

Approved by

Minseo Park, Chair, Professor of Physics
Michael Bozack, Emeritus Professor of Physics
Sarit Dhar, Associate Professor of Physics
Ayayi C. Ahyi, Associate Research Professor of Physics
Guofu Niu, Alumni Professor of Electrical and Computer Engineering

Abstract

Gallium nitride (GaN) has unique inherent properties such as ionic-covalent bond, large direct bandgap, excellent thermal stability, high threshold displacement energy and higher breakdown field. Also, the relatively low phonon loss and a high threshold for electron-hole pair generation upon ionizing radiation make GaN and its alloys a prominent candidate for the applications in a high radiation environment. Aluminum gallium nitride/gallium nitride (AlGaN/GaN) heterostructure system possesses a unique interface driven characteristic with high electron density and high mobility at the interface which gives additional radiation hardness to the AlGaN/GaN system. The study of gamma-ray and proton irradiation provides better insight into device response and defect creation for practical applications of AlGaN/GaN HEMTs in radiation environments.

In this work, a detailed investigation was performed on the direct-current (dc) electrical performance and optical characteristics of pristine and irradiated AlGaN/GaN HEMTs with 120 MRad dose of ^{60}Co-gamma-rays (γ-rays) in one experiment, and 100 keV protons with fluences 1×10^{10}, 1×10^{12}, and 1×10^{14} protons/cm^2 in another. A slight degradation of dc characteristics was observed for the devices fabricated on gamma-ray irradiated HEMT epi-layers, indicating the presence of radiation-induced defects. No additional irradiation induced strain was detected from comparing the Raman peak frequency position of pristine and irradiated samples. However, full-width-at-half-maximum (FWHM) of the Raman and near-band-edge PL peaks increased after irradiation, which suggests the degradation of crystal quality. The spectroscopic photocurrent-voltage (SPIV) study with sub-bandgap and above bandgap illumination confirmed the pre-existence of sub-

bandgap defects in the heterostructure and revealed the possibility of their re-arrangement or the introduction of new defects after gamma-ray irradiation.

Proton irradiation-induced effects on HEMTs was studied by emulating a certain space radiation environment using relatively low energy (100 keV) proton beam. Proton irradiation-induced sub-gap traps were detected by SPIV measurements. Raman study revealed that proton irradiation had induced strain relaxation on the HEMTs epi-layers. No substantial change in the crystal quality of epi-layers was indicated from Raman and PL studies. Charge carrier density was increased for the samples irradiated with 1×10^{12} and 1×10^{14} protons/cm^2 fluences, estimated *via* Raman spectroscopy and the charge-control model analysis. The magnitude and direction of transistor threshold voltage shift were also dependent on proton fluence. Overall, degradation of transistor output characteristics of the fabricated HEMTs was observed as the proton fluence increased.

Based on the level of performance of the irradiated devices, it was concluded that AlGaN/GaN HEMTs is relatively resistant to high dose (120 MRad) gamma-ray irradiation, but it can introduce additional traps or re-configure the pre-existing traps, and affect the electrical and optical characteristics of HEMTs. Additionally, the relative degree of influence on the material/device characteristics by 100 keV protons was not severe. Therefore, it can be suggested that the AlGaN/GaN HEMTs have high endurance for exposure to relatively high fluences of low-energy proton beams.

Acknowledgments

I indeed consider myself more than fortunate to have had the opportunity to pursue research work towards the Ph.D. with Professor Minseo Park. He always has guided me to become a successful and competent professional in every aspect of research and life. All of the many great tips and tools of knowledge I have gained will stick with me forever. Having the opportunity to work with Dr. Park taught me to become an independent researcher, excellent multitasker, and a project leader. I always had the opportunity to do experiments on my thoughts, to write my ideas down, and to share them with the world. This work would not have been possible without his endless encouragement and assistance which has been of immense value.

My special thank goes to Prof. Ayayi Claude Ahyi for his generous help and enlightened scientific discussions and also being a committee member. Without his support in experimental designs and software setups, my research would not have been possible. I am also indebted to the other members of my advisory committee: Prof. Michael Bozack, Prof. Sarit Dhar, and Prof. Guofu Niu. Their significant contributions to this work are greatly appreciated. I am honored to have been associated with such an eminent committee. Prof. Michael Bozack owes my appreciations for his valuable time spent to conduct XPS analysis on my samples and teaching me the software to analyze the results. I would also like to thank Mrs. Tamara Isaacs-Smith kindly who trained me in fabrication processes and device measurements and Max Chip Cichon who spent his valuable time in troubleshooting the instruments and conduct irradiation on my samples. I remember Henry Yang

who taught me lithography and device fabrication steps while I was starting my research. My appreciation goes to Prof. Sarit Dhar and Benjamin V. Schoenek for helping me to perform AFM analysis. I am also grateful to Prof. Tae-Sik Oh and Ehsan Hassani for their support in XRD experiment and analysis and Mr. Naresh Shahi for his help in SEM experiment.

I want to thank everybody with whom I have shared my experiences in life. Especially to those who with the gift of their company made my days more enjoyable, pleasant and worth living when I was far from home.

I also would like to especially thank the faculty and staff members of Auburn University who have taught, trained, and helped me through my research and physics classes. I am tempted to individually thank all of my friends which, from my childhood until graduate school, have joined me. However, because the list might be unmanageable and by fear of leaving someone out, I will simply thank very much to you all. Some of the very helpful friends who have helped me in all the ways for completing this work at the earliest are Dr. Burcu Ozden, Dr. Vahid Mirkhani, Dr. Shiqiang Wang, Mr. Sunil Uprety, Dr. Kosala Yapabandara, Mr. Peter Traverso, Mr. Spencer Leblanc, Dr. Asanka Jayawardena, Mrs. Isanka U. Jayawardhena Mr. Kyunghyuk Kim and Mr. Mohammadtadghi Soroush.

Most importantly, my deepest appreciation and gratitude from the core of heart goes to my beloved parents Kashi Nath Khanal and Dev Kumari Khanal who gave me my name, my life and everything else in between. I love them and appreciate the efforts they have put into giving me the life I have now. They are the reason I did this; they are the reason I thrive on being better. Their pride for me is my main goal in life. I am grateful to my loving brothers Suresh Khanal and Dr.

Rabi Khanal for their endless and unconditional support since my childhood. I would also like to remember my sister-in-laws Kabita and Anuradha for being a part and contributing to my family.

I always felt overjoyed, rejoiced, blessed and relieved once I see your beautiful face my sweet daughter, Manavi Khanal. Manavi, I can't thank you enough for being in our lives. You are the most thankful person in my life, you are the source of encouragement, smile, and love. You had to miss your father most of the times when you wanted to play with, I am sorry sweetie. Please forgive me.

Last but not the least, most of all my appreciation and thank goes to my loving, supportive, encouraging and patient wife Laxmi Khanal, who unconditionally tolerated me all the time. She has always been most encouraging, supporting and motivating individual throughout everything and continues to be. There is no amount of thanks commendable when it comes to Laxmi; I am forever indebted.

There is really no measure of thanks adequate to express how grateful I am for all of you who have painstakingly guided, supported and encouraged me throughout my doctoral work. Nevertheless, I tried to express a few words.

Dedicated to my grandfather,
Ekdev Khanal

Table of Contents

List of Tables

List of Figures

List of Abbreviations

2DEG	2-Dimensional Electron Gas
ABX	Acceptor-Bound Exciton
AlGaN	Aluminum Gallium Nitride
AlN	Aluminum Nitride
BFOM	Baliga's Figure of Merit
BL	Blue Luminescence
BX	Bound Exciton
CCD	Charge-Coupled Device
C-V	Capacitance-Voltage
CVD	Chemical Vapor Deposition
DAP	Donor-Acceptor Pair
DBX	Donor-Bound Exciton
DC	Direct Current
DD	Displacement Damage
DI	Deionized
DLTS	Deep Level Transient Spectroscopy
FET	Field Effect Transistor
FOM	Figure of Merit
FWHM	Full-Width at Half Maximum

GaAs	Gallium Arsenide
GaN	Gallium Nitride
HEMTs	High Electron Mobility Transistors
HFET	Heterostructure Field Effect Transistor
IC	Integrated Circuit
InN	Indium Nitride
IR	Image Reversal
I-V	Current-Voltage
JFOM	Johnson's Figure of Merit
LED	Light Emitting Diode
LEEBI	Low Energy Electron Beam Irradiation
LO	Longitudinal Optical
LPMOCVD	Low-Pressure Metal Chemical Vapor Deposition
LPP	Longitudinal Phonon Plasmon
MBE	Molecular Beam Epitaxy
MESFET	Metal Semiconductor Field Effect Transistor
MFS	Minimum Feature Size
MIS	Metal-Insulator-Semiconductor
MOCVD	Metal Organic Chemical Vapor Deposition
MODFET	Modulation Doped Field Effect Transistor
MOSFET	Metal-Oxide-Semiconductor Field Effect Transistor

NBE	Near Band Edge
NIEL	Non-Ionizing Energy Loss
PL	Photoluminescence
PD	Penetration Depth
PPC	Persistent Photoconductivity
RTA	Rapid Thermal Annealing
rf	Radio Frequency
SBH	Schottky Barrier Height
Si	Silicon
SiC	Silicon Carbide
TCE	Trichloroethylene
TFT	Thin Film Transistor
TID	Total Ionizing Dose
TLM	Transmission Line Model
TO	Transverse Optical
UV	Ultra-Violet
WBGS	Wide Band Gap Semiconductor
XPS	X-ray Photoelectron Spectroscopy
XRD	X-ray Diffraction
YL	Yellow Luminescence
ZnO	Zinc Oxide

Chapter 1

Introduction

III-V nitride semiconductors such as GaN, InN, AlN, AlGaN have been considered as one of the most important groups of semiconductors beyond Si. III-V nitrides possess several intrinsic material properties such as a strong chemical bond[1], large direct bandgap[2], high displacement threshold energy[3], ultrafast carrier relaxation time[4], high breakdown field[5], and high electron mobility[6], which make them suitable for power electronic and optoelectronic applications. As a third-generation semiconductor, GaN and its alloys made a possible demonstration of the most efficient blue-laser diode[7] and the field effect transistor with highest output power density[8], as well as high temperature, high power, high frequency, and harsh radiation environment performance and many more, have been anticipated with growing power electronics market requirements.[9]

This thesis explores the radiation response and reliability of AlGaN/GaN High Electron Mobility Transistors (HEMTs) grown by metal-organic chemical vapor deposition (MOCVD). Electrical and optical characteristics of gamma-ray and proton irradiated HEMTs were analyzed. In this introductory chapter, a brief survey of radiation study performed on AlGaN/GaN HEMTs is outlined. To provide better insight into the practical space applications and other high radiation environments, a detailed systematic investigation was performed on irradiation-induced damage and defects.

The history of synthesis of GaN goes back to 1930s when Johnson *et al.*[10], Von R. Juza and Harry Hahn made the first attempt by flowing ammonia (NH_3) through gallium at high temperatures.[11] They produced small needles and platelets. Later in 1959, Grimmeiss and Koelmans used the same technique and could produce small crystals of GaN to study the photoluminescence

(PL) spectra.[12] Maruska and Tietjen in 1969 accomplished a breakthrough in the growth of single crystal GaN using chemical vapor deposition (CVD) technique.[13] In the early days of the 1960s and 1970s, GaN production methods suffered from heavy oxygen and water contamination. All the efforts to make GaN at that time have resulted in a highly conducting n-type material, even without doping, and encountered difficulties in p-type doping. Therefore, not much attention was paid to the matter until the 1980s.[14] GaN device fabrication again progressed after a turning point of successful growth of high-quality single crystal GaN by Asif Khan's group in 1983 using low-pressure metal organic chemical vapor deposition (LPMOCVD) technique[15] and by Yoshida *et al.* who reported an improvement in GaN growth quality using AlN as the buffer layer.[16] In 1986, Amano *et al.* reported the highly improved surface morphology, as well as optical and electrical properties of GaN films grown on sapphire substrates by MOCVD.[17] The buffer layer acted as a nucleation layer and decreased the interfacial free energy to facilitate two-dimensional growth by changing the properties of the surface. The doping of wide-bandgap materials encounters difficulty due to the probability of native defects formation that can dominate the electronic point defect chemistry. Intrinsically, GaN grows as n-type with a direct bandgap[2] of 3.47 eV; but to fabricate semiconductor devices, electronic properties must be controlled and controlling carrier concentration plays a major role. It was believed that the n-type nature of GaN was due to nitrogen vacancy's (V_N) donor behavior. The GaN community was facing difficulty in achieving a high conductivity p-type GaN. A big breakthrough was achieved on GaN study when Akasaki's group announced the low resistivity p-type GaN samples formed by activating Mg-doped sample with a low energy electron beam irradiation ((LEEBI) using a scanning electron microscope[18] in 1989. Later, Nakamura established a simple technique of thermal annealing in inert gas or vacuum environment to

improve the conductivity of p-type GaN.[19] The first nitride blue light emitting diode (LED) containing PN-junction was reported by Amano *et al.*[18] in 1989. And in 1991, Nakamura *et al.* prepared a bright and highly efficient blue LED using Mg-doped GaN as a buffer layer following the standard thermal annealing technique.[20] Since then, much work has been performed by Akasaki, Amano and Nakamura and their teams. In acknowledgment of their pioneering and tremendous work in this field, the Nobel Prize in Physics 2014 was awarded to all three of them.

The $Al_xGa_{1-x}N$ is an alloy of aluminum nitride (AlN) and GaN with aluminum molar fraction given by x. The reports[21,22] on the growth of AlGaN films can be found as early as 1977 and 1978. Following the progress in crystal growth techniques, the quality of AlGaN films was improved by adopting molecular beam epitaxy (MBE)[23] and MOCVD techniques.[24]After all these progresses on GaN and AlGaN crystal growth, in 1991, Khan *et al.*[25] reported the first evidence of a two-dimensional electron gas (2DEG) formation at an $Al_xGa_{1-x}N$/GaN heterojunction interface grown by MOCVD technique on a sapphire substrate. In 1993 and 1994, Khan *et al*. reported the GaN-based first metal semiconductor field-effect transistor (MESFET)[26] and heterostructure field-effect transistor (HFET)[27] on a sapphire substrate. Since then, GaN-based devices began to be fabricated more routinely, and excellent progress has been made in the development of GaN technology. GaN devices then faced the need of a more suitable substrate. In 2000, Kaiser *et al.* successfully transferred the AlGaN/GaN HEMT technology to silicon substrates using MOCVD techniques.[28] Nowadays, despite the challenges in managing the large lattice mismatch and thermal mismatch between GaN and Si, which can lead to more defects, crack-free GaN epitaxial films can be successfully grown on Si to manufacture power devices with low ON-resistance, low leakage, and small dynamic ON-resistance degradation.[29] The ability to grow GaN on Si facilitates the cost competitiveness of manufacturing power devices.

III-nitride compound semiconductor materials have large band gaps ranging from 3.4 eV to 6.1 eV and strong atomic bonds such as 8.92 eV/atom for GaN and 11.52 eV/atom[30] for AlN whereas Si, has 2.30 eV/atom.[31] The high bond strength, as well as remarkably high thermal and mechanical stability of these semiconductors confer them relatively high threshold displacement energy.[3] Wide bandgap of III-nitrides helps to minimize the problems associated with the unwanted optical or thermal generation of charge carriers. With all these advantageous material properties, GaN-based devices offer great potential for operations in a wide range of temperature[32, 33](-223ºC -1000ºC) and pressure (0-5 kbar)[34] and in harsh radiation environments. Therefore, these materials are viable to operate in extreme environments including vulnerable radiation exposure without the need for the cumbersome and expensive heating/cooling systems and/or radiation shielding.

The major focus of this research is on $Al_xGa_{1-x}N$/GaN heterostructures constructed as HFETs, also called HEMTs. A heterojunction, in general, is an interface composed of two different semiconductor materials. The difference in bandgaps of two materials in contact can lead to unique physical properties and can be exploited for particular applications. The heterojunction formed at the interface between AlGaN and GaN is featured for its unique properties such as high electron mobility and density. In a series of development from the first generation (Si/Ge) and second generation (GaAs/SiC) semiconductors, the power electronics industry has adopted Gallium Nitride as the most promising candidate. Among other promising, yet not completely developed III-N based technologies, AlGaN/GaN HEMTs have made significant progress over the past decades.[35] The wide bandgap, high breakdown field, high electron saturation velocity, high thermal conductivity, high gain, and high electron mobility enable AlGaN/GaN heterostructured devices to perform reliably in commercial and military applications which demand high voltage, high current,

high efficiency, high temperature, and high radiation tolerance.[8] Fig. 1.1 illustrates the potential applications of GaN-based power devices.

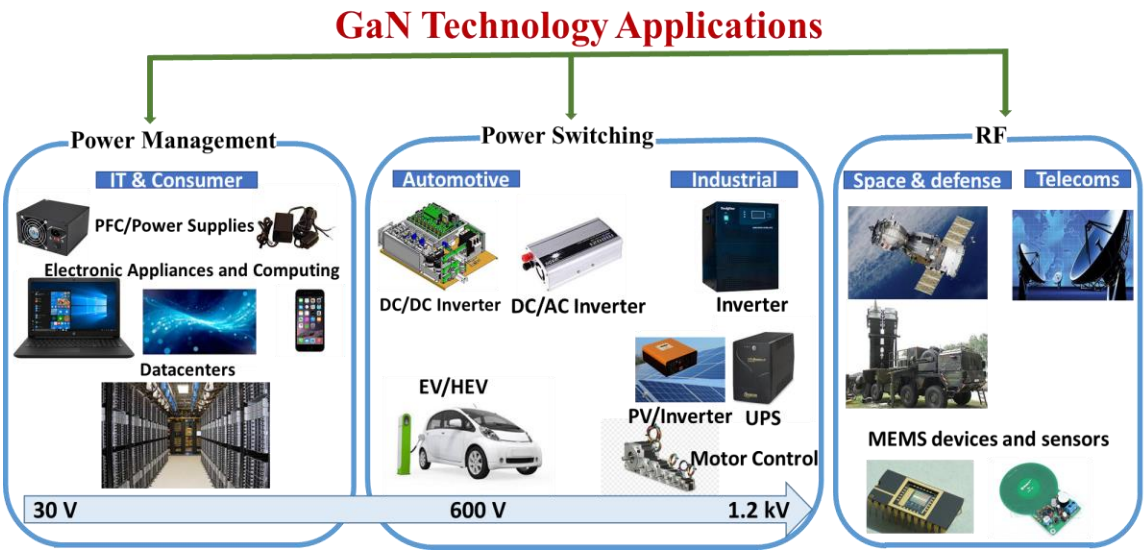

Fig. 1.1. Potential applications for GaN-based power devices.

As the current technology demands for the reliable study reports on potential semiconductors to be used in radiation environment as a part of space exploration and the terrestrial applications, the studies of radiation-induced effects on GaN-based devices have attracted a significant interest of the scientific community. Although there are quite a few reports published on the study of ionizing radiation effects, only a limited number of data exists on the non-ionizing radiation exposure study on AlGaN/GaN HEMTs. In various studies about the radiation effects by different groups, different techniques were employed to analyze the outcomes of the device level performance and irradiation-induced defects. The following table summarizes the prior and contemporary studies on radiation studies of GaN-based semiconductor devices.

Table 1.1: Summary of prior and contemporary state-of-the-art in radiation studies of GaN-based electronic devices.

Semiconductor materials and electronic devices	Radiation exposed to	Energy/Source	Dose/Fluence	Ref
AlGaN/InGaN/GaN commercial LEDs	Protons	2 MeV	2.31 ± 0.23 MRad/1.68×10^{12} cm^{-2}	[36]

GaN Film	Protons	2 MeV	10^{9}-10^{16} cm^{-2}	[37]
GaN/AlGaN/InGaN commercial blue LEDs	Protons	2 MeV	10^{11}-10^{15} cm^{-2}	[38]
InGaN LEDs	Protons	40 MeV	5×10^{9}-5×10^{10} cm^{-2}	[39]
AlGaN/GaN HEMTs	Protons	1.8 MeV	1×10^{14} cm^{-2}	[40]
AlGaN/GaN HEMTs	Protons	40 MeV	5×10^{9} and 5×10^{10} cm^{-2}	[41]
AlGan/GaN HEMTs	Protons	15, 40, and 105 MeV	Up to 10^{13} cm^{-2}	[42]
AlGaN/GaN HEMTs	Protons	3 and 6 MeV	Up to 5×10^{14} cm^{-2}	[43]
AlGaN/GaN HEMTs	Protons	5 MeV	2×10^{11} and 5×10^{14} cm^{-2}	[44]
AlGaN/GaN HEMTs	Protons	17 MeV	Up to 1×10^{16} cm^{-2}	[45]
AlGaN/GaN HEMTs	Protons	100 keV	$1 \times (10^{10}, 10^{12}, 10^{14}$ $cm^{-2})$	[46]
GaN Schottky diodes	Electrons	1 MeV	5×10^{15} cm^{-2}	[47]
AlGaN/GaN Schottky diodes	Electrons	1 MeV	5×10^{15} cm^{-2}	[48]
GaN/InGaN quantum wells	Electrons	10 MeV	10^{15}, $10^{16}$and 5×10^{16}-5×10^{17} cm^{-2}	[49]
AlGaN/GaN HFETs	Electrons	0.45 MeV	Up to 3.67×10^{15} cm^{-2}	[50]
AlGaN/AlN/GaN/Sapphire, AlGaN/GaN/Sapphire and AlGaN/GaN/ Si and In-AlN/GaN/Sapphire Hetero-junctions	Electrons	10 MeV	2×10^{15}-3.33×10^{16} cm^{-2}	[51]
GaN Film	Electrons	2.5 MeV	4×10^{18} cm^{-2}	[52]
GaN/AlGaN/InGaN commercial LEDs	Electrons	300-1400 keV	$(1\text{-}13) \times 10^{14}$ cm^{-2}	[3]
AlGaN/GaN HEMTs	Gamma-rays	^{60}Co	5, 30, 45 and 70 kRad	[53]
AlGaN/GaN	Gamma-rays	^{60}Co	Up to 10 MRad	[54]
InGaN quantum well LEDs	Gamma-rays	^{60}Co	150-2000 MRad (Si)	[55]
GaN Film	Gamma-rays	^{60}Co 700 keV and 0.9 keV	1.34×10^{19} cm^{-2}	[56]

		equivalent electrons		
AlGaN/GaN HEMTs	Gamma-rays	^{60}Co	Up to 600 MRad	[57]
GaN Schottky diodes	Gamma-rays	^{60}Co	21 MRad (Si)	[58]
GaN Film	Gamma-rays	^{60}Co	3×10^{19} cm^{-2}	[59]
AlGaN/GaN Schottky diodes	Gamma-rays	^{60}Co 1.33 MeV	Up to 1 MRad	[60]
AlGaN/GaN HEMTs	Gamma-rays	^{60}Co	120 MRad (Air)	[61]
GaN Schottky and Ohmic diodes	Neutrons	1 MeV	Up to 2.6×10^{16} cm^{-2}	[62]
GaN Schottky diodes	Neutrons	-	Up to 2.8×10^{16} cm^{-2}	[63]
AlGaN/GaN and AlIN/GaN HEMTs and MOS-HEMTs	Neutrons	-	1.6×10^{11} cm^{-2} and 6×10^{19} cm^{-2}	[64]
AlGaN/GaN, AlGaN/AlN/GaN and InAlN//GaN HEMTs	Neutrons	2 MeV	$1\text{-}3\times10^{15}$ cm^{-2}	[65]
AlGaN/GaN HFETs	Neutrons	1 MeV	Up to 6×10^{12} cm^{-2}	[66]
AlInN/GaN HEMTs	Neutrons	-	1.2×10^{12} cm^{-2}	[67]

As can be seen from Table I, III-nitrides have attracted significant interest in the radiation studies, and various types of radiation exposure have been tested for the device performance of GaN-based electronics. The main focus of the radiation-induced effects on III-nitrides is on protons, neutrons, electrons, and gamma-rays. For the development of semiconductor technology in the radiation hard electronic applications, the research is still not mature, and electronic devices still need to be tested with different aspects of radiation exposure in the real situation. Despite the remarkable advances in optoelectronic and power electronic device performances of GaN and III-nitride based HEMTs, further developments of the next generation GaN technology depend on

advances in areas such as novel materials and structures, growth and integration optimization, high-quality, low-cost substrates, device reliability, new device functionalities, *etc*. With regards to the reliability and the stability of AlGaN/GaN HEMTs, most of the different areas of research rely on the ability to suppress the crystal defects and to mitigate their effects in device performance. However, due to the lack of inexpensive large area GaN substrates, AlGaN/GaN HEMTs are usually grown on foreign substrates like sapphire[51, 9], Si, and SiC. Therefore, due to the lattice and thermal mismatch between the epi-layers and the foreign substrates, a high density of defect formation is possible in the epitaxial structures like AlGaN/GaN HEMTs. Researchers are trying to exploit polarization engineering to develop novel materials and structures based on unconventional crystal orientations to improve the device performance, reducing defect density and meeting specific application requirements. However, due to the novelty of the materials and difficulties in characterizing the defects, the required information about the presence, origin, and behavior of defects in these materials have not been widely reported and not fully understood.

Deep level defects on GaN-based devices can be created and/or modulated under the operational conditions, leading to the instability in performance or even catastrophic failure. Such an issue can be more severe when the AlGaN/GaN HEMTs are deployed for the applications in space crafts, communication satellites, as deep traps are created in the device as a result of exposure of the device to the high energy particle radiation in space. Deep level defects are mainly point defects such as Ga or N vacancies and also displacement damage can occur in the lattice.[68] Comprehensive understanding of the deep level defects and their role in device performance is essential for the further development of GaN technology.

This dissertation work intends to introduce a new technique called spectroscopic photocurrent-voltage (SPIV) to characterize the as grown defects across the nitride wafers and apply this

technique to identify how the high energy particle radiations can influence the spectral location and distribution of the deep level defects in AlGaN/GaN HEMTs. The main goal of this thesis is to fill in the gap for the information about defects characterization induced by high dose gamma-ray and low energy proton irradiations. Chapter 2 introduces the fundamental properties of GaN, its crystal structure and device physics of AlGaN/GaN HEMTs. In chapter 3, processes and physics of experimental techniques used for device processing and electrical characterization, is discussed in detail. Radiation environments, nature of radiation and the possible effect of radiation in electronics are explained in chapter 4. Chapter 5 is written to describe the material characterization techniques used in this dissertation work and their operational principles (including related physics) is presented in this chapter. Chapter 6 investigates the possible effects of high dose (120 MRad) gamma-ray irradiation on AlGaN/GaN HEMTs heterostructures. The effects of low energy (100 keV) protons, with three different fluences, on HEMTs were examined and the introduced defects were characterized. The results are presented in chapter 7. Finally, chapter 8 provides a summary of the analysis of the defect characterization of gamma-ray and proton irradiated HEMTs and presents a proposal for future directions.

References

[1] Trachenko, Kostya, J. M. Pruneda, Emilio Artacho, and Martin T. Dove. "How the nature of the chemical bond governs resistance to amorphization by radiation damage." *Physical Review B* 71, no. 18 (2005): 184104.

[2] Cimalla, V., J. Pezoldt, and O. Ambacher. "Group III nitride and SiC based MEMS and NEMS: materials properties, technology and applications." *Journal of Physics D: Applied Physics* 40, no. 20 (2007): 6386.

[3] Ionascut-Nedelcescu, A., C. Carlone, A. Houdayer, H. J. Von Bardeleben, J-L. Cantin, and S. Raymond. "Radiation hardness of gallium nitride." *IEEE Transactions on Nuclear Science* 49, no. 6 (2002): 2733-2738.

[4] Sun, C-K., Y-L. Huang, S. Keller, U. K. Mishra, and S. P. DenBaars. "Ultrafast electron dynamics study of GaN." *Physical Review B* 59, no. 21 (1999): 13535.

[5] Wu, Y-F., J. Gritters, L. Shen, R. P. Smith, and B. Swenson. "kV-class GaN-on-Si HEMTs enabling 99% efficiency converter at 800 V and 100 kHz." *IEEE transactions on power electronics* 29, no. 6 (2014): 2634-2637.

[6] Kyle, Erin CH, Stephen W. Kaun, Peter G. Burke, Feng Wu, Yuh-Renn Wu, and James S. Speck. "High-electron-mobility GaN grown on free-standing GaN templates by ammonia-based molecular beam epitaxy." *Journal of applied physics* 115, no. 19 (2014): 193702.

[7] Nakamura, Shuji, Masayuki Senoh, Shin-ichi Nagahama, Naruhito Iwasa, Takao Yamada, Toshio Matsushita, Hiroyuki Kiyoku, and Yasunobu Sugimoto. "InGaN multi-quantum-well-structure laser diodes with cleaved mirror cavity facets." *Japanese journal of applied physics* 35, no. 2B (1996): L217.

[8] Mishra, Umesh K., Primit Parikh, and Yi-Feng Wu. "AlGaN/GaN HEMTs-an overview of device operation and applications." *Proceedings of the IEEE* 90, no. 6 (2002): 1022-1031.

[9] Amano, H., Y. Baines, E. Beam, Matteo Borga, T. Bouchet, Paul R. Chalker, M. Charles et al. "The 2018 GaN power electronics roadmap." *Journal of Physics D: Applied Physics* 51, no. 16 (2018): 163001.

[10] Johnson, Warren C., J. B. Parson, and M. C. Crew. "Nitrogen compounds of gallium. iii." *The journal of physical chemistry* 36, no. 10 (1932): 2651-2654.

[11] Juza, Robert, and Harry Hahn. "Über die kristallstrukturen von Cu_3N, GaN und InN metallamide und metallnitride." *Zeitschrift für anorganische und allgemeine Chemie* 239, no. 3 (1938): 282-287.

[12] Grimmeiss, H. G., and H. Koelmans. "Über die Kantenemission und andere Emissionen des GaN." *Zeitschrift für Naturforschung* A 14, no. 3 (1959): 264-271.

[13] Maruska, H. P., and J. J. Tietjen. "The preparation and properties of vapor-deposited single-crystal-line GaN." *Applied Physics Letters* 15, no. 10 (1969): 327-329.

[14] Strite, S., and H. Morkoc. "GaN, AlN, and InN: a review J. Vac." *Sci. Technol. B* 10 (1992): 1237-66.

[15] Khan, M. Asif, R. A. Skogman, R. G. Schulze, and M. Gershenzon."Electrical properties and ion implantation of epitaxial GaN, grown by low pressure metalorganic chemical vapor deposition." *Applied Physics Letters* 42, no. 5 (1983): 430-432.

[16] Yoshida, S., S. Misawa, and S. Gonda. "Improvements on the electrical and luminescent properties of reactive molecular beam epitaxially grown GaN films by using AlN-coated sapphire substrates." *Applied Physics Letters* 42, no. 5 (1983): 427-429.

[17] Amano, Hi, N. Sawaki, I. Akasaki, and Y. Toyoda. "Metalorganic vapor phase epitaxial growth of a high quality GaN film using an AlN buffer layer." *Applied Physics Letters* 48, no. 5 (1986): 353-355.

[18] Amano, Hiroshi, Masahiro Kito, Kazumasa Hiramatsu, and Isamu Akasaki. "P-type conduction in Mg-doped GaN treated with low-energy electron beam irradiation (LEEBI)." *Japanese Journal of Applied Physics* 28, no. 12A (1989): L2112.

[19] Nakamura, Shuji, Masayuki Senoh, and Takashi Mukai. "Highly p-typed Mg-doped GaN films grown with GaN buffer layers." *Japanese journal of applied physics* 30, no. 10A (1991): L1708.

[20] Nakamura, Shuji, Takashi Mukai, and Masayuki Senoh. "High-power GaN pn junction blue-light-emitting diodes." *Japanese Journal of Applied Physics* 30, no. 12A (1991): L1998.

[21] J. Hagen, R. D. Metcalfe, W. Clark, and D. Wickenden, “Growth and properties of Ga x Al 1-x N compounds,” *J. Phys. C: Solid State Phys.*, vol. 11, no. 4, p. L143, 1978.

[22] Baranov, B., L. Däweritz, V. B. Gutan, G. Jungk, H. Neumann, and H. Raidt. "Growth and properties of AlxGa1–xN epitaxial layers." *physica status solidi (a)* 49, no. 2 (1978): 629-636.

[23] S. Yoshida, S. Misawa, and S. Gonda, “Properties of $Al_x Ga_{1-x} N$ films prepared by reactive molecular beam epitaxy,” *Journal of Applied Physics*, vol. 53, no. 10, pp. 6844–6848, Oct. 1982.

[24] Khan, M. Asif, R. A. Skogman, R. G. Schulze, and M. Gershenzon. "Properties and ion implantation of Al x Ga1− x N epitaxial single crystal films prepared by low pressure metalorganic chemical vapor deposition." *Applied Physics Letters* 43, no. 5 (1983): 492-494.

[25] Khan, M. Asif, J. M. Van Hove, J. N. Kuznia, and D. T. Olson. "High electron mobility GaN/Al x Ga1− x N heterostructures grown by low-pressure metalorganic chemical vapor deposition." *Applied Physics Letters* 58, no. 21 (1991): 2408-2410.

[26] Asif Khan, M., J. N. Kuznia, A. R. Bhattarai, and D. T. Olson. "Metal semiconductor field effect transistor based on single crystal GaN." *Applied Physics Letters* 62, no. 15 (1993): 1786-1787.

[27] Asif Khan, M., J. N. Kuznia, D. T. Olson, W. J. Schaff, J. W. Burm, and M. S. Shur. "Microwave performance of a 0.25 μm gate AlGaN/GaN heterostructure field effect transistor." *Applied Physics Letters* 65, no. 9 (1994): 1121-1123.

[28] Kaiser, S., M. Jakob, J. Zweck, W. Gebhardt, O. Ambacher, R. Dimitrov, A. T. Schremer, J. A. Smart, and J. R. Shealy. "Structural properties of AlGaN/GaN heterostructures on Si (111) substrates suitable for high-electron mobility transistors." *Journal of Vacuum Science & Technology B: Microelectronics and Nanometer Structures Processing, Measurement, and Phenomena* 18, no. 2 (2000): 733-740.

[29] Chen, Kevin J., Oliver Häberlen, Alex Lidow, Chun lin Tsai, Tetsuzo Ueda, Yasuhiro Uemoto, and Yifeng Wu. "GaN-on-Si power technology: Devices and applications." *IEEE Transactions on Electron Devices* 64, no. 3 (2017): 779-795.

[30] Pearton, S. J., J. C. Zolper, R. J. Shul, and F. Ren. "GaN: Processing, defects, and devices." *Journal of applied physics* 86, no. 1 (1999): 1-78.

[31] Dabrowski, Jarek. *Silicon surfaces and formation of interfaces: basic science in the industrial world*. World Scientific, 2000.

[32] Xue-Feng, Zhang, Wang Li, Liu Jie, Wei Lai, and Xu Jian. "Electrical characteristics of AlInN/GaN HEMTs under cryogenic operation." *Chinese Physics B* 22, no. 1 (2013): 017202.

[33] Khanna, Vinod Kumar. "Extreme-Temperature and Harsh-Environment Electronics; Physics, technology and applications." *Extreme-Temperature and Harsh-Environment Electronics; Physics, technology and applications, by Khanna, Vinod Kumar. ISBN: 978-0-7503-1156-4. IOP ebooks. Bristol, UK: IOP Publishing, 2017* (2017).

[34] Liu, Y., M. Z. Kauser, D. D. Schroepfer, P. P. Ruden, J. Xie, Y. T. Moon, N. Onojima, H. Morkoc, K-A. Son, and M. I. Nathan. "Effect of hydrostatic pressure on the current-voltage characteristics of Ga N⁄ Al Ga N⁄ Ga N heterostructure devices." *Journal of applied physics* 99, no. 11 (2006): 113706.

[35] Pengelly, Raymond S., Simon M. Wood, James W. Milligan, Scott T. Sheppard, and William L. Pribble. "A review of GaN on SiC high electron-mobility power transistors and MMICs." *IEEE Transactions on Microwave Theory and Techniques* 60, no. 6 (2012): 1764-1783.

[36] Osiński, M., P. Perlin, H. Schöne, A. H. Paxton, and E. W. Taylor. "Effects of proton irradiation on AlGaN/InGaN/GaN green light emitting diodes." *Electronics Letters* 33, no. 14 (1997): 1252-1254.

[37] Khanna, Shyam M., Jim Webb, Haipeng Tang, Alain J. Houdayer, and Cosmo Carlone. "2 MeV proton radiation damage studies of gallium nitride films through low temperature photoluminescence spectroscopy measurements." *IEEE Transactions on Nuclear Science* 47, no. 6 (2000): 2322-2328.

[38] Gaudreau, François, Cosmo Carlone, Alain Houdayer, and Shyam M. Khanna. "Spectral properties of proton irradiated gallium nitride blue diodes." *IEEE Transactions on Nuclear Science* 48, no. 6 (2001): 1778-1784.

[39] Khanna, Rohit, K. K. Allums, C. R. Abernathy, S. J. Pearton, Jihyun Kim, F. Ren, R. Dwivedi, T. N. Fogarty, and R. Wilkins. "Effects of high-dose 40 MeV proton irradiation on the electroluminescent and electrical performance of InGaN light-emitting diodes." *Applied physics letters* 85, no. 15 (2004): 3131-3133.

[40] Cai, S. J., Y. S. Tang, R. Li, Y. Y. Wei, L. Wong, Y. L. Chen, K. L. Wang et al. "Annealing behavior of a proton irradiated Al/sub x/Ga/sub 1-x/N/GaN high electron mobility transistor grown by MBE." *IEEE Transactions on Electron Devices* 47, no. 2 (2000): 304-307.

[41] Luo, B., J. W. Johnson, F. Ren, K. K. Allums, C. R. Abernathy, S. J. Pearton, R. Dwivedi et al. "DC and RF performance of proton-irradiated AlGaN/GaN high electron mobility transistors." *Applied Physics Letters* 79, no. 14 (2001): 2196-2198.

[42] Hu, Xinwen, Bo K. Choi, Hugh J. Barnaby, Daniel M. Fleetwood, Ronald D. Schrimpf, Sungchul Lee, S. Shojah-Ardalan, R. Wilkins, Umesh K. Mishra, and Ross W. Dettmer. "The energy dependence of proton-induced degradation in AlGaN/GaN high electron mobility transistors." *IEEE Transactions on Nuclear Science* 51, no. 2 (2004): 293-297.

[43] Lei, Zhifeng, Hongxia Guo, Minghua Tang, Chao Peng, Zhangang Zhang, Yun Huang, and Yunfei En. "Mechanism of high-fluence proton induced electrical degradation in AlGaN/GaN high-electron-mobility transistors." *Japanese Journal of Applied Physics* 57, no. 7 (2018): 074101.

[44] Lo, C. F., C. Y. Chang, B. H. Chu, H-Y. Kim, J. Kim, David A. Cullen, Lin Zhou et al. "Proton irradiation effects on AlN/GaN high electron mobility transistors." *Journal of Vacuum Science & Technology B, Nanotechnology and Microelectronics: Materials, Processing, Measurement, and Phenomena* 28, no. 5 (2010): L47-L51.

[45] Kim, Hong-Yeol, Jihyun Kim, Sang Pil Yun, Kye Ryung Kim, Travis J. Anderson, Fan Ren, and S. J. Pearton. "AlGaN/GaN high electron mobility transistors irradiated with 17 MeV protons." *Journal of the Electrochemical Society* 155, no. 7 (2008): H513-H515.

[46] Khanal, Min P., Sunil Uprety, Vahid Mirkhani, Shiqiang Wang, Kosala Yapabandara, Ehsan Hassani, Tamara Isaacs-Smith et al. "Impact of 100 keV proton irradiation on electronic and optical properties of AlGaN/GaN high electron mobility transistors (HEMTs)." *Journal of Applied Physics* 124, no. 21 (2018): 215702.

[47] Fang, Z-Q., Joseph W. Hemsky, David C. Look, and M. P. Mack. "Electron-irradiation-induced deep level in n-type GaN." *Applied physics letters* 72, no. 4 (1998): 448-449.

[48] Fang, Z-Q., Gary C. Farlow, B. Claflin, David C. Look, and D. S. Green. "Effects of electron-irradiation on electrical properties of AlGaN/GaN Schottky barrier diodes." *Journal of Applied Physics* 105, no. 12 (2009): 123704.

[49] Polyakov, A. Y., N. B. Smirnov, A. V. Govorkov, In-Hwan Lee, Jong Hyeob Baek, N. G. Kolin, V. M. Boiko, D. I. Merkurisov, and S. J. Pearton. "Electron Irradiation Effects in GaN⁄ InGaN Multiple Quantum Well Structures." *Journal of the Electrochemical Society* 155, no. 1 (2008): H31-H35.

[50] McClory, John W., James C. Petrosky, James M. Sattler, and Thomas A. Jarzen. "An analysis of the effects of low-energy electron irradiation of AlGaN/GaN HFETs." *IEEE Transactions on Nuclear Science* 54, no. 6 (2007): 1946-1952.

[51] Hwang, Ya-Shi, Lu Liu, Fan Ren, Alexander Y. Polyakov, N. B. Smirnov, A. V. Govorkov, E. A. Kozhukhova et al. "Effect of electron irradiation on AlGaN/GaN and InAlN/GaN heterojunctions." *Journal of Vacuum Science & Technology B, Nanotechnology and Microelectronics: Materials, Processing, Measurement, and Phenomena* 31, no. 2 (2013): 022206.

[52] Buyanova, I. A., Mt Wagner, W. M. Chen, B. Monemar, J. L. Lindström, H. Amano, and I. Akasaki. "Photoluminescence of GaN: Effect of electron irradiation." *Applied physics letters* 73, no. 20 (1998): 2968-2970.

[53] Hwang, Ya-Hsi, Yueh-Ling Hsieh, Lei Lei, Shun Li, Fan Ren, Stephen J. Pearton, Anupama Yadav et al. "Effect of low dose γ-irradiation on DC performance of circular AlGaN/GaN high electron mobility transistors." *Journal of Vacuum Science & Technology B, Nanotechnology and Microelectronics: Materials, Processing, Measurement, and Phenomena* 32, no.3 (2014): 031203.

[54] Jha, S., Emil V. Jelenković, M. M. Pejović, G. S. Ristić, M. Pejović, K. Y. Tong, C. Surya, Igor Bello, and W. J. Zhang. "Stability of submicron AlGaN/GaN HEMT devices irradiated by gamma rays." *Microelectronic Engineering* 86, no. 1 (2009): 37-40.

[55] Khanna, Rohit, Sang Youn Han, S. J. Pearton, D. Schoenfeld, W. V. Schoenfeld, and F. Ren. "High dose Co-60 gamma irradiation of InGaN quantum well light-emitting diodes." *Applied Physics Letters* 87, no. 21 (2005): 212107.

[56] Emtsev, V. V., V. Yu Davydov, V. V. Kozlovskii, V. V. Lundin, D. S. Poloskin, A. N. Smirnov, N. M. Shmidt et al. "Point defects in-irradiated n-GaN." *Semiconductor science and technology* 15, no. 1 (2000): 73.

[57] B. Luo *et al.*, "Influence of 60Co γ-rays on dc performance of AlGaN/GaN high electron mobility transistors," *Appl. Phys. Lett.*, vol. 80, no. 4, pp. 604–606, Jan. 2002.

[58] Umana-Membreno, G. A., J. M. Dell, G. Parish, B. D. Nener, L. Faraone, and U. K. Mishra. "^{60}Co gamma irradiation effects on n-GaN Schottky diodes." *IEEE Transactions on Electron Devices* 50, no. 12 (2003): 2326-2334.

[59] Shmidt, N. M., D. V. Davydov, V. V. Emtsev, I. L. Krestnikov, A. A. Lebedev, W. V. Lundin, D. S. Poloskin, A. V. Sakharov, A. S. Usikov, and A. V. Osinsky. "Effect of Annealing on Defects in As-Grown and γ-Ray irradiated n-GaN Layers." *physica status solidi (b)* 216, no. 1 (1999): 533-536.

[60] C. Sharma, R. Laishram, D. S. Rawal, S. Vinayak, and R. Singh, “Cumulative dose 60Co gamma irradiation effects on AlGaN/GaN Schottky diodes and its area dependence,” *AIP Conference Proceedings*, vol. 1942, no. 1, p. 120015, Apr. 2018.

[61] Khanal, Min P., Burcu Ozden, Kyunghyuk Kim, Sunil Uprety, Vahid Mirkhani, Kosala Yapabandara, Ayayi C. Ahyi, and Minseo Park. "Electrical and optical characteristics of gamma-ray irradiated AlGaN/GaN high electron mobility transistors." *Journal of Vacuum Science & Technology B, Nanotechnology and Microelectronics: Materials, Processing, Measurement, and Phenomena* 35, no. 3 (2017): 03D107.

[62] Katz, Evan J., Chung-Han Lin, Jie Qiu, Zhichun Zhang, Umesh K. Mishra, Lei Cao, and Leonard J. Brillson. "Neutron irradiation effects on metal-gallium nitride contacts." *Journal of Applied Physics* 115, no. 12 (2014): 123705.

[63] Lin, Chung-Han, Evan J. Katz, Jie Qiu, Zhichun Zhang, Umesh K. Mishra, Lei Cao, and Leonard J. Brillson. "Neutron irradiation effects on gallium nitride-based Schottky diodes." *Applied Physics Letters* 103, no. 16 (2013): 162106.

[64] Berthet, Fanny, Sébastien Petitdidier, Yannick Guhel, Jean Lionel Trolet, Philippe Mary, Christophe Gaquière, and Bertrand Boudart. "Influence of neutron irradiation on electron traps existing in GaN-based transistors." *IEEE Transactions on Nuclear Science* 63, no. 3 (2016): 1918-1926.

[65] Polyakov, A. Y., N. B. Smirnov, A. V. Govorkov, E. A. Kozhukhova, Stephen J. Pearton, Fan Ren, Lu Liu et al. "Comparison of neutron irradiation effects in AlGaN/AlN/GaN, AlGaN/GaN, and InAlN/GaN heterojunctions." *Journal of Vacuum Science & Technology B, Nanotechnology and Microelectronics: Materials, Processing, Measurement, and Phenomena* 30, no. 6 (2012): 061207.

[66] McClory, John W., and James C. Petrosky. "Temperature dependent electrical characteristics of neutron irradiated AlGaN/GaN HFETs." *IEEE Transactions on Nuclear Science* 54, no. 6 (2007): 1969-1974.

[67] Petitdidier, Sébastien, Yannick Guhel, Guillaume Brocero, Philippe Eudeline, Jean-Lionel Trolet, Patrick Mary, Christophe Gaquière, and Bertrand Boudart. "Influence of neutron irradiation on electron traps induced by NGB stress in AlInN/GaN HEMTs." *IEEE Transactions on Nuclear Science* 64, no. 8 (2017): 2284-2291.

[68] Pearton, S. J., F. Ren, Erin Patrick, M. E. Law, and Alexander Y. Polyakov. "Ionizing radiation damage effects on GaN devices." *ECS Journal of solid-state science and technology* 5, no. 2 (2016): Q35-Q60.

Chapter 2

Material Properties and Related Physics

2.1 Overview of GaN Material

2.1.1 Crystal Structure

GaN is a binary compound semiconductor and belongs to III-V semiconductor family. Wurtzite, zincblende, and rock salt are the three crystal structures that this wide bandgap (3.47 eV)[1] semiconductor exists in. The zinc-blende structure of GaN is metastable, and the rock salt structure can be produced only under very high pressure[2] of approximately 37 GPa. At high pressure, the wurtzite structure goes into structural phase transformation and converts to a six-fold coordinated rock salt structure. The lowest energy state for the bulk GaN does not exist in a cubic phase.[3] Therefore, the wurtzite structure is commonly abundant as it is thermodynamically stable at ambient conditions and easiest to grow. Among other forms of GaN, the wurtzite structure is preferred for research and technological applications. We focus our discussion on wurtzite structure in this work because our devices used for the research are of the wurtzite structure.

The general structure of the ideal wurtzite unit cell structure is hexagonal and consists of two interpenetrating hexagonal close-packed (HCP) lattice parameters a_0 and c_0 with their ratio: $c_0/a_0 = \sqrt{8/3} \cong 1.633$ where c is the height of a hexagonal cell.[4] The basis of a unit cell for the wurtzite GaN belong to four atoms, two being nitrogen and two gallium atoms as shown in Fig. 2.1 (a). In GaN crystal, Ga and N atoms are tetrahedrally bonded to four atoms (Ga & N). On the same plane, each side of the bonds are connected to the same type of atoms. Therefore, two distinct phases as shown in the schematics in Fig. 2.2, (Ga-face and N-face) of wurtzite GaN exist. The Ga-face corresponds to the [0001] and N-face corresponds to the $[000\bar{1}]$ of Miller indices.[5]

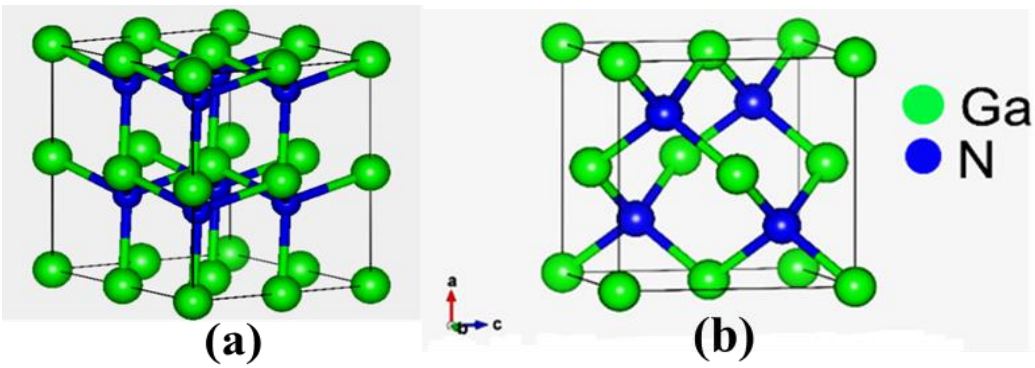

Fig. 2.1. Crystal structures of GaN: (a) wurtzite and (b) cubic zinc blende.

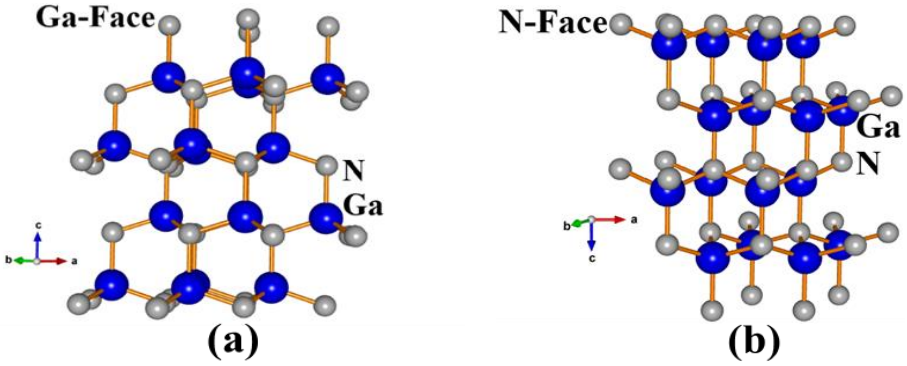

Fig. 2.2. Crystal structures of wurtzite GaN: (a) Ga- face polarity [0001] (b) N- face polarity [000$\bar{1}$]. The structures were generated by *VESTA*.[6]

Table 2.1 shows the summary of lattice parameters of wurtzite III-nitrides at 300 K. From the table; it is clear that the GaN is more close to the ideal wurtzite crystal structure compared to other III-nitrides. The degree of deviation from ideality determines the strength of polarization in III-nitrides.

Table 2.1: Structural parameters, thermal expansion coefficients and lattice mismatch with respect to common substrates of wurtzite III-nitrides[7] at 300 K.

Lattice Parameter		Ideal Crystal	AlN	GaN	InN
a_0 (Å)		-	3.112	3.189	3.54
c_0 (Å)		-	4.982	5.185	5.705
c_0/a_0 (expected)		-	1.601	1.625	1.611
c_0/a_0 (calculated)		1.633	1.619	1.633	1.627
Thermal expansion	α_a	-	4.2	5.59	5.7
cofficient (CTE) ($\times 10^{-6}$ K^{-1})	α_c		5.3	3.17	3.7
Lattice mismatch with (%)	α-Al_2O_3	-	12.5	14.8	25.4
	6H-SiC		1.0	3.3	14.0
	GaN		-2.4	-	10.6

2.1.2 Polarity of GaN Crystal

None of the three structures (wurtzite, zinc blende, and rock-salt) of GaN possess a center of inversion, *i.e.* in the closed packed plane, the position co-ordinates (x, y, z) is not invariant to the position ($-x$, $-y$, $-z$). As a result of the lack of inversion symmetry, the wurtzite GaN crystal exhibits two different polarity corresponding to (0001) (c-plane) and ($000\bar{1}$) (a-plane) basal planes. The polarity of the GaN depends on whether the Ga-atoms or N-atoms of GaN forming the crystal face the substrate. It has been studied that the two different polar faces have a vast difference in their growth and surface properties. When three of the bonds on Ga-atom with tetrahedral coordination face towards the substrate, the polarity is called Ga-face. Similarly, when three bonds face towards the growth direction, the polarity is called N-face as shown in Fig. 2.2. The growth and a variety of properties of the material such as etching, defect formation, plasticity, and piezoelectricity depend on its polarities. The crystal symmetry dictates the spontaneous polarization, the cubic zinc-blende structure forbids the spontaneous polarization, whereas the wurtzite structure permits it. On the other hand, both structures exhibit piezoelectric polarization. Since the c_0/a_0 ratios of AlN, GaN, and InN are not equal to the ideal value, and there is an absence of internal electric fields, in the absence of external fields, the total macroscopic polarization ($\boldsymbol{P}$) of a solid is given by the sum of spontaneous polarization ($\boldsymbol{P}_{sp}$) and the piezoelectric polarization ($\boldsymbol{P}_{pz}$).

2.1.3 Spontaneous Polarization

Spontaneous polarization arises due to the asymmetry of the wurtzite crystal. The lack of inversion symmetry of the wurtzite structure and the characteristics feature of the ionic bond between Ga and N atoms in GaN contributes to a naturally distorted crystal structure which exhibits a permanent polarization along the c-axis even in the absence of strain and external fields.[8] This

permanent polarization is recognized as spontaneous polarization ($\boldsymbol{P}_{sp}$). Since GaN wurtzite structure has two faces (Ga-face and N-face), the direction of spontaneous polarization is also different in those faces. In Ga-face structure, polarization has the direction away from the surface and towards the substrate whereas crystallographic c-axis and the internal electric field point away from the substrate towards the surface. The polarization-induced lattice charges are negative at the surface and positive at the substrate interface. On the other hand, for N-face structure, charges at the surface are positive and negative at the substrate interface, and the directions are inverted.

The magnitude of spontaneous polarization can be estimated using the sheet charge density for GaN to be -0.029 C/m^2 corresponding to ~3 MV/cm of the internal electric field.[9] The surface charge density caused by the spontaneous polarization is estimated to be in the order of 10^{13} cm^{-2}. The charges are fixed and are large enough to drastically affect the electrical properties of the material at surface and interfaces. The direct consequence of this large polarization and the corresponding surface density is the emergence of a large internal electric field which is hidden into the system as a result of crystal structure. This field has a strong influence on the band diagrams, charge accumulation and depletion, and band profile. Spontaneous polarization parameters for III-nitrides are listed in Table 2.2. For stable wurtzite III-nitride structures, the deviation in the structural deformation along the c-axis results in a large spontaneous polarization. As can be seen from Table 2.2, it is negative for all III-nitrides and the magnitude increases from GaN to InN to AlN following the deviation of c_0/a_0 ratio.

The spontaneous polarization can be estimated using the method below[9]; assuming that all the forces acting on a point charge are Coulombic, the distance between the top N atom and the central Ga atom (the bond length along c- axis) denoted by u_0 can be calculated in units of c_0 using the following equation:

$$\frac{3(0.5-u_0)c_0}{[{}^{a_0^2}/_{3}+(0.5-u_0)^2]^{\frac{3}{2}}} = \frac{1}{{u_0}^2{c_0}^2} \quad (2.1)$$

For the tetrahedron bonding, the net dipole moment is $Ze(u_0\text{-}0.375)c_0$, where Z is the effective charge of the metal atom. The net dipole moment per unit volume gives the polarization. In the case of unstrained material, this polarization is called spontaneous polarization ($\boldsymbol{P}_{sp}$) and is equal to;

$$P_{sp} = \frac{Ze(u_0-0.375)c_0}{\sqrt{3}{a_0}^2/_{24}} \quad (2.2)$$

Using a_0 and c_0 for GaN and from Table 2.1 and Z=3 for Ga the $\boldsymbol{P}_{sp}$ for GaN is estimated to be -0.029 C/m^2.

Table 2.2: Spontaneous polarization sheet charge density for III-nitrides.[10]

Material	AlN (Cm^{-2})	GaN (Cm^{-2})	InN (Cm^{-2})
P_{sp}	-0.081	-0.029	-0.032
P_{sp}	-0.090	-0.034	-0.042

In the case of AlGaN/GaN heterostructure, as mentioned above, Ga-face GaN and AlGaN will have a negative spontaneous polarization whereas the N-face materials will have positive $\boldsymbol{P}_{sp}$. Spontaneous polarization of ternary alloys can be calculated by the linear combination of binary endpoints with regard to mole fraction. Therefore considering, AlGaN follows the Vegard's law, the spontaneous polarization of $Al_xGa_{1-x}N$ can be expressed as;[11]

$$\overline{P_{AlGaN}^{SP}}(x) = x\overline{P_{AlN}^{SP}} + (1-x)\overline{P_{GaN}^{SP}} \quad (2.3)$$

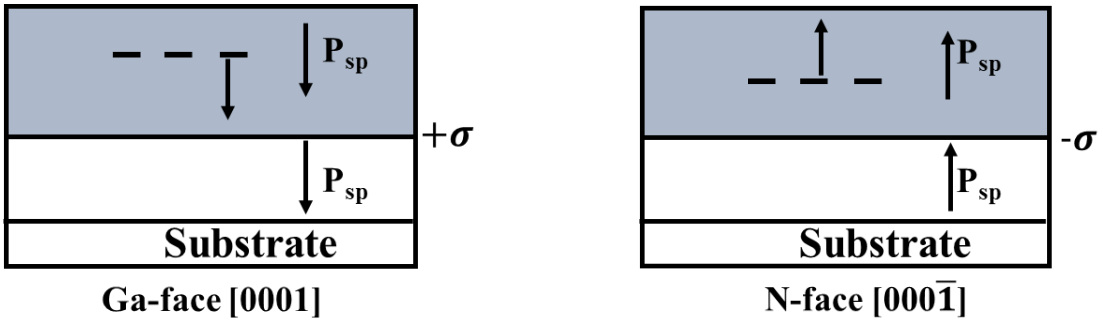

Fig. 2.3. Directions of polarizations in Ga- and N- faces relaxed AlGaN/GaN heterostructures.

2.1.4 Piezoelectric Polarization

Piezoelectric polarization ($\boldsymbol{P}_{pz}$) is the polarization field that results from the lattice distortion of the crystal induced by an externally applied stress and strain as a result of lattice mismatch during the epitaxial growth. While the spontaneous polarization is associated with a relaxed crystal, the applied external strain to the film would further change the net dipole moment, the lattice parameters a_0 and c_0 leading to the piezoelectric effect. Due to the differences in lattice constants of AlN, GaN, and AlGaN, growing AlGaN on GaN leads to tensile strain[12] in AlGaN resulting in a charge sheet at two faces of the crystal and the piezoelectric field will be in the same direction as the spontaneous polarization. In the case of compressive stress (increase in c_0/a_0 ratio), piezoelectric and spontaneous polarization will be in the opposite directions, therefore net polarization will be decreased. Similarly, in the case of tensile stress (decrease in c_0/a_0 ratio), the net polarization will be increased. The polarization field increases with the Al content in AlGaN.

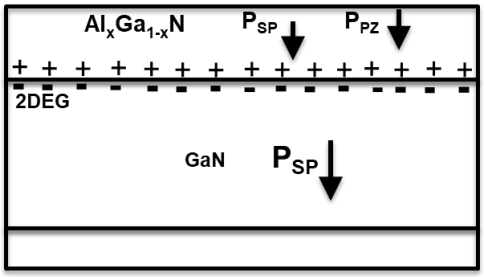

Fig. 2.4. Piezoelectric and spontaneous polarization fields for AlGaN grown on GaN.

The piezoelectric polarization of the crystal (***P**pz*) is given by the product of piezoelectric coefficients e_{ij} and stress tensor σ_{ij}. For wurtzite crystal structure along [0001] direction (*z*-axis), $\boldsymbol{P}_{pz}$ can simply be written as;

$$P_{pz} = e_{33}\varepsilon_z + e_{31}(\varepsilon_x + \varepsilon_x) \tag{2.4}$$

where ε_z is the strain along c-axis and $\varepsilon_x = \varepsilon_y$ *i*s an isotropic in-plane strain.

Strain components are related by the elastic coefficients by the relation:

$$\varepsilon_z = -2\varepsilon_x\,(c_{13}/c_{33}) \tag{2.5}$$

The in plain strain in terms of lattice constant is given by;

$$\varepsilon_x = \varepsilon_y = (a - a_0)/a_0 \tag{2.6}$$

where a is the in-plane lattice constant and a_0 is its equilibrium value.

Combining the above equations, the strain induced piezoelectric polarization along the *z*-axis of wurtzite III-V semiconductors is given by:

$$P_{pz} = 2(e_{31} - e_{33}\frac{c_{13}}{c_{33}})(a - a_0)/a_0 \tag{2.7}$$

Since e_{31} is always negative for wurtzite nitrides making $(e_{31} - e_{33}\frac{c_{13}}{c_{33}}) < 0$. Therefore, under tensile stress, the piezoelectric polarization is negative and positive for the compressive strain. Same as spontaneous polarization, the piezoelectric polarization for alloys can be obtained by linear interpolation of the moduli of the binary constituents. Thus, $\boldsymbol{P}_{pz}$ of AlGaN is given by;

$$Ppz(AlGaN) = x\,Ppz(AlN) + (1 - x)\,Ppz(GaN) \tag{2.8}$$

It is important to note that the piezoelectric polarization along [111] direction in zinc-blende III-V semiconductors has been studied in details,[13] but the low piezoelectric constants of the material system make the structure unattractive to perform band-engineering.

The net polarization of AlGaN/GaN heterostructure is given by the sum of spontaneous and piezoelectric polarizations:

$$\boldsymbol{Pnet} = \boldsymbol{Psp} + \boldsymbol{Ppz} \tag{2.9}$$

2.1.5 Physical Properties of GaN Compared to other WBG Semiconductors

The physical properties that make the III-nitrides suitable for high frequency and high power applications are large bandgap, high breakdown field, high thermal conductivity, high charge carrier density and mobility, high saturation velocity and strong chemical bond. On the

other hand, the figure-of-merits (FOM) which is a calculated number in order to quantify the performance of semiconductor devices is also higher for GaN compared to most of the other WBG semiconductors and Si.

Basic material properties at room temperature and FOM for III-nitrides and other wide bandgap semiconductors are listed in Table 2.3.[14,15,16,17,18] FOM is calculated based on the most relevant properties for particular applications such as high power and high-frequency applications and gives a rough measure of the relative strength of the material.

Table 2.3: Material properties at room temperature and FOM for III-nitrides and other wide-bandgap semiconductors.

Parameters	Si	GaAs	AlN	InN	4H-SiC	GaN	Diamond
Crystal Structure	Diamond	Zincblende	Wurtzite	Wurtzite	Hexagonal	Hexagonal, cubic	Diamond
Density (g/cm^3)	2.328	5.32	3.26	6.81	3.21	6.1	3.515
Melting Point (^oC)	1415	1238	2200	1100	2830	2573	4373
Thermal Conductivity (W/cm.K)	1.5	0.46	2.85	2	2.3-4.9	1.3-2.3	6-22
Bandgap (eV)	1.12	1.42	6.2	0.65	3.26	3.44	5.46-5.6
Dielectric Constant	11.7	12.9	8.5	15.3	10.0	9.5	5.7
Electron Mobility ($cm^2/V.s$)	1500	8500	300	3200	1000	1250 AlGaN/GaN: 2100	2200
Hole Mobility ($cm^2/V.s$)	450	400	14	220	150	200	1800

Breakdown field (MV/cm)	0.3	0.4	8.4	1.2	3	4	10
Saturated Electron Velocity (x10^7 cm/s)	1	1	1.4	2.5	2.7	2.7	1.56
JFOM (Relative to Si)	1	1.8	5120	58	400	1600	81000
BFOM (Relative to Si)	1	14.6	32158	46	548	1507	25106

The Johnson's FOM is calculated based on the critical electric field and saturation electron drift velocity in defining a measure of the high-frequency capability of a material and is given by;[19]

$$JFOM = \frac{E_C^2 v_s^2}{4\pi^2} \tag{2.10}$$

where E_C is the critical electrical field, v_s is the saturation electron drift velocity.

Moreover, the Baliga's FOM takes into account the dielectric constant, carrier mobility, and electric breakdown field to measure the high-power handling capability and to minimize conduction losses in power field effect transistors (FETs) and is given by;[20]

$$BFOM = \varepsilon \mu E_C^3 \tag{2.11}$$

where ε is the dielectric constant and μ is the mobility.

For GaN, both the JFOM and BFOM are more than 1000 times higher than Si and JFOM is about four times higher than SiC and BFOM is about three times higher. From these figures, it is clear that for high power and high-frequency applications, GaN is a highly promising candidate.

Overall, because of the intrinsic material properties, GaN possesses several advantages over many other wide bandgap semiconductors. In summary, the main advantages of GaN material properties can be listed as below:

- The chemical bonding in GaN is an ionic-covalent bond. Strong bond means it is harder for an electron to jump from one site to the next ultimately leading to the wider bandgap. This leads to a lower intrinsic leakage current and higher operating temperature.
- High electric breakdown fields resulting from large bandgap of GaN permits the devices to sustain high DC and RF terminal voltages.
- To achieve high currents and sustain high-frequency operations, high charge carrier mobility and high saturation velocity are desirable. Although GaN does not have relatively high mobility (1250 $cm^2/V.s$) but has a high value of saturation velocity at high electric field. The AlGaN/GaN heterostructure which possesses the 2DEG at the interface has much higher mobility.
- The thermal conductivity of a semiconductor is important to determine the power dissipation in the devices. Poor thermal conductivity can result in the degradation of device operation at elevated temperature. The high thermal conductivity of GaN can help easily extract the heat from the devices and is beneficial for the design of high power devices.
- Dielectric constant indicates capacitive loading of a transistor which affects the device terminal impedances. WBG semiconductors have the comparatively lower dielectric constant compared to conventional semiconductors. GaN has about 20% lower value of dielectric constant than those for conventional semiconductors. Which means for a

given impedance; GaN devices can be about 20% larger in the area. As a result, the increased GaN area permits the generation of larger carrier density and higher microwave output power.

2.2 AlGaN/GaN Heterostructures and HEMTs Device Overview

2.2.1 Band Structure

In general, a heterojunction is an interface between two dissimilar materials. In semiconductors, it is referred to a junction between two different monocrystalline semiconductor materials with different electronic properties but the similar crystal structures. In the case of homojunction, the energy bandgap does not vary across the junction, but in a heterojunction, there will be a variation in energy gap between two different semiconductors. These variations leverage the degree of freedom in independent control of majority and minority charge carrier flow. When two different semiconductors are brought into physical contact for example, through epitaxial growth of one semiconductor on top of another semiconductor, the Fermi level in two semiconductors must be equal and constant under the equilibrium conditions. When two semiconductors with different bandgaps are in contact, carriers will flow across the junction, building space and interface charges until the Fermi energy is same everywhere in the material. There is also band discontinuities in the alignment of the two structures, which results in band bending to align the Fermi level of the heterostructure.

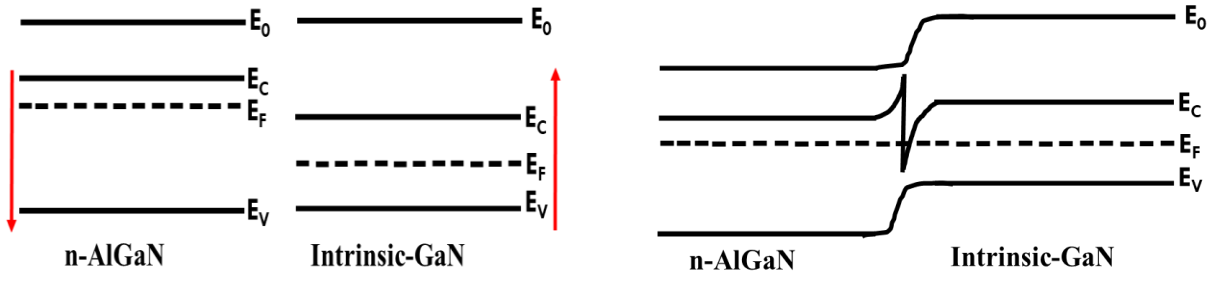

Fig. 2.5. Band diagram of an AlGaN/GaN before and after Fermi level alignment.

The resulted net polarization as described above exerts an electric field that causes bands to bend such that the conduction band is close to the Fermi level at the heterojunction. Bands at two sides are connected by means of some kind of cusp or notch and junction, and the nature of cusp or notch depends on the details of the system. In the case of AlGaN/GaN heterostructure, the band alignment falls under the type-I category known as a straddle. The structures are created by growing wide bandgap AlGaN barrier layer (doped or undoped) on top of a smaller bandgap unintentionally doped relaxed GaN layer. Figure 2.6 shows the schematics of cross-section of AlGaN/GaN heterostructure and the corresponding energy band diagram. When the differing band gap materials (AlGaN and GaN) brought into contact, the energy band offsets and difference in band gaps between two materials causes the conduction band to instantaneously drop below and then gradually rise toward the Fermi level. Consequently, a small triangular quantum potential well near the boundary of the interface forms as shown in Fig. 2.6 (b) where the electrons are accumulated.

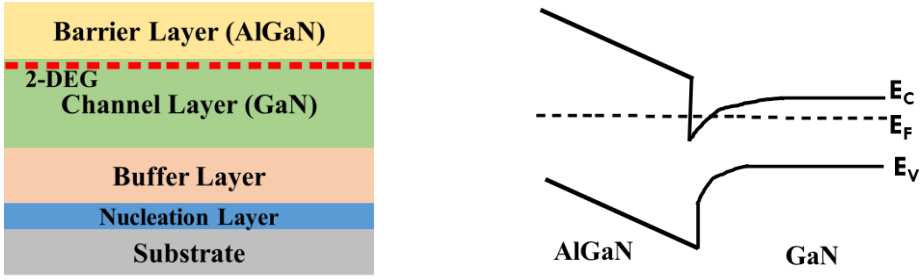

(a) (b)

Fig. 2.6. (a) Schematics of a cross-section of AlGaN/GaN heterostructure (b) energy band diagram of the heterostructure.

In this potential well, electrons are free to move parallel to the interface but are tightly confined in the perpendicular direction. The electrons in this region appear to be as a two-dimensional sheet. Therefore they are referred to as 2-dimensional electron gas (2DEG). The confine-

ment of the channel electrons in the quantum well granting two-dimensional feature strongly enhances the mobility of the structure because it eliminates the need for carriers to travel through the lattice in which they can easily be scattered by lattice atoms and bulk carriers. The 2DEG characteristics at quantum well can be greatly controlled by altering the gate voltage. The presence of 2DEG is one of the biggest advantages of such a heterostructure and is introduced without intentional doping to compensate the polarization induced positive sheet charge.[21] This peculiar feature of this heterostructure is being used in the fabrication of innovative device called HEMT which remains in the center of attraction in electronic applications.

2.2.2 HEMT Device Overview

As mentioned earlier HEMT stands for High Electron Mobility Transistor, and this is a member of the family of field effect transistors (FETs). The structure is also known as MODFET (Modulation-Doped Field Effect Transistor), MISHEMT (Metal Insulator High Electron Mobility Transistor) and HFET. At the heterostructure, the conduction band of the barrier layer is higher than that of the channel layer and because of the large discontinuity in conduction band, carriers diffuse from the large bandgap (AlGaN) (can be doped or undoped) to the narrow bandgap (GaN) layer at which heterointerface a channel of 2DEG is formed in a triangular quantum well. This 2DEG formed at the triangular potential well is the hallmark of a HEMT. The 2DEG sheet charge carrier concentration can be controlled by applying the voltage through a Schottky barrier gate formed on the barrier layer. Another feature of this modulation doping is that the channel carriers are spatially separated from the rest of the carriers and have high mobilities because there is no impurity scattering.

The AlGaN/GaN HEMTs are currently grown[22] on Si, sapphire,[23] SiC,[24] and GaN[25] substrates. Except for GaN substrates, the main growth challenge is due to thermal expansion and

lattice mismatch. However, although GaN substrate does not have this problem, this substrate remains undesirable because of the small size and extremely high cost. Intermediate nucleation buffer layers are grown between the substrate and the channel layer to prevent the cracking of GaN grown on foreign substrates (except sapphire), governed by a tensile strain due to lattice mismatch, On top of the buffer layer, a GaN layer is grown mostly along the [0001] direction to benefit from the spontaneous polarization of the *c*-plane within the GaN wurtzite crystal, and a channel is formed within this layer; therefore it is called the channel layer. A layer with the higher bandgap and the lesser electron affinity (AlGaN) is grown on top of the channel layer and referred to as a barrier layer. This barrier layer can be either doped or intrinsic. Due to the conduction band offset and the difference in the polarization between the AlGaN and the GaN layer, a potential quantum well will be created underneath the hetero-interface, trapping the electrons inside, and consequently creating the channel. The depth of the well is associated with the difference in electron affinity.

Figure 2.7 shows a conventional Schottky gate AlGaN/GaN HEMT device structure. The source and drain terminals constitute an ohmic contact metallization, and the gate contact is made of Schottky contact metallization. Electrons flow from a source contact (S) to a drain contact (D) through a very low resistance of 2DEG formed at the interface of AlGaN and GaN, when a voltage (V_{DS}) is applied between them. The amount of current (I_{DS}) flow is modulated by the voltage applied at the gate (G). The HEMT devices that we are considering in this study are "normally-on" devices in which 2DEG exists without an applied voltage at the gate. In such a device, current will flow between the source and drain as long as a voltage is applied between the source and drain contacts. Biasing the gate to an increasingly negative voltage will decrease the electric field through AlGaN causing the depth of penetration of the triangular well to lessen until the pinch-off

voltage (V_{PO}) is reached, at which time a 2DEG no longer forms, and the channel no longer passes the current, effectively switching off the device. On the other hand, when the gate voltage is increased, the electric field steepens, deepening the triangular energy well which in turn raises the number of available energy states for carriers traveling through the 2DEG and increase the density of carriers in 2DEG. Therefore, for a given drain-source voltage the amount of current will increase.

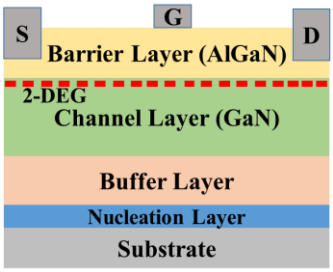

Fig. 2.7. A conventional Schottky gate AlGaN/GaN HEMT schematics.

The modulation of I_{DS} can be explained with the help of a simple model shown in Fig. 2.8 and described below. The AlGaN layer is supposed to be n-type with a doping concentration of N_D. The valence band offset between GaN and AlGaN layer is considered as ΔE_C, the Schottky barrier height Φ_b and the net polarization charge density σ_{pol}.

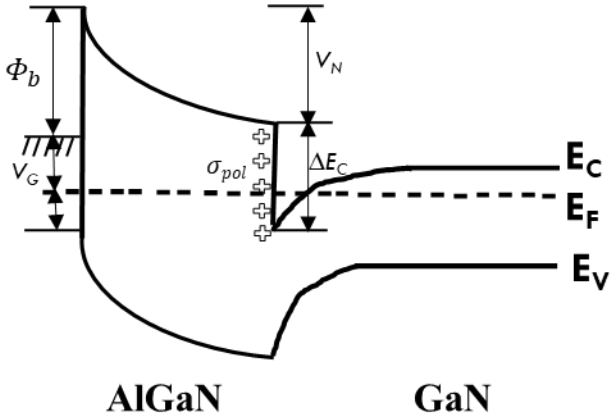

Fig. 2.8. AlGaN/GaN heterojunction band with applied gate bias.

For the heterostructure under study, assuming the potential well to have only two quantum levels, E_0 and E_1, which are relevant for the operation of the device, since all other levels are always above the Fermi level. A self-consistent solution to the Poisson and Schrodinger equation gives us the 2DEG density (cm^{-2}) in terms of the energy levels as;[26]

$$n_s = DkT \left\{\left[1 + exp\left(\frac{E_F - E_0}{kT}\right)\right]\left[1 + exp\left(\frac{E_F - E_1}{kT}\right)\right]\right\} \tag{2.12}$$

where $D = \frac{qm}{\pi\hbar^2}$ is the density of states of the 2DEG gas at the 2-dimensional potential well, k is Boltzmann's constant, T is temperature and E_F is Fermi energy.

Shottky gate on the AlGaN layer results in depletion beneath the gate. If the AlGaN layer is thin or when a sufficiently large negative gate voltage is applied, the gate depletion and junction depletion regions overlap. Neglecting interface states, the 2DEG density can be further written as;

$$n_s = \frac{\varepsilon}{et}\left(V_{GS} - V_{TH} - \frac{E_F}{e}\right) \tag{2.13}$$

where V_{GS} is the gate-source voltage, e is the electronic charge, t is the thickness of the AlGaN barrier layer and ε is the dielectric constant of AlGaN.

The gate voltage under which the 2DEG in the channel is depleted and generated is defined as the threshold voltage (V_{TH}) and is given by[27]:

$$V_{TH} = \Phi_b - \Delta E_C - \frac{eN_D t^2}{2\varepsilon} \tag{2.14}$$

where the term $V_{PO} = \frac{eN_D t^2}{2\varepsilon}$ is called the pinch-off voltage, N_D is doping concentration in the doped AlGaN layer. In the case of not intentionally doped AlGaN (barrier) layer $V_{PO} = 0$.

In Equation 2.13, Fermi energy is a function of V_{GS}, which is always very small as compared to the other terms. Therefore, we can obtain 2DEG carrier density using the following approximate result from equation 2.13:

$$n_s = \frac{\varepsilon}{et}(V_{GS} - V_{TH}) \tag{2.15}$$

If we take into account the polarization charge density (σ_{pol}), the expression for the threshold voltage can be modified as[28];

$$V_{TH} = \Phi_b - \Delta E_C - \frac{eN_D t^2}{2\varepsilon} - \frac{\sigma_{pol} t}{\varepsilon} \tag{2.16}$$

At the threshold voltage, the 2DEG occupies the lowest energy level and coincides with the Fermi level. With the voltage V_{DS} applied if $V_{GS} > V_{TH}$, the 2DEG is in a continuous state and the device is turned on; if $V_{GS} < V_{TH}$, the 2DEG is depleted and the device is turned off. For the weak inversion case (close to pinch off), the Fermi level is below most of the allowed energy states. The carrier density is small in the 2DEG. In this case, the Fermi energy and the 2DEG density can be expressed as[29]:

$$E_F = kT\, ln\left(\frac{n_s}{2DkT}\right) \tag{2.17}$$

$$n_s = 2DkTexp\left(\frac{e(V_{GS} - V_{TH})}{kT}\right) \tag{2.18}$$

After past the weak inversion region (close to pinch off), the device starts to operate in the strong inversion region. In this situation, the sheet carrier density is much higher, and the Fermi level is much higher in the potential well. Conventionally, the threshold voltage is defined as the beginning of the strong inversion region. In this case, the Fermi level and the sheet carrier density are given by the following expressions[28]:

$$E_F = \frac{n_s}{2D} \tag{2.19}$$

$$n_s = \frac{2\varepsilon eD}{\varepsilon + 2e^2 Dt}(V_{GS} - V_{TH}) \tag{2.20}$$

Since HEMT is a field effect device, its DC behavior is characterized by output channel current (also called as a drain current) I_D which is controlled by the channel potential $V_C(x)$, after the 2DEG is formed. The output current is typically proportional to the channel width W which can be derived by multiplying the carrier density by carrier velocity and the gate width W of the transistor as;

$$I_D = en_s(x)Wv(x) \tag{2.21}$$

where $v(x)$ is the electron velocity. The velocity depends on the electric field in the channel similar to the MOSFET operation.

As we increase the electric field, at some point the drain current saturates and, the saturated electron velocity approaches to infinity. The applied voltage at this point is called the knee voltage. At very high fields, the velocity reaches its saturation level v_s, but below this limit, the velocity is limited by mobility. The electric field at which the velocity saturates is defined as the critical field E_C. The electron velocity can be written as follows for different electric field regimes:

$$v = \mu E, for\ E < E_C \tag{2.22}$$

$$v = v_s, for\ E \geq E_C \tag{2.23}$$

where μ *is* the mobility of the electrons in the channel. The drain current for the electric field less than the critical field is given by:

$$I_D = \mu W \frac{\varepsilon}{t}(V_{GS} - V_C(x) - V_{TH})\frac{dV_C}{dx} \tag{2.24}$$

$C = \frac{\varepsilon}{t}$ is called the dielectric capacitance per unit area.

In the linear region of operation, the drain current is proportional to the sheet carrier density, channel length, and the electric field. The potential gradient in the above expression can be approximated and written as follow[30];

$$I_D = \mu \frac{W}{L}\frac{\varepsilon}{t}(V_{GS} - V_{TH})\big(V_C(L) - V_C(0)\big) \tag{2.25}$$

where L is the gate length.

When the voltage is applied across the channel, there will be a voltage drop at the resistive segments of the drain and source. The electric field is proportional to the drain voltage and the sheet carrier density depends on the applied gate voltage. Therefore, the above expression can be modified to include the effects of drain and source excess resistances R_D and R_S respectively. For $V_C(0) = R_S I_{DS}$ and $V_C(L) = V_{DS} - R_D I_{DS}$ equation 2.25 can be written as;

$$\frac{V_{DS}}{I_{DS}} = R_S + R_D + \frac{L\,t}{W\,\mu\,\varepsilon\,(V_{GS} - V_{TH})} \tag{2.26}$$

The mobility can be obtained from the reciprocal of the slope of the plot of $\frac{V_{DS}}{I_{DS}}$ *vs.* $\frac{1}{(V_{GS} - V_{TH})}$ from equation 2.26. The calculation of mobility from this method neglects the interface states. And the transconductance g_m which describes the modulation of the drain current by gate-source voltage is given by:

$$g_m = \left(\frac{\partial I_D}{\partial V_{GS}}\right) \text{ at constant } V_D \tag{2.27}$$

We fabricated circular transistor devices following the Corbino geometry to avoid mesa isolation (Fig. 3.10, next chapter). The outer ring with radius R_2 was used as the source and the inner circle of radius R_1 was used as the drain. Due to the Corbino geometry of the devices, the channel width -to-length ratio (aspect ratio) was defined through effective $W/L = 2\pi/ln\,(R_2/R_1)$.[31]

2.2.2.1 Breakdown for AlGaN/GaN HEMTs

When the drain is stressed with a high voltage and the gate voltage is below the threshold voltage, HEMT devices get into the block region. In this case, the GaN region is depleted from the drain to the gate. This depleted region helps to sustain the high voltage. The high critical field (3.3 MV/cm)[32] of GaN gives the ability to handle the high voltage and can be used to design the high-efficiency power devices. Under the drain voltage stress, if the local electric field in the device is

higher than the critical field, the device will break down. If the breakdown occurs in the GaN or AlGaN regions, the electrons generated can destroy the 2DEG in the heterojunction. In this condition, the on-resistance of the device would sharply increase, and the device failure will occur.

Since the gate contact of HEMT is a Schottky type, it will have higher leakage than the MOS and junction devices in the reverse bias condition. To restrain the early breakdown phenomenon and to increase the breakdown voltage, several methods such as gate/source electric field plate[33,34] and air bridge field plate[35] are proposed to depress the surface electric field.

2.2.2.2 Capacitance-Voltage Characteristics

The charge in the metal-semiconductor junction can be modulated by changing the applied voltage between them. The ratio of change in charge due to the change of voltage is defined as the capacitance and is written as:

$$C = \frac{dQ}{dV} \tag{2.28}$$

To measure capacitance, a small AC voltage signal *dV* at a certain frequency is first applied, and the corresponding charge modulation *dQ* is measured.

The total charge in the semiconductor is given by[36]:

$$Q = qN_D W = \sqrt{\left[2qN_D\varepsilon_s\left(V_{bi} - V_{ext} - \frac{kT}{q}\right)\right]} \tag{2.29}$$

where N_D is the donor concentration, ε_s is a dielectric constant of a semiconductor, V_{bi} is the built-in potential, V_{ext} is the external applied potential and W is the width of the depletion region, and for a homogeneously doped Schottky contact it is defined as:

$$W = \sqrt{\frac{2\varepsilon_s}{qN_D}(V_{bi} - V_{ext})} \tag{2.30}$$

The depletion capacitance (per unit area) at given depletion width is expressed as follows:

$$C = \frac{\varepsilon_s}{W} \tag{2.31}$$

For the depletion region where the space charge is uniformly distributed, the depletion capacitance as a function of applied dc bias (V_{ext}) can be derived using Poisson's equation as;

$$C = \sqrt{\frac{\varepsilon_s q N_D}{2\left(V_{bi} - V_{ext} - \frac{kT}{q}\right)}} = \frac{\varepsilon_s}{W} \tag{2.32}$$

For a heterostructure with 2DEG, at the zero external bias, the capacitance across the depletion space charge is given as:

$$C = A.\frac{dQ}{dV} = A\frac{\varepsilon_s}{t} \tag{2.33}$$

where *t* is the distance of the Schottky gate from the 2DEG (thickness of the AlGaN barrier layer). It is assumed that at zero volt applied bias, the depletion region slightly touches 2DEG.

Equation 2.32 can also be written as;

$$\frac{1}{C^2} = \frac{2\left(V_{bi} - V_{ext} - \frac{kT}{q}\right)}{\varepsilon_s q N_D} \tag{2.34}$$

As $\frac{1}{C^2}$ is measured as a function of applied voltage, therefore if the doping concentration is homogeneous, it should be linearly dependent on the bias voltage. Hence, the doping concentration can be determined from the slope of the following equation:

$$N_D = -\frac{2}{q\varepsilon_s}\left[\frac{d}{dV_{ext}}\left(\frac{1}{C^2}\right)\right]^{-1} \tag{2.35}$$

The built-in potential V_{bi} is determined from the extrapolation to $\frac{1}{C^2} = 0$. It is worthy to note that, for inhomogeneous doping, the depth profile of the doping can be determined by *C*-*V* spectroscopy. In such a case, the $1/C^2$ *vs.* applied bias curve is no longer a straight line and possess a varying slope. Ideal *C*-*V* characteristics of a Schottky diode with 2DEG is shown in Fig. 2.9. For

the zero external bias on the Schottky diode, the capacitance is given by equation 2.33. When we apply the negative external bias, space charge under the contact starts to deplete, and as we increase the bias, it will penetrate through 2DEG. The capacitance will decrease rapidly when the depletion region completely penetrates through 2DEG. This is caused because of the very low capacitance of the depleted 2DEG channel C-2DEG, which is in series with the capacitance of the contact.

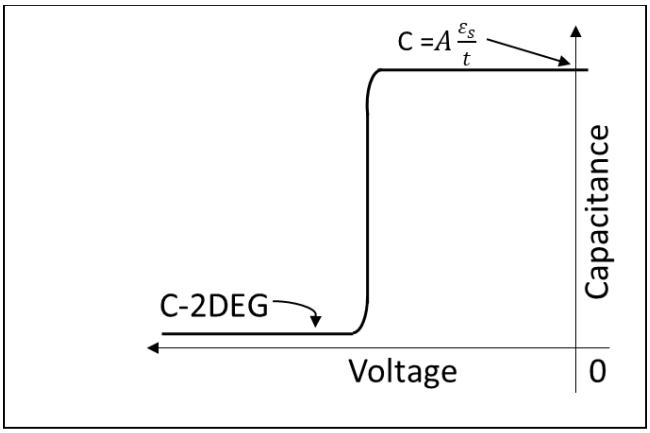

Fig. 2.9. Ideal capacitance-voltage characteristics of a Schottky diode with 2DEG.

The integral of the charge under the *C-V* curve gives the total sheet charge density of 2DEG. For a given gate bias and low electric fields, and assuming the AlGaN layer is not intentionally doped, equation 2.13 can be written as:

$$n_s = \frac{\varepsilon}{et}(V_{GS} - V_{TH}) \tag{2.36}$$

where $C_G = \frac{\varepsilon}{t}$ is the gate capacitance and which is the sum of the several capacitance contributions including GaN cap layer, AlGaN barrier layer, AlN spacer layer and the contribution of the capacitance of distance of the electron gas from the space layer.

2.2.2.3 Schottky Device Operation Characteristics

When a metal comes into contact with a semiconductor at equilibrium, the Fermi levels are forced to coincide and then valence band, and conduction bands bend near the interface as shown

in Fig. 2.10 (b). Due to this phenomena, a potential barrier develops between the metal and semiconductor which prevents the charge carriers moving from one side to another freely. The charge carriers must possess energy higher than the barrier height to be able to flow across the junction. This barrier is known as Schottky barrier (Φ_b), *a*nd the height is called the Schottky barrier height. The Schottky barrier for an n-type semiconductor is given by the difference between the work function of the metal and the electron affinity of the semiconductor;

$$\Phi_b = \Phi_m - \chi \tag{2.37}$$

where $\Phi_m$is the work function of the metal and χ is the electron affinity of the semiconductor.

Prior to bringing into contact, the Fermi level of the semiconductor is above that of the metal as shown in Fig. 2.10 (a). When they are brought into contact, electrons from the conduction band of the semiconductor start flowing into the lower energy states into the metal. As the Fermi energies of the two materials in contact must be equal under the condition of thermal equilibrium, the charge transfer continues until the chemical potential in the semiconductor reached in equilibrium with the Fermi energy of the metal. The Schottky model suggests that the barrier height is independent of the semiconductor doping. However, the transport property across the barrier is highly affected by the doping of the semiconductor.

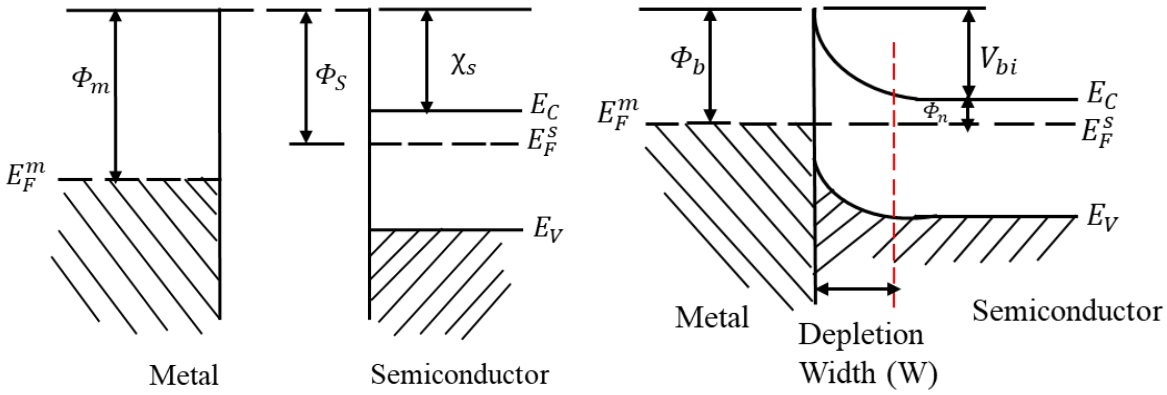

Fig. 2.10. Energy band diagram of metal and an n-type semiconductor in (a) close proximity (b) perfect contact.

The alignment of Fermi levels creates the depletion region and whose width is given by equation 2.30. The built-in potential (V_{bi}) is the potential across the depletion region in thermal equilibrium. This potential is also necessary for electrons in the conduction band to overcome to move into the metal and is given by:

$$V_{bi} = \Phi_b - \Phi_n \tag{2.38}$$

where Φ_n is the magnitude of the potential difference between the conduction energy band (E_C) and the Fermi energy level (E_F).

Reverse bias potential increases the semiconductor to metal barrier potential, whereas forward biasing lowers the barrier height facilitating the flow of the electrons across the junction if sufficient energy is provided to the carriers for their transport. Regardless of the biasing direction, the metal to semiconductor barrier height remains the same.

The current transport mechanism for a Schottky diode based on thermionic emission theory is given by[37]:

$$I = I_S exp\left({qV}/{nkT}\right)\left[1 - exp\left({-qV}/{kT}\right)\right] \tag{2.39}$$

where I_S is the saturation current given as;

$$I_S = AA^*T^2 exp\left({-q\Phi_b}/{kT}\right) \tag{2.40}$$

n is the ideality factor, *V* is the forward bias voltage, *T* is the absolute temperature, *q* is the electron charge, *k* is the Boltzmann's constant, Φ_b is the Schottky barrier height, *A* is the effective diode area, and A^* is the effective Richardson constant for channel layer semiconductor (n-GaN in our case).

The saturation current is determined at the intersection on *y*-axis (*i.e.*, *V*=0) of the extrapolated *I-V* curve, and the slope is ${q}/{nkT}$ from which we can determine the ideality factor as:

$$^{q}/_{nkT} = \text{ slope} \tag{2.41}$$

And, $$^{q}/_{slope(kT)} = n \tag{2.42}$$

Thus, the Schottky barrier height can be calculated from equation 2.40 as;

$$\Phi_b = \frac{kT}{q} ln \frac{AA^* T^2}{I_S} \tag{2.43}$$

References

[1] Cimalla, V., J. Pezoldt, and O. Ambacher. "Group III nitride and SiC based MEMS and NEMS: materials properties, technology and applications." *Journal of Physics D: Applied Physics* 40, no. 20 (2007): 6386.

[2] Xia, Hui, Qing Xia, and Arthur L. Ruoff. "High-pressure structure of gallium nitride: Wurtzite-to-rocksalt phase transition." *Physical Review B* 47, no. 19 (1993): 12925.

[3] Wu, Jun, Hiroyuki Yaguchi, Hiroyuki Nagasawa, Yoichi Yamaguchi, Kentaro Onabe, Yasuhiro Shiraki, and Ryoichi Ito. "Crystal structure of GaN grown on 3C-SiC substrates by metalorganic vapor phase epitaxy." *Japanese journal of applied physics* 36, no. 7R (1997): 4241.

[4] Pankove, Jacques I., and Theodore D. Moustakas, eds. "Gallium Nitride (GaN)." (1998): p15.

[5] Ambacher, O., J. Smart, J. R. Shealy, N. G. Weimann, K. Chu, M. Murphy, W. J. Schaff et al. "Two-dimensional electron gases induced by spontaneous and piezoelectric polarization charges in N-and Ga-face AlGaN/GaN heterostructures." *Journal of applied physics* 85, no. 6 (1999): 3222-3233.

[6] Momma, Koichi, and Fujio Izumi. "VESTA 3 for three-dimensional visualization of crystal, volumetric and morphology data." *Journal of applied crystallography* 44, no. 6 (2011): 1272-1276.

[7] Vurgaftman, I., and JR N. Meyer. "Band parameters for nitrogen-containing semiconductors." *Journal of Applied Physics* 94, no. 6 (2003): 3675-3696.

[8] Bernardini, Fabio, Vincenzo Fiorentini, and David Vanderbilt. "Spontaneous polarization and piezoelectric constants of III-V nitrides." *Physical Review B* 56, no. 16 (1997): R10024.

[9] Wei, Qiyuan. *Polarization Effects in Group III-Nitride Materials and Devices*. Arizona State University, 2012.

[10] Quay, RŘdiger. "III-N Materials, and the State-of-the-Art of Devices and Circuits." *Gallium Nitride Electronics* (2008): 3-90.

[11] O. Ambacher *et al.*, "Two dimensional electron gases induced by spontaneous and piezoelectric polarization in undoped and doped AlGaN/GaN heterostructures," *Journal of Applied Physics,* vol. 87, no. 1, pp. 334–344, Jan. 2000.

[12] Foutz, B. E., O. Ambacher, M. J. Murphy, V. Tilak, and L. F. Eastman. "Polarization induced charge at heterojunctions of the III–V nitrides and their alloys." *physica status solidi (b)* 216, no. 1 (1999): 415-418.

[13] Mailhiot, C., and D. L. Smith. "Electronic structure of [001]-and [111]-growth-axis semiconductor superlattices." *Physical Review B* 35, no. 3 (1987): 1242.

[14] Ueda, Daisuke. "Properties and advantages of gallium nitride." In *Power GaN Devices*, pp. 1-26. Springer, Cham, 2017.

[15] Pearton, S. J., F. Ren, A. P. Zhang, and K. P. Lee. "Fabrication and performance of GaN electronic devices." *Materials Science and Engineering: R: Reports* 30, no. 3-6 (2000): 55-212.

[16] Pérez-Tomás, Amador, Ekaterine Chikoidze, Michael R. Jennings, Stephen AO Russell, Ferechteh H. Teherani, Philippe Bove, Eric V. Sandana, and David J. Rogers. "Wide and ultra-wide bandgap oxides: where paradigm-shift photovoltaics meets transparent power electronics." In *Oxide-based Materials and Devices IX*, vol. 10533, p. 105331Q. International Society for Optics and Photonics, 2018.

[17] Yoder, Max N. "Wide bandgap semiconductor materials and devices." *IEEE Transactions on Electron Devices* 43, no. 10 (1996): 1633-1636.

[18] Zhou, Yi, Dake Wang, Claude Ahyi, Chin-Che Tin, John Williams, Minseo Park, N. Mark Williams, and Andrew Hanser. "High breakdown voltage Schottky rectifier fabricated on bulk n-GaN substrate." *Solid-state electronics* 50, no. 11-12 (2006): 1744-1747.

[19] Johnson, E. "Physical limitations on frequency and power parameters of transistors." In *1958 IRE International Convention Record*, vol. 13, pp. 27-34. IEEE, 1966.

[20] Baliga, B. Jayant. "Power semiconductor device figure of merit for high-frequency applications." *IEEE Electron Device Letters* 10, no. 10 (1989): 455-457.

[21] Ambacher, O., J. Smart, J. R. Shealy, N. G. Weimann, K. Chu, M. Murphy, W. J. Schaff et al. "Two-dimensional electron gases induced by spontaneous and piezoelectric polarization charges in N-and Ga-face AlGaN/GaN heterostructures." *Journal of applied physics* 85, no. 6 (1999): 3222-3233.

[22] Selvaraj, Susai Lawrence, Arata Watanabe, Akio Wakejima, and Takashi Egawa. "1.4-kV breakdown voltage for AlGaN/GaN high-electron-mobility transistors on silicon substrate." *IEEE Electron Device Letters* 33, no. 10 (2012): 1375-1377.

[23] Saito, Wataru, Tomohiro Nitta, Yorito Kakiuchi, Yasunobu Saito, Kunio Tsuda, Ichiro Omura, and Masakazu Yamaguchi. "On-resistance modulation of high voltage GaN HEMT on sapphire substrate under high applied voltage." *IEEE Electron Device Letters* 28, no. 8 (2007): 676-678.

[24] Sheppard, S. T., K. Doverspike, W. L. Pribble, S. T. Allen, J. W. Palmour, L. T. Kehias, and T. J. Jenkins. "High-power microwave GaN/AlGaN HEMTs on semi-insulating silicon carbide substrates." *IEEE Electron Device Letters* 20, no. 4 (1999): 161-163.

[25] Chu, K. K., P. C. Chao, M. T. Pizzella, R. Actis, D. E. Meharry, K. B. Nichols, R. P. Vaudo et al. "9.4-W/mm power density AlGaN-GaN HEMTs on free-standing GaN substrates." *IEEE Electron Device Letters* 25, no. 9 (2004): 596-598.

[26] Shur, Michael. "Modulation Doped Field Effect Transistors." In *GaAs Devices and Circuits*, pp. 513-610. Springer, Boston, MA, 1987.

[27] H. Morkoç, Handbook of Nitride Semiconductors and Devices (Wiley, New York, 2008), Vol. 3, p. 349.

[28] Rashmi A. Kranti S. Haldar R. S. Gupta "Impact of strain relaxation of AlGaN layer on 2-DEG sheet charge density and current voltage characteristics of lattice mismatched AlGaN/GaN HEMT's" Microelectron. J. vol. 33 no. 3 pp. 205-212 Mar. 2002.

[29] Rashmi, A. Kranti, S. Haldar, and R. S. Gupta. "An accurate charge control model for spontaneous and piezoelectric polarization dependent two-dimensional electron gas sheet charge density of lattice-mismatched AlGaN/GaN HEMTs." *Solid-State Electronics* 46, no. 5 (2002): 621-630.

[30] Delagebeaudeuf, Daniel, and Nuyen T. Linh. "Metal-(n) AlGaAs-GaAs two-dimensional electron gas FET." *IEEE Transactions on Electron Devices* 29, no. 6 (1982): 955-960.

[31] Giraldo, A., A. Paccagnella, and A. Minzoni. "Aspect ratio calculation in n-channel MOSFETs with a gate-enclosed layout." *Solid-State Electronics* 44, no. 6 (2000): 981-989.

[32] Visalli, Domenica, Marleen Van Hove, Joff Derluyn, Stefan Degroote, Maarten Leys, Kai Cheng, Marianne Germain, and Gustaaf Borghs. "AlGaN/GaN/AlGaN double heterostructures on silicon substrates for high breakdown voltage field-effect transistors with low on-resistance." *Japanese Journal of Applied Physics* 48, no. 4S (2009): 04C101.

[33] Karmalkar, Shreepad, and Umesh K. Mishra. "Enhancement of breakdown voltage in AlGaN/GaN high electron mobility transistors using a field plate." *IEEE transactions on electron devices* 48, no. 8 (2001): 1515-1521.

[34] Saito, Wataru, Yoshiharu Takada, Masahiko Kuraguchi, Kunio Tsuda, Ichiro Omura, Tsuneo Ogura, and Hiromichi Ohashi. "High breakdown voltage AlGaN-GaN power-HEMT design and high current density switching behavior." *IEEE Transactions on electron devices* 50, no. 12 (2003): 2528-2531.

[35] R. Chu *et al.*, "1200-V Normally Off GaN-on-Si Field-Effect Transistors With Low Dynamic on -Resistance," *IEEE Electron Device Letters*, vol. 32, no. 5, pp. 632–634, May 2011.

[36] Grundmann, M. "The physics of semiconductors: an introduction including devices and nanophysics. 2006." *Verlag Berlin Heidelberg: Springer*.

[37] S. M. Sze and K. K. Ng, *Physics of Semiconductor Devices*. John Wiley & Sons, 2006.

Chapter 3

Device Processing and Electrical Characterization

3.1 Introduction

This chapter focuses on the semiconductor processing techniques for the device fabrication and equipment used for the fabrication and characterization of AlGaN/GaN HEMT transistors and the Schottky contacts on HEMT heterostructures. Theoretical description of the electrical characterization techniques and detailed experimental procedures and recipes of the fabrication of the devices used to report the results of this dissertation are explained.

3.2 Growth: Metal Organic Chemical Vapor Deposition (MOCVD)

Samples under this study were grown using metal organic chemical vapor deposition (MOCVD) technique. The research for MOCVD was first started in the late 1960s by Manasevit and coworkers.[1] This technique possesses several strengths such as high purity, high growth rate, high uniformity, and capability for abrupt interfaces, and more. The MOCVD process is basically a CVD process specified with the use of metal-organic compounds for supplying the group-III element sources. It is a nonequilibrium growth technique in which a hydride gas containing the group-V elements such as AsH_3 or NH_3 (especially for nitride growth), is commonly used. The precursors are transported, and the chemical reactions take place in the vapor phase of the precursors leading to the formation of a solid material deposited on a substrate. The chemical reactions are facilitated by introducing some external energy, such as heat, plasma, photons, and ion-beam for pyrolysis of the precursors and assistance to the reactions.[2] Following are the simplified key steps involved in a CVD process:

1. Precursors transport to the growth region

2. Reactions of gas-phase precursors in the growth region producing reactive intermediate by-products
3. Mass transport of reactants to the substrate surface
4. Adsorption of reactants on the substrate surface
5. Surface diffusion to growth sites
6. Surface reactions and nucleation leading to the solid formation
7. Desorption and mass transport of decomposed fragments away from the growth zone
8. Exhaust to the pumping system

Growth rate and composition are controlled by controlling the mass flow rate and dilution of various components of the gas stream. Organometallic group III sources are either liquid or solid and stored in the bubbler through which a carrier gas flows. This carrier gas will saturate with vapor from the source and transport vapor to the heated substrate. The substrate usually is kept on a block of graphite called a susceptor and heated by radio frequency (RF) coil, a resistance or a strip heater. Walls are colder than the heated interior that helps to reduce the reactant depletion effect that hot walls cause which is the most important feature of MOCVD. Typically, MOCVD is used in the mass transport limited regime, in which the growth rate solely depends on the amount of metal organic supplied.[3] For GaN the growth temperature is in the range of 1050 ^{O}C, and it is up to 1500 ^{O}C for AlN. The pressure range of the reactor lies between 100 Pa to close to 100 kPa (ambient pressure). The fastest growth rate up to 5 μm/hr can be achieved. Major impurities found are oxygen, hydrogen, carbon, and silicon.[4]

The AlGaN/GaN HEMT samples used to study the device characteristics in this research were grown on top of six-inch p-type Si wafers *via* MOCVD technique. AlN nucleation layer of thickness 0.25 μm was grown on top of Si, and AlGaN buffer multilayer with varied aluminum (Al)

concentrations between 20%-75% was deposited on top of the AlN layer. An undoped GaN layer of thickness 1μm was deposited on top of the AlGaN buffer layer, followed by a 20 nm AlGaN barrier layer. A GaN cap layer of a thickness of 2 nm was grown on top of the barrier layer. The schematic cross section of the grown sample is shown in figure 3.1.

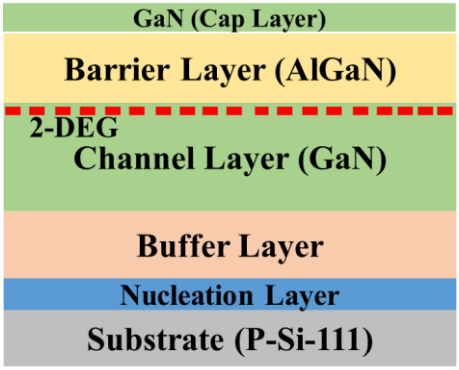

Fig. 3.1. Schematics of MOCVD grown AlGaN/GaN HEMT heterostructures used in this study.

3.3 Cleaning

Wafer surface can easily get contaminated during the storage and device fabrication process through chemicals/gases, water, tools, and human activities. These contaminants can easily get absorbed onto the wafer surface and occupy a space into the electrically sensitive area leading to a catastrophic device failure. The micro-contaminants may cause 50% of yield loss in integrated circuit fabrication. Therefore, having a clean surface is an essential requirement in the fabrication of electronic devices. Hence, it is essential to remove native oxides, organic contaminants, metallic impurities, particulate contaminants, adsorbed molecules, and residual species before proceeding to the further processing steps.[5,6] Metal contacts and electrical/optical properties can be affected by native oxides which can grow very easily on the exposed surfaces of wafers.

Organic contaminants from photoresist, solvent residues, and ambient air can be adsorb to the semiconductor surface. Metallic impurities such as iron (Fe), copper (Cu), aluminum (Al) along with the ionic metals like sodium (Na) and calcium (Ca) originate from the liquid chemicals,

water as well as handling and processing tools. Chemical contaminants, such as chlorine (Cl), lead to the unwanted etching from the undesired area and create compounds that will become hard to remove from the surface. Surface cleaning can be performed using dry or wet etching of the contaminants. Among those, wet etching is more preferable compared to dry cleaning methods since dry etching mostly results in damaging the surface and making the material electrically unsuitable.[7] The following paragraph describes the cleaning process performed before device fabrication.

Six-inch HEMTs epitaxial wafer was first diced into 1 cm x 1 cm square pieces which were ultrasonically cleaned in the organic solvents with the following order: acetone, trichloroethylene (TCE), acetone, methanol, and methanol for 5 min in each solvent. The first acetone and TCE were used to completely de-grease the organic contaminants (particularly oily or greasy) from the wafer surface. The purpose of second acetone use is to dissolve residues from TCE solvent and acetone itself will deposit contaminants. Hence, the first methanol was used as a solvent for the acetone residues and the second fresh methanol served to further cleaning of the sample. Since the methanol easily dissolves in water, the samples were rinsed in deionized (DI) water to remove the residues of the solvents. After removing organic contaminants, the samples were placed in a mixture of hydrochloric acid (HCl) and DI water (1:1 ratio by vol.) and subsequently heated at 110^0C for 10 minutes to clean the ionic contaminants. Cleaning ionic contaminants is as important as removing organic contaminants; hence an acid mix has been used. It was reported that HCl: DI wet chemical processes produced the lowest coverages of oxygen and carbon contaminants for GaN surface cleaning.[8] In addition, it increases chlorine (Cl) concentration and decreases the oxygen coverage on the surface.[9] The increase of Cl concentration on the surface promotes the adhesion of metals like Ni, Au, Pd, Pt on GaN and hinders re-oxidation of the surface. Therefore, it is beneficial to use HCl cleaning.[8,10] Finally, samples were thoroughly rinsed in DI water, blow-

dried with house nitrogen and examined with the optical microscope for cleanliness. The entire cleaning process was performed inside a fume hood.

3.4 Device Fabrication

Semiconductor device fabrication to form an integrated circuit (IC) requires various chemical and physical processes such as ion implantation, diffusion, oxidation, lithographic patterning, thin film deposition, etching, *etc*. The lithographic process is one of the most fundamental steps in any semiconductor device processing. The process and technology used for the lithography are discussed in the following section.

3.4.1 Photolithography

Photolithography is an optical process which forms three dimensional (3D) relief images of the pattern on the polymer for the subsequent transfer of the pattern on the wafer.[11] Photolithography has its limitations with the minimum sizes to be in a size of a few microns. Therefore, in the modern device fabrication process, electron beam lithography is used to obtain the smaller feature sizes in the nm scale. For our research, microelectronic devices were sufficient to study the results; therefore we employed photolithography. The typical photolithography process involves multiple steps as shown in the chart in Fig. 3.2 to yield the device pattern on a clean substrate.

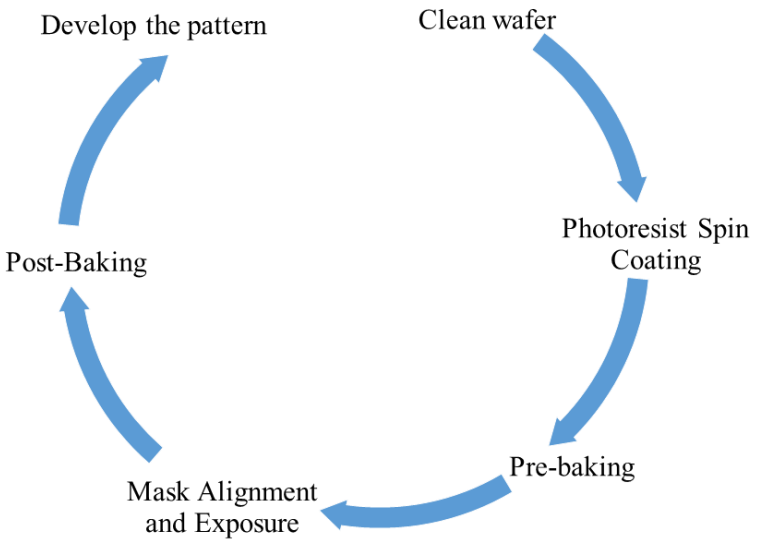

Fig. 3.2. The typical order of photolithography process.

To define the minimum feature size, the most important parameter is the spatial resolution of the system. The minimum feature size depends on the optical elements, radiation wavelength and the photoresist used. The shorter wavelength radiation gives a higher resolution. The minimum feature size (MFS) is associated with the diffraction effect and is typically in the order of wavelength of the radiation used in exposure. The resolution of a photolithography system is associated with the wavelength (λ) of radiation used and numerical aperture (NA) according to the modified Rayleigh criterion as given by[12]:

$$\text{Resolution} = k_1 \frac{\lambda}{NA} \tag{3.1}$$

$$\text{The depth of focus} = k_2 \frac{\lambda}{(NA)^2} \tag{3.2}$$

where k_1 and k_2 are the coefficients of proportionality and are the measures of the difficulty in printing a given dimension with a given exposure system-photoresist combination.

As can be seen from the above equations, decreasing the wavelength and increasing the numerical aperture results in a better resolution. However, the tradeoff is the depth of focus which gets decreased. The diced and cleaned wafer piece (sample) was attached to a three inch Si wafer and placed in the vacuum chuck of a spin coater. The sample was spin-coated with the image reversal photoresist AZ-5214E-IR, which is capable of both positive and negative tone modes (two types of photoresists exist, positive and negative photoresist). The coating speed was maintained at 400 *rpm* for 30 seconds. The liquid photoresist poured in the center of the sample was pushed toward the edges by centrifugal forces as a result of spinning. The frictional force of viscosity opposes the centrifugal force which decreases as the film thins. Moreover, evaporation of the resists increases the viscosity of the resists so this affects the thickness of the coating. The thickness of the coating depends on the speed of spinner, the viscosity of the resist, humidity, and substrate topography as given in the following formula[13]:

$$\text{Thickness} = k\frac{p^2}{\omega^{1/2}} \sim \frac{v^{0.4}}{\omega^{0.2}} \tag{3.3}$$

where k is the spinner constant, p is the resist solid content in the percentage, ω is the rotational speed of the spinner in revolution per minute (*rpm*)/1000, and v is liquid photoresist viscosity.

Immediately after the spin coating of the photoresist, the samples were soft baked at 110°C for 60 seconds. This step helps to drive off the excess solvent in the resist layer, and hence the thickness of the resist will be reduced and also the adhesion of the resist to the substrate will increase. Further, soft baking makes photoresist less viscous and thus becomes less susceptible to particle contamination. The average thickness of the photoresist after the spin coating was measured to be 1.4 μm. After the exposure to the UV light, the positive photoresist becomes more soluble, and for the negative photoresist, it becomes hardened because of the cross-linking between

the polymers. The selection of the type of photoresist depends on the choice of the photomask used to transfer the pattern.

The photoresist coated sample was mounted to the sample holder of the Karl Suss MJB3 photo-mask aligner equipped with a 160 W mercury (Hg) lamp as shown in Fig. 3.3. A photomask of quartz plate patterned with chromium was used to produce the pattern by mounting above the sample. The sample and the patterns of the photomask were aligned using the optical microscope attached to the mask aligner. Then it was exposed to the radiation of Hg lamp at a power of 160 W for 30 seconds. We used a clear field mask with the soft contact illumination mode in all of the device fabrication process. Clear field masks are defined as opaque pattern in a transparent back-ground and dark field mask as a transparent pattern on an opaque background.

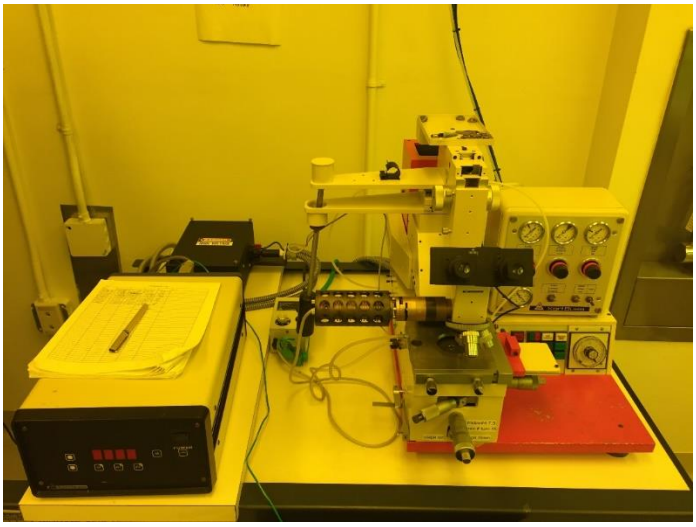

Fig. 3.3. Karl Suss MJB3 photo-mask aligner.

After UV exposure with the mask, samples were hard baked at 110°C for 60 seconds after which the exposed area of the photoresist crosslinks and becomes insoluble in developer, but the unexposed area remains photoactive. Then, a direct re-exposure (no mask) of UV (known as flood exposure) for 60 seconds to the post-baked samples was done which makes the areas that were not exposed before bake, more soluble, resulting in the image reversal.

The samples were then developed in AZ 726 MIF developer to dissolve the soluble area of the photoresist film which resulted in a negative image of the mask pattern on the substrate. The chemicals used as developers for common photoresists are in general aqueous bases such as KOH or tetramethyl ammonium hydroxide (TMAH) for metal ion free (MIF) developers. The shape of the photoresist profile and the linewidth control are determined by the reaction between photoresist and developer, the type of photoresist and the wavelength of light used. There are a few methods to apply the development technique. In this work, puddle development method in which wafer spun to spread the developer efficiency was used to develop the pattern. After the developing time elapsed, the additional developer was rinsed immediately with DI water which is essential to avoid the overdevelopment of the patterns. This technique reduces the usage of developer but may result in overdeveloped patterns.

3.4.2 Metal Contact Deposition: Direct-Current (DC) Magnetron Sputtering

Sputtering is a physical vapor deposition technique used to deposit the films of the source materials (target) onto the substrate. This method uses the plasma processing technique which relies on the creation and use of plasmas to activate a chemical reaction at the substrate. In sputtering, material from the target, which serves as a cathode, is removed by bombarding the energetic ions from the plasma and the ejected materials transport to the surface of the substrate to be deposited.[14] The chamber is filled with an inert gas such as argon (Ar). Sputtering deposition is conducted either in a vacuum or at low pressure with preventing a gas-phase collision in the space between the target and surface. A potential of a few hundred volts is applied between the target (cathode) and the substrate (anode). Thus, plasma of inert gas is created with the help of DC voltage applied. Positively charged ions of the inert gas are attracted and accelerated towards the target that is in a negative potential with respect to the plasma. The energetic ions impinging the target

surface transfer their momentum to the target causing the atoms to eject from the surface of the target. The ejected atoms which are highly energetic (1-10 eV), also known as sputtered species finally get sputtered into the substrate. This high energy of the atoms helps to form a dense film on the substrate for the thin film growth process.

DC magnetron sputtering is a high rate deposition method and can deposit films over a large area. A permanent magnet is placed beneath the target in such a way that its magnetic field is parallel to the target surface. As a result, the secondary electrons circle the magnetic field and stay nearby the surface increasing the ionization efficiency. Since the direction of the applied electric field is perpendicular to the target surface, the resulting force due to magnetic and electric field develops a drift in the direction perpendicular to both $\boldsymbol{E}$ and $\boldsymbol{B}$ fields. Thus, the high plasma density will be produced within the maximum $\boldsymbol{E}$ and $\boldsymbol{B}$ fields. As a result, the electron moves on a close path parallel to the target surface. Thus, the use of magnets in magnetron sputtering enables sputtering to be feasible at low temperature and the voltage resulting in a higher sputtering rate.

Depending upon the nature of supplied power source, two types of magnetron sputtering systems are available called direct current (DC) and radio frequency (RF) magnetron sputtering. DC source can be used to supply higher power as compared to the RF source giving the higher sputtering rate. The limitation of DC sputtering is that it can be used only for the sputtering of conducting target. On the other hand, RF sputtering is applicable to deposit metal and insulator thin films.[15] The schematics of DC magnetron sputtering used for the thin film deposition in this research is shown in figure 3.4.

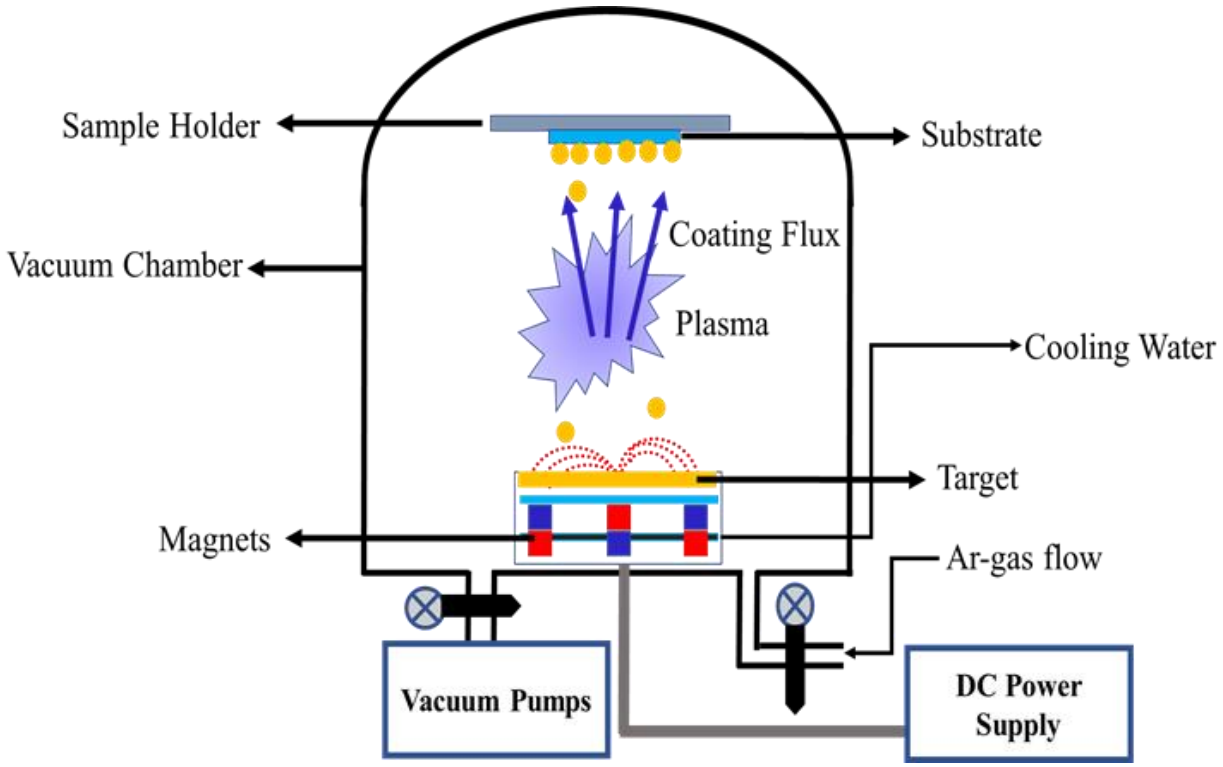

Fig. 3.4. Schematic diagram of the DC-magnetron sputtering system.

For the device fabrication purpose in this research, metal contact deposition was done by DC magnetron sputtering with a maximum attainable power of 1000 W. The system consists of the vacuum chamber with four sputtering guns of two-inch diameter target holding capacity inside the chamber. Chimneys are placed on each gun to facilitate the deposition on the targeted substrate, prevent the ejected material from wide spreading and cross-contamination. The sample holder plate is located right above the sputtering target in a distance of approximately 15 cm which can be mechanically rotated after the vacuum chamber is closed so that it is possible to sputter four different metals successively without venting the vacuum. The photo-lithographically patterned samples were mounted on the sample holder plate. The vacuum chamber which is coupled with a roughing pump and the turbomolecular pump was pumped down to the base pressure of about 10^{-7} Torr to remove the contaminants. Argon gas was introduced into the chamber at the rate of 95 sccm (standard cubic centimeter per minute) until the chamber reaches stable pressure of 18

millitorrs. The required DC voltage was applied between the target (cathode) and the ground at a fixed current to start the plasma process. A short pre-sputtering was performed to remove any impurities on the target surface before depositing the metals on the samples. During pre-sputtering, the samples were kept away from the chimney surface. Finally, the desired metals were deposited on the samples. Chilled water lines were maintained beneath the targets to cool them down during the sputtering process. The picture of DC magnetron sputtering system located at Leach Science Center of Auburn University which is the one used for the metal deposition is shown in figure 3.5 below.

Figure 3.5. The dc-magnetron sputtering system used for the metal deposition in this research.

3.4.3 Lift-off

Lift-off is a step in the semiconductor processing that removes the excess metal deposited on the substrate. In lift-off, the metal deposited on top of the photoresist is washed away by dissolving the resist to the suitable solvent. Duration of the lift-off primarily depends upon the film quality of the deposited material. For dense and thick films, it will take a longer time to lift-off because it will become more impermeable to solvent. Additionally, pre-bake, film deposition temperature, UV exposure dose, type of resist, developer solvent also affects the duration of the lift-off. For the work reported in this dissertation, acetone was used as a lift-off solvent followed by

methanol and DI water rinsing. Image-reversal lithography was used in this work which made lift-off process easy by creating an undercut profile with a negative slope. Fig. 3.6 shows schematics of the process flow of the AlGaN/GaN HEMTs device fabrication.

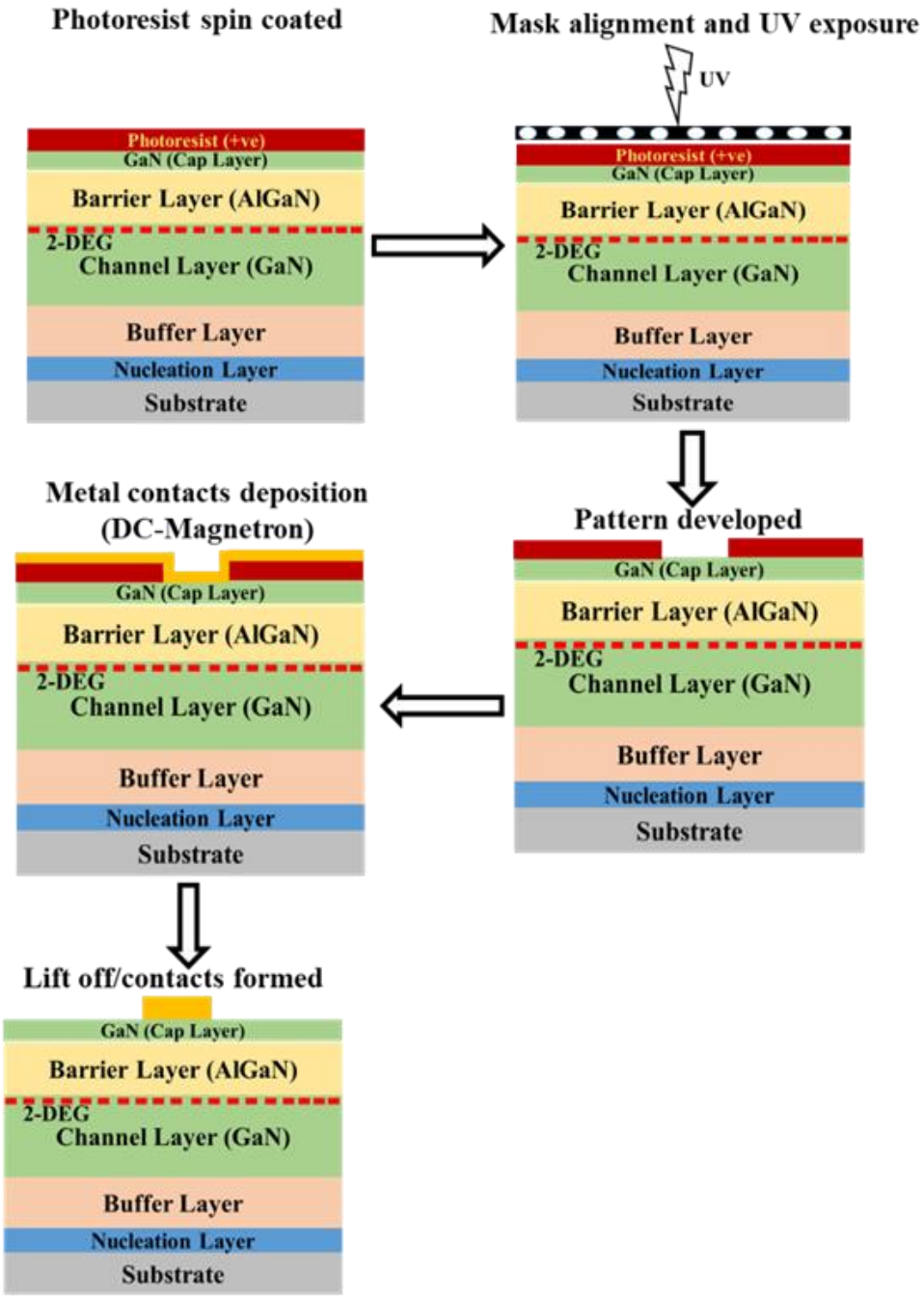

Figure 3.6. Schematics of the process flow of device fabrication.

3.4.4 Rapid Thermal Annealing (RTA)

In the semiconductor industry, rapid thermal annealing (RTA) is a fabrication process step used for the activation of dopants, the interfacial diffusing of metal contacts in multilayers. In principle, the operation involves the rapid heating of a wafer from ambient to a high temperature of around 1200 ^{o}C. As soon as the wafer reaches the desired high temperature, it is held there for a few seconds and then finally quenched. RTA is also used for the change states of grown films, densify deposited film, and repair damage from ion implantation in order to change its electrical properties such as to reduce the electric losses. Process parameters such as temperature, time, and the gas flow need to be controlled properly in order to create low resistance metal-semiconductor contacts. Common gases used for RTA annealing are nitrogen (N_2) and argon (Ar). For the device fabrication of this dissertation work, RTA was done to achieve good ohmic contacts on deposited metal stacks[16] of Ti/Al/Ni on AlGaN/GaN HEMTs. The annealing system consists of a vacuum chamber equipped with custom-made two carbon strips kept two-inch apart used as the heating elements. Also, the system has a variable transformer (to control the current through the carbon heating strip), and an infrared optical pyrometer located right above the vacuum chamber which is focused at the edge of the sample to monitor the position of the sample to confirm the uniformity of the temperature. The schematics of the RTA system used to anneal the samples under the study of this research is shown in Fig. 3.7.

First of all, the samples were loaded in a carbon crucible and then the crucible was mounted on top of the carbon strip inside the chamber. The chamber was pumped down a base pressure of 2×10^{-7} torr using roughing and diffusion pumps to remove the possible moisture and contaminant gases. The research grade high purity N_2 gas was flown to fill the chamber until the chamber pressure is equal to the atmospheric pressure. Then, the current was ramped-up to achieve the

desired annealing temperature of 850°C and maintained for 30 seconds. Immediately after the annealing for 30 seconds, the current was turned off, and the temperature was lowered to room temperature with the aid of a mechanical fan blown close to the chamber.

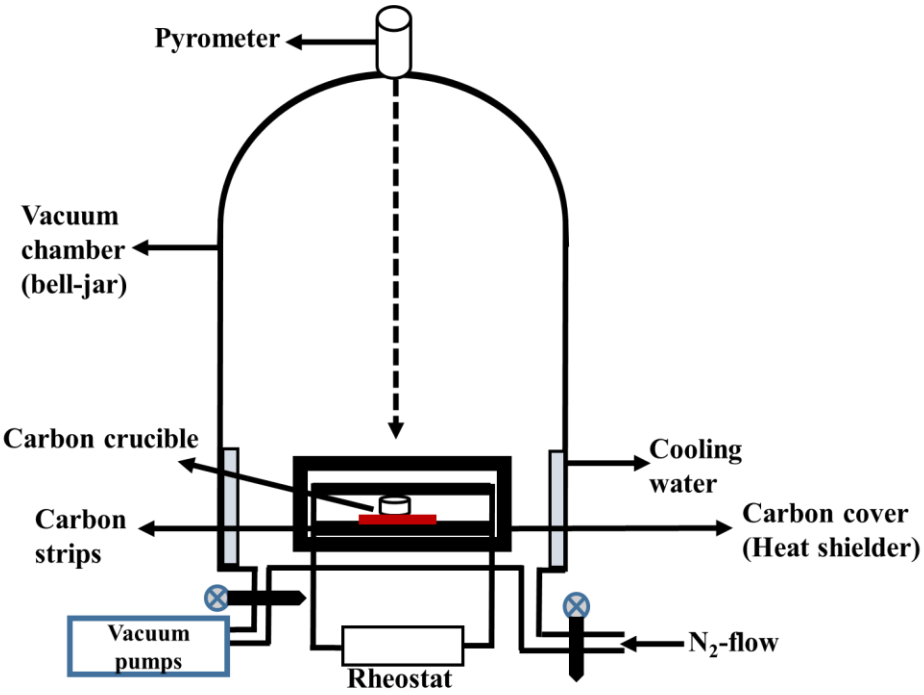

Figure 3.7. Schematics of the RTA system used in this research.

3.5 Ohmic Contacts

The contact between metal and semiconductor surface is defined as an ohmic contact when there is a negligible barrier between the Fermi level of the metal and the conduction band of the semiconductor so that there is an unrestricted two-way flow of charge carriers across the junction. Ideal ohmic contact exhibits a linear relationship between the output current and the applied voltage (*i.e.*, linear *I-V* characteristics) with a low contact resistance R_c. The lowest possible value of R_c facilitates the maximum output current. The contact resistance (R_c) of a metal-semiconductor junction for a highly doped semiconductor is given by[17]:

$$R_C = exp\left[\frac{2\sqrt{\varepsilon_S m^*}}{h}\left(\frac{\varphi_b}{\sqrt{N_D}}\right)\right] \tag{3.4}$$

where ε_S is the permittivity of the semiconductor, m^* is the effective mass of an electron, h is the Planck's constant, φ_b is the barrier height and N_D is the doping concentration.

The low contact resistance compared to the bulk resistance of the device is needed for an ideal ohmic contact to reduce the on-state voltage drop and the power dissipation during the current conduction. A classical n-type semiconductor ohmic contact is shown in Fig. 3.8 below. The combination of the proximity of the Fermi level to the conduction band and band bending at the interface allows the low contact resistance, linear *I-V* characteristic, proportional to the contact area. This is due to a combination of the low work function of the metal than the semiconductor, Fermi level pinning caused by electronic states at the M-S interface and the doping level in the semiconductor. Some of these variables can affect the Schottky barrier height. A thinner depletion region also allows the carriers to tunnel through the barrier contributing to improving the ohmic contact and barrier height can be lowered using suitable metal choice. Thermal annealing is a frequently used method to alloy the metal into the semiconductor which can also lower the barrier height.

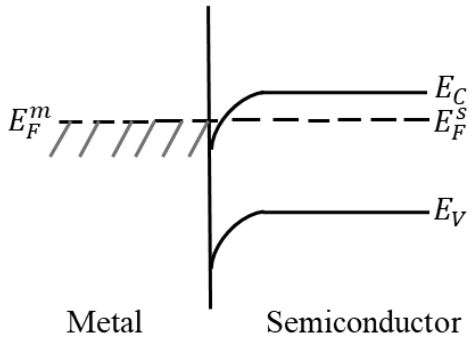

Figure 3.8. Energy band diagram for a metal-semiconductor interface with high n-type doping.

Smooth surface morphology and limited thickness of the ohmic contacts are very important parameters to take care of to avoid alignment problems in contact lithography. Ohmic contacts should be mechanically stable, *i.e.*, should not be scratched away during the electrical testing and wire bonding; they should not degrade due to the high temperature that can arise during the device operation.

In AlGaN/GaN HEMTs, ohmic contacts are formed by annealing the Ti/Al/diffusion layer/Au multilayer metal stacks.[18] Mostly used diffusion layer metals are Ni, Ti, Mo, Ir, and Pt.[19,20] The various metals in these schemes have their specific role. Titanium is the first metal layer and is believed to:

- serve as an adhesion layer to provide good mechanical stability,[21]
- dissolve the native oxides on the AlGaN surface,[21,22] and
- create nitrogen vacancies (V_N) by reacting with the nitrogen atoms in the AlGaN barrier layer introducing the donor states near the metal interface or in the AlGaN layer. Which makes the AlGaN layer underneath the contact highly doped thereby enabling electrons to tunnel through the remaining thin potential barrier which separates[21,23] them from the 2DEG.

The function of Aluminum is to:

- react with Ti to form an Al_3Ti layer which prevents oxidation of the underlying Ti layer,[21,23] and
- serves as a diffusion barrier for the Ni and Au layers as they form high Schottky barriers with the AlGaN layer.[21]

Using Ti/Al sequence, rather than a single Ti layer provides lower resistivity and work function compared to Ti only which helps to reduce the contact resistance. Al might diffuse into the contact interface and form AlN, which causes an increase in contact resistance.[24] Diffusion layer metals are used to prevent the penetration of Au intermixing with Al which forms a highly resistive alloy, generally called “purple plague.” Au is necessary to reduce the lateral resistivity, improve the conductivity of the metal stack and facilitate bridging with other devices.

During annealing metal, migrates down into the epi-layer, beyond the barrier and provide low resistance paths from 2DEG. For the ohmic contact formation in this dissertation work, Ti/Al/Ni (30/180/40 nm thickness) metal stacks were sputter deposited, and the rapid thermal annealing was performed at 850 ^{o}C for 30 seconds. Ohmic behavior was confirmed by *I-V* and transmission line model TLM characteristic measurements.

3.5.1 Transmission Line Model (TLM)

The transmission line model (TLM) is a commonly used model for the determination of the sheet resistance (R_s), the contact resistance (R_c), and the specific resistance (ρ_c). The total resistance (R_T) between two rectangular ohmic contacts in an array of identical contacts (shown in figure 3.9 (a)) with different (increasing separation) distances (d) between them is measured. The measured total resistance consists of several components:

$$R_T = 2R_m + 2R_C + R_{semi} \tag{3.5}$$

where R_m is the resistance due to the metal contact, R_C is associated with the M-S interface, and R_{semi} is the usual semiconductor resistance. The factor 2 comes because we measure the resistance of two contacts. For most of the situations, the resistance of the metals is so low that $R_C >> R_m$, therefore R_m can be ignored. And the semiconductor resistance is given as[25]:

$$R_{semi} = R_S \frac{d}{W} \tag{3.6}$$

and total resistance will be:

$$R_T = 2.R_C + d.\frac{R_S}{W} \tag{3.7}$$

where W is the width of the contacts.

After the resistance (R_T) is measured between the contacts pads, the R_T value is plotted against the separation (d) and the plot can be fitted with a linear curve as shown in Fig. 3.9 (b).

Using the above equation 3.7, the contact resistance R_C and sheet resistance R_S can easily be derived.

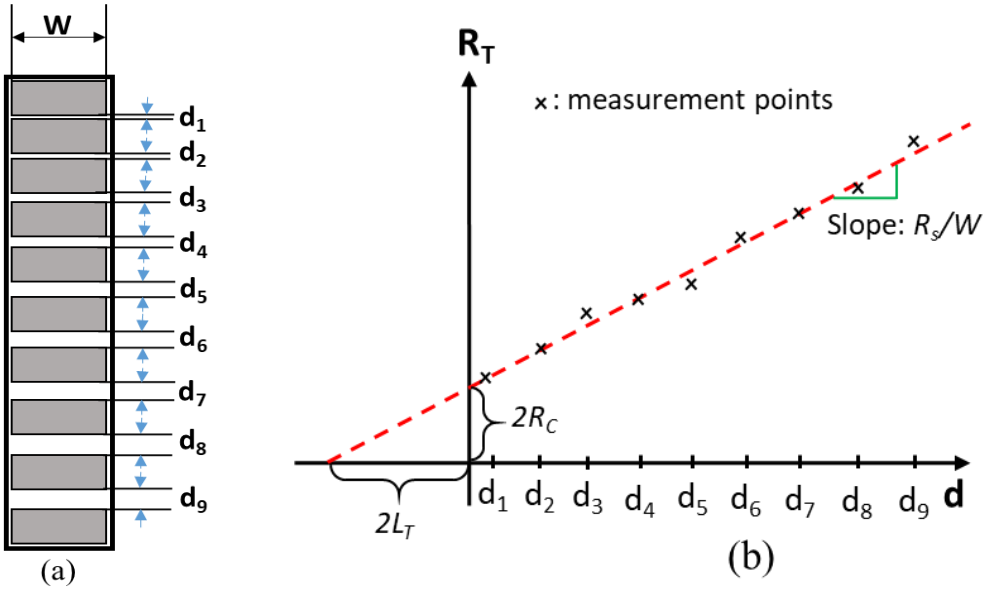

Figure 3.9. (a) Schematics of rectangular TLM structures (b) Representative plot of the resistance between the rectangular contacts and the distance between them.

At the edge of the contact, the current flowing in (or out) is significant. Moving away from that edge, the current drops off until, at the far edge, there is no current which is known as "current crowding." This current drops off exponentially with a characteristic length L_T, which is known as the transfer length which is the average distance that an electron (or hole) travels in the semiconductor beneath the contact before it flows up into the contact. The transfer length is related to the sheet resistance (R_S) and the specific resistance (ρ_c) as:

$$L_T = \sqrt{\frac{\rho_c}{R_S}} \tag{3.8}$$

L_T is determined at the intercept of the R_T vs. d graph when R_T is zero.

The effective area of the contact can be treated as $L_T.W$. And the contact resistance will be:

$$R_C = \frac{\rho_C}{L_T W} = \frac{R_S L_T}{W} \tag{3.9}$$

$$R_T = R_{semi} + 2R_C = \frac{R_S d}{W} + 2\frac{R_S L_T}{W} = \frac{R_S}{W}(d + L_T) \tag{3.10}$$

Thus, with the help of this equation and the plot in Fig. 3.9, we have everything required to calculate the specific contact resistance, ρ_C. The calculated value of ρ_C for the ohmic contact in this dissertation work is $7.14 \times 10^{-4}\ \Omega\ \text{cm}^{-2}$.

3.6 Schottky Contacts

Gate contacts in III-nitrides are generally Schottky contacts that act as capacitors when under bias, depleting the semiconductor region beneath the channel of free carriers and preventing the flow of charge between ohmic contacts. The rectifying behavior of a Schottky contact is due to the band properties of metal-semiconductor interfaces. The theory behind Schottky device operation is described earlier in chapter 2 section 2.2.2.3.

A Schottky gate electrode in AlGaN/GaN HEMTs is used to control the channel current by means of a field-effect transconductance. Theoretically, transconductance and leakage properties are limited by device geometry, semiconductor dielectricity, and Schottky barrier height. Rectifying behavior of n-GaN has been observed using Ti, Ag, Au, Pt, Pd, Ni, and Ir metals.[26,27,28] Au is commonly used to lower the lateral resistance and to prevent oxidation. Since the Ir contacts were more stable and scratch resistant than Ni contacts, Ir (15 nm thickness) was used for the gate metallization of transistor devices fabricated for the study in this dissertation. For SPIV measurements, semitransparent (10-15 nm) contacts of Ni were deposited on HEMT wafers. For this particular experiment, the light effect on Ni contact deposited devices was more significant than the Ir contact deposited devices which might be due to the variation on the reflectivity of the metals. Final yielded devices after all the fabrication steps are shown in the following Fig. 3.10.

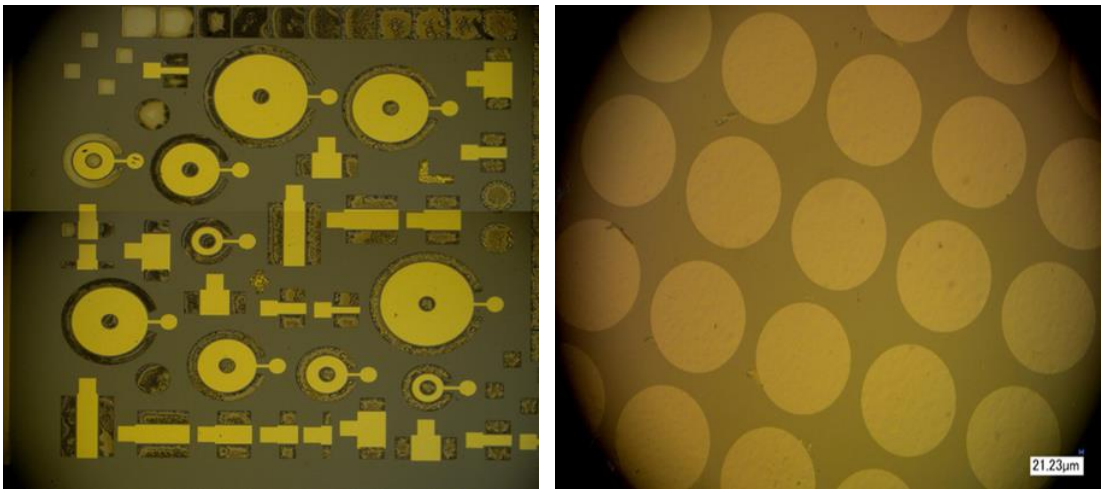

(a) (b)

Figure 3.10. Final products of the fabricated HEMTs (a) transistor devices (b) Schottky contacts.

3.7 Transistor Characteristics Measurements: Current-Voltage (*I-V*) and Capacitance-Voltage (*C-V*)

Transistor DC characteristics were measured on the H-100 Signatone probe station equipped with Keithley 24100 and 2400-source meters. Moreover, *C-V* measurements were performed using calibrated cables with Signatone S-725 micro-positioners. The used source meter and voltage sources were automated with LabVIEW program. All the measurements were performed in a dark condition at room temperature. Data were extracted with the help of LabVIEW program and analyzed using Origin software.

3.8 Spectroscopic Photocurrent Voltage (SPIV) Measurements

For III-V semiconductors, different types of trap characterization techniques have been established such as deep level transient spectroscopy (DLTS),[29] deep level optical spectroscopy (DLOS),[30] luminescence spectroscopy,[31] surface potential analysis,[32] and photoionization spectroscopy.[33] Different techniques detect the traps based on their response in the measured parameters such as change of terminal device characteristics under the pulse, energy characteristics, cross section of the traps, thermal relaxation time of terminal current, and decaying time constant.

Electronic and optical properties of semiconductors are affected by imperfections such as point defects, dislocations, and interfaces. Photoconductivity measurement is one of the established techniques to characterize defects in semiconductors. It is defined as the increase in conductivity of a material resulting from the absorption of optical photons. The basic process that governs the magnitude of photocurrent is the generation of free electrons and holes through the absorption of incident photons, their transport through the material under the influence of an electric field, and their recombination.[34] The study and analysis of the response on the photocurrent as a function of the illumination will offer insights into the structure, band-gap energy, excitonic transitions, crystal imperfections, defects and electronic properties of the material under the investigation.

The removal of a bound electron with the help of incident photon (electromagnetic radiation) is defined as photoionization.[35] In photoionization spectroscopy, electrons in the traps are excited with the incident photon having energy above-threshold trapping energy which releases the electrons from the traps and contribute to increase an output current.

$$\Delta + h\nu = \Delta^{+} + e \tag{3.11}$$

where Δ is the target atom in the lower state and the $\Delta^{+}$is the higher state (ionized) and e is the photoionized electron.

By analyzing the trapping and de-trapping of the charge carriers in the deep traps, the nature of the traps can be elucidated. Klein *et at.*[36] studied the wavelength dependence of drain current recovery on GaN transistors and reported the signature of specific trap levels responsible for the current collapse. In these techniques, the trapped carrier responsible for current collapse is released during the illumination of light, which reflects the photoionization spectrum of the traps. The spectrum

can be used to identify the defects by relating the increase in the number of carriers ejected from the traps upon illumination to the increase in the current.

Spectroscopic photocurrent-voltage (SPIV) measurement technique used in this research is a simplified version of the photoionization spectroscopy. It is a novel diagnostic technique developed in our lab to evaluate the distribution of in-gap states in Si-based HEMTs.[37] This method is complementary to photoluminescence (PL) which is sensitive to radiative transition only whereas SPIV is sensitive to both radiative and non-radiative transition of the charge carriers. Similar to the photoionization spectroscopy, bias is applied between two electrodes to fill the traps and fully collapsed output current is measured both under dark and various wavelengths (λ) of illuminated light for the pulse duration of *t* repeatedly. The difference between the dark and the illuminated output current at a given fixed bias (V_o) is calculated for each of the wavelengths. There will be an increment in the light illuminated output current in reference to the dark current, that difference represents the number of carriers untrapped from the traps due to the excitation of incident light.

The response function *S (λ)* is measured by normalizing the fractional increase;

$$\frac{[I(\lambda)]}{I_{dark}} = \frac{\Delta I(\lambda)}{I_{dark}} \tag{3.12}$$

in output current, which reflects the fraction of the traps emptied upon illumination by the total number of incident photons at each wavelength $\phi(\lambda)t$ (photon cm^{-2}) as follows[36,38]:

$$S(\lambda) = \left[\frac{\Delta I(\lambda)}{I_{dark}}\right]\left[\frac{1}{\phi(\lambda)t}\right] \tag{3.13}$$

where $\phi(\lambda)$ is the flux of incident photon, *t* is illumination time, $\Delta I(\lambda)$ is an increase in output current upon light illumination and I_{dark} is the dark current.

We employed a SPIV technique to characterize the irradiation-induced defects in Al-GaN/GaN HEMTs. The devices used for SPIV measurement were an array of semi-transparent (10-15 nm) circular Ni Schottky contacts with a diameter of 600 μm. Xenon lamp light source coupled with a monochromator was used for the illumination. Two ranges of wavelength of the illuminated light were used; sub-bandgap (800-400 nm) and above bandgap (280-400 nm) illumination by varying with the help of a stepping motor controlled monochromator. In the meantime, a Keithley 6487 picoammeter with a built-in voltage source was used to apply the bias to collect the photocurrent. The direction of current flow was vertical and was controlled by applying a reverse bias to the top Schottky contact with respect to the bottom ohmic contact (attached gold plate). LabVIEW program was used to collect and extract the data. Moreover, the measurements were performed in a dark condition at room temperature. The device was brought to the same state before each measurement step, *i.e.*, waited for enough and irradiated with a red light to ensure the elimination of depletion and returning to the equilibrium condition, ensuring the reproducibility of the results. The schematics of the SPIV system is shown in Fig. 3.11 below.

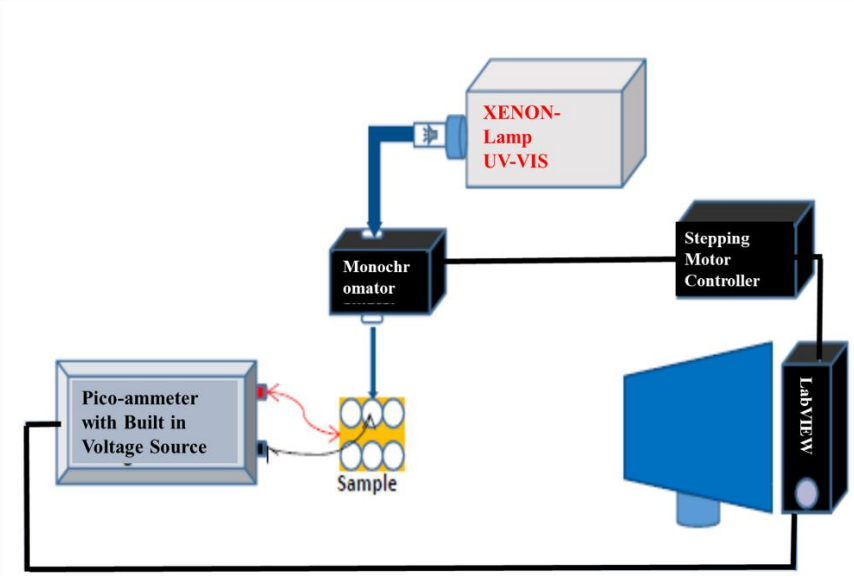

Figure 3.11. Schematics of spectroscopic photocurrent voltage measurement system.

3.8.1 Sub-bandgap SPIV

The sub-bandgap SPIV provides information about sub-bandgap energy levels of defects within the bandgap by relating the change in photocurrent level in response to the wavelength of the incident light.[37] It is capable of sequentially probing the traps with the different activation energy (from low to high deep level-to-band transition energy) by changing the wavelength of light from long to short wavelength. The wavelength of the incident light was varied in such a way that the higher energy levels were excited as the wavelength decreases (energy increases). When the light carrying photon with the energy above threshold trapping energy falls into the deep traps, the trapped carriers will be photoionized and released from those traps, leading to the deep level-to-band electronic transition of carriers, consequently increasing the output current.[39]

In this experiment, the wavelength of incident light was varied from 800 nm to 400 nm with a step of 50 nm. Carriers were excited from the deep traps and hence contributed to the photocurrent. The results of the experiment are described in chapter six and seven. The persistent photoconductivity phenomena are prevalent in GaN and related materials.[40] Therefore, sequential photocurrent measurement will produce a systematic reduction in photocurrent. If there are no sub-gap defects, the photo-IV spectra will simply follow the pattern of gradual reduction of photocurrent as the measurement is repeated. However, if there are sub-gap defects present, the distinct photocurrent spectra will be observed without following the systematic order of the wavelength. Therefore, sub-gap defects based on their activation energy levels can be detected.

3.8.2 Above bandgap SPIV

The above bandgap SPIV utilizes the fact that the penetration depth of light with a photon energy of above bandgap energy will gradually increase as the wavelength is increased.[41] In this experiment, the wavelength of ultra-violet (UV) light was varied from low to high (280 nm to 400

nm) at the steps of 10 nm. Therefore, the electrically active defects will be sequentially probed along the epi-layer growth direction (bottom to top). The physics of this technique is explained as below:

According to Beer-Lambert law;[42]

$$\frac{I}{I_0} = exp[-\alpha . d] \tag{3.13}$$

where α is the absorption coefficient, d is the distance from the surface of the material, and I and I_0 are the intensities of incident light measured at the depth and surface respectively. Also, the penetration depth (PD) is defined as the distance from the surface when the intensity of the light has decayed to $1/e$ (37%) of the original intensity. Thus, the penetration depth is given by;

$$\text{Penetration depth (PD)} = \frac{1}{\alpha} \tag{3.14}$$

This equation clarifies that, as the absorption coefficient is a function of the wavelength of light, PD is also the function of the wavelength of light. The absorption coefficient is related to extinction coefficient K and the wavelength of light λ as;

$$\alpha = \frac{4\pi K}{\lambda} \tag{3.15}$$

Figure 3.12 shows the variation of PD as a function of wavelength[43] in GaN and AlGaN.

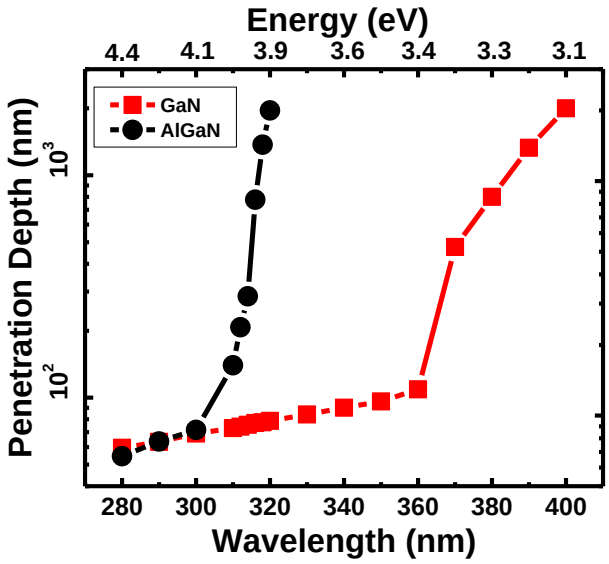

Figure 3.12. Variation of penetration depth as a function of wavelength in GaN (red/square) and AlGaN (black/circle).

Proton and gamma-ray irradiated samples were analyzed to characterize the in-depth distribution of defects within the bandgap, and the experimental results are reported in chapter six and seven. As discussed above, the incident photon energy is higher than the bandgap of the material; all the states in the bandgap are expected to be photoionized. Hence, the information about in-depth spatial distribution of irradiation induced in-gap states of the samples was obtained.

3.9 Persistent Photoconductivity

When light impinges on the semiconductor samples, the rise in photocurrent is observed due to the photoexcitation of carriers. In some of the II-VI[44] and III-V[45,46] semiconductors, the light-induced enhancement in the conductivity persists for a long period even after the termination of light excitation. This phenomenon is known as persistent photoconductivity (PPC) effect.[47] The carrier concentration is increased due to the photoexcited electrons which are transferred from deep-level donors to the conduction band when the light is turned on. After the light is turned off, the recombination of the electrons and ionized deep-level donors can be prevented by the local potential barrier around the deep-level donors which results in a persistent carrier concentration.

The PPC includes multiple processes such as photon absorption, carrier recombination, and transport.[48] In the case of GaN and AlGaN epilayers, PPC is ascribed to defect complexes such as gallium vacancies, nitrogen antisites, deep-level impurities, and interacting defect complexes. PPC in AlGaN/GaN heterostructures is claimed to arise from defect levels in both the AlGaN and GaN layers. However, the main contribution comes from the donor like centers in AlGaN barrier layer from which upon the photoexcitation electrons travel across the heterojunction fall into the triangular quantum well in the GaN side and contribute to the photocurrent and the barrier in 2DEG prevents the faster decay of it contributing to PPC.[40]

References

[1] Manasevit, H. M., F. M. Erdmann, and W. I. Simpson. "The use of metalorganics in the preparation of semiconductor materials IV. The nitrides of aluminum and gallium." *Journal of the Electrochemical Society* 118, no. 11 (1971): 1864-1868.

[2] Jones, Anthony C., and Michael L. Hitchman, eds. *Chemical vapour deposition: precursors, processes and applications*. Royal society of chemistry, 2009.

[3] Davis, R. F., S. M. Bishop, S. Mita, R. Collazo, Z. J. Reitmeier, and Z. Sitar. "Epitaxial growth of gallium nitride." In *AIP Conference Proceedings*, vol. 916, no. 1, pp. 520-540. AIP, 2007.

[4] Lewerenz, Hans-Joachim, and Laurie Peter, eds. *Photoelectrochemical Water Splitting: Materials, Processes and Architectures*. Royal Society of Chemistry, 2013.

[5] Sanganeria, Mahesh K., Mehmet C. Öztürk, Gari Harris, Katherine E. Violette, I. Ban, C. Archie Lee, and Dennis M. Maher. "Ultrahigh Vacuum Rapid Thermal Chemical Vapor Deposition of Epitaxial Silicon onto (100) Silicon I. The Influence of Prebake on (Epitaxy/Substrate) Interfacial Oxygen and Carbon Levels." *Journal of the Electrochemical Society* 142, no. 11 (1995): 3961-3969.

[6] E. H. Rhoderick and R. H. Williams, *Metal-semiconductor contacts*, 2nd ed. Oxford [England]: Clarendon Press ; New York : Oxford University Press, 1988.

[7] Shul, RJa, GAa Vawter, CGa Willison, MMa Bridges, JWb Lee, SJb Pearton, and C. R. Abernathy. "Comparison of plasma etch techniques for III–V nitrides." *Solid-State Electronics* 42, no. 12 (1998): 2259-2267.

[8] Smith, L. L., S. W. King, R. J. Nemanich, and R. F. Davis. "Cleaning of GaN surfaces." *Journal of Electronic Materials* 25, no. 5 (1996): 805-810.

[9] King, S. W., J. P. Barnak, M. D. Bremser, K. M. Tracy, C. Ronning, R. F. Davis, and R. J. Nemanich. "Cleaning of AlN and GaN surfaces." *Journal of Applied Physics* 84, no. 9 (1998): 5248-5260.

[10] Diale, M., F. D. Auret, N. G. Van der Berg, R. Q. Odendaal, and W. D. Roos. "Analysis of GaN cleaning procedures." *Applied Surface Science* 246, no. 1-3 (2005): 279-289.

[11] Mack, Chris. *Fundamental principles of optical lithography: the science of microfabrication*. John Wiley & Sons, 2008.

[12] Rothschild, Mordechai, Theodore M. Bloomstein, Theodore H. Fedynyshyn, Roderick R. Kunz, Vladimir Liberman, Michael Switkes, Nikolay N. Efremow et al. "Recent trends in optical lithography." *Lincoln Laboratory Journal* 14, no. 2 (2003): 221-236.

[13] Campbell, Stephen A. "The Science and Engineering of Microelectronic Fabrication (The Oxford Series in Electrical and Computer Engineering)." (2001).

[14] Elshabini, Aicha, Aicha AR Elshabini-Riad, and Fred D. Barlow. *Thin film technology handbook*. McGraw-Hill Professional, 1998.

[15] John, P. I. *Plasma sciences and the creation of wealth*. Tata McGraw-Hill Education, 2005.

[16] Edward, T. Yu. *III-V nitride semiconductors: Applications and devices*. Vol. 16. CRC Press, 2002.

[17] Sze, S. M., and K. K. Ng. "Physics of Semiconductor Devices 3rd Edition, John Wiley & Sons." *Inc., NJ*: 164.

[18] Van Daele, B., G. Van Tendeloo, W. Ruythooren, J. Derluyn, M. R. Leys, and M. Germain. "The role of Al on Ohmic contact formation on n-type GaN and AlGaN⁄GaN." *Applied Physics Letters* 87, no. 6 (2005): 061905.

[19] Greco, Giuseppe, Ferdinando Iucolano, and Fabrizio Roccaforte. "Ohmic contacts to Gallium Nitride materials." *Applied Surface Science* 383 (2016): 324-345.

[20] Fitch, R. C., J. K. Gillespie, N. Moser, T. Jenkins, J. Sewell, D. Via, A. Crespo et al. "Properties of Ir-based Ohmic contacts to AlGaN/GaN high electron mobility transistors." *Applied physics letters* 84, no. 9 (2004): 1495-1497.

[21] Ruvimov, S., Z. Liliental-Weber, J. Washburn, D. Qiao, S. S. Lau, and Paul K. Chu. "Microstructure of Ti/Al ohmic contacts for n-AlGaN." *Applied Physics Letters* 73, no. 18 (1998): 2582-2584.

[22] Liu, Q. Z., and S. S. Lau. "A review of the metal–GaN contact technology." *Solid-State Electronics* 42, no. 5 (1998): 677-691.

[23] Liu, Q. Z., L. S. Yu, F. Deng, S. S. Lau, Q. Chen, J. W. Yang, and M. A. Khan. "Study of contact formation in AlGaN/GaN heterostructures." *Applied physics letters* 71, no. 12 (1997): 1658-1660.

[24] Motayed, Abhishek, Ravi Bathe, Mark C. Wood, Ousmane S. Diouf, R. D. Vispute, and S. Noor Mohammad. "Electrical, thermal, and microstructural characteristics of Ti/Al/Ti/Au multilayer Ohmic contacts to n-type GaN." *Journal of applied physics* 93, no. 2 (2003): 1087-1094.

[25] Schroder, Dieter K. *Semiconductor material and device characterization*. John Wiley & Sons, 2006.

[26] Schmitz, A. C., A. T. Ping, M. Asif Khan, Q. Chen, J. W. Yang, and I. Adesida. "Schottky barrier properties of various metals on n-type GaN." *Semiconductor Science and Technology* 11, no. 10 (1996): 1464.

[27] Arulkumaran, Subramaniam, Takashi Egawa, Guang-Yuan Zhao, Hiroyasu Ishikawa, Takashi Jimbo, and Masayoshi Umeno. "Electrical characteristics of Schottky contacts on GaN and Al0. 11Ga0. 89N." *Japanese Journal of Applied Physics* 39, no. 4B (2000): L351.

[28] Jessen, G. H., R. C. Fitch, J. K. Gillespie, G. D. Via, N. A. Moser, M. J. Yannuzzi, A. Crespo, R. W. Dettmer, and T. J. Jenkins. "Gate optimization of AlGaN/GaN HEMTs using WSi, Ir, Pd, and Ni Schottky contacts." In *25th Annual Technical Digest 2003. IEEE Gallium Arsenide Integrated Circuit (GaAs IC) Symposium, 2003,* pp. 277-279. IEEE, 2003.

[29] Götz, W., N. M. Johnson, H. Amano, and I. Akasaki. "Deep level defects in n-type GaN." *Applied physics letters* 65, no. 4 (1994): 463-465.

[30] Korotkov, R. Y., J. M. Gregie, and Bruce W. Wessels. "Optical properties of the deep Mn acceptor in GaN: Mn." *Applied Physics Letters* 80, no. 10 (2002): 1731-1733.

[31] Bradley, Shawn T., Alexander P. Young, Leonard J. Brillson, Michael J. Murphy, William J. Schaff, and L. E. Eastman. "Influence of AlGaN deep level defects on AlGaN/GaN 2-DEG carrier confinement." *IEEE Transactions on Electron Devices* 48, no. 3 (2001): 412-415.

[32] Koley, Goutam, Vinayak Tilak, Lester F. Eastman, and Michael G. Spencer. "Slow transients observed in AlGaN/GaN HFETs: effects of SiN/sub x/passivation and UV illumination." *IEEE Transactions on Electron Devices* 50, no. 4 (2003): 886-893.

[33] Klein, P. B., S. C. Binari, J. A. Freitas Jr, and A. E. Wickenden. "Photoionization spectroscopy of traps in GaN metal-semiconductor field-effect transistors." *Journal of Applied Physics* 88, no. 5 (2000): 2843-2852.

[34] Petritz, Richard L. "Theory of photoconductivity in semiconductor films." *Physical Review* 104, no. 6 (1956): 1508.

[35] Amusia M.Y. (1996) Theory of Photoionization. In: Becker U., Shirley D.A. (eds) VUV and Soft X-Ray Photoionization. Physics of Atoms and Molecules. Springer, Boston, MA.

[36] Klein, P. B., J. A. Freitas Jr, S. C. Binari, and A. E. Wickenden. "Observation of deep traps responsible for current collapse in GaN metal–semiconductor field-effect transistors." *Applied Physics Letters* 75, no. 25 (1999): 4016-4018.

[37] Tong, Fei, Kosala Yapabandara, C-W. Yang, Min Khanal, Chunkun Jiao, M. Goforth, B. Ozden et al. "Spectroscopic photo I–V diagnostics of nitride-based high electron mobility transistor structures on Si wafers." *Electronics Letters* 49, no. 24 (2013): 1547-1548.

[38] Klein, P. B. "Photoionization spectroscopy in AlGaN/GaN high electron mobility transistors." *Journal of applied physics* 92, no. 9 (2002): 5498-5502.

[39] Ozden, Burcu, Min P. Khanal, Suhyeon Youn, Vahid Mirkhani, Kosala Yapabandara, Minseo Park, Ming Zhao, Hu Liang, Prem Kumar Kandaswamy, and Y. N. Saripalli. "Analysis of Point Defect Distributions in AlGaN/GaN Heterostructures via Spectroscopic Photo Current-Voltage Measurements." *ECS Journal of Solid State Science and Technology* 5, no. 4 (2016): P3206-P3210.

[40] Li, J. Z., J. Y. Lin, H. X. Jiang, M. Asif Khan, and Q. Chen. "Persistent photoconductivity in a two-dimensional electron gas system formed by an AlGaN/GaN heterostructure." *Journal of applied physics* 82, no. 3 (1997): 1227-1230.

[41] Muth, J. F., J. Dd Brown, M. A. L. Johnson, Zhonghai Yu, R. M. Kolbas, J. W. Cook, and J. F. Schetzina. "Absorption coefficient and refractive index of GaN, AlN and AlGaN alloys." *Materials Research Society Internet Journal of Nitride Semiconductor Research* 4, no. S1 (1999): 502-507.

[42] Swinehart, D. F. "The beer-lambert law." *Journal of chemical education* 39, no. 7 (1962): 333.

[43] Ozden, Burcu, Chungman Yang, Fei Tong, Min P. Khanal, Vahid Mirkhani, Mobbassar Hassan Sk, Ayayi Claude Ahyi, and Minseo Park. "Depth-resolved ultra-violet spectroscopic photo current-voltage measurements for the analysis of AlGaN/GaN high electron mobility transistor epilayer deposited on Si." *Applied Physics Letters* 105, no. 17 (2014): 172105.

[44] Jiang, H. X., and J. Y. Lin. "Persistent photoconductivity and related critical phenomena in Zn 0.3 Cd 0.7 Se." *Physical Review B* 40, no. 14 (1989): 10025.

[45] Lang, D. V., R. A. Logan, and M. Jaros. "Trapping characteristics and a donor-complex (DX) model for the persistent-photoconductivity trapping center in Te-doped Al x Ga 1− x As." *Physical Review B* 19, no. 2 (1979): 1015.

[46] Queisser, H. J., and D. E. Theodorou. "Decay kinetics of persistent photoconductivity in semiconductors." *Physical Review B* 33, no. 6 (1986): 4027.

[47] Dang, X. Z., C. D. Wang, E. T. Yu, K. S. Boutros, and J. M. Redwing. "Persistent photoconductivity and defect levels in n-type AlGaN/GaN heterostructures." *Applied physics letters* 72, no. 21 (1998): 2745-2747.

[48] Buyanov, A. V., J. P. Bergman, J. A. Sandberg, B. E. Sernelius, P. O. Holtz, J. Dalfors, B. Monemar, H. Amano, and I. Akasaki. "Photoconductivity in n-type modulation-doped GaN/AlGaN heterostructures." *Journal of crystal growth* 189 (1998): 753-757.

Chapter 4

Radiation and its Effect in Semiconductors

4.1 Introduction

This chapter discusses the effects of energetic particle radiation on semiconductor materials. The types of damage the radiating particles can produce, and the nature of the defects will also be presented. We mainly focus our discussion on the gamma-ray, and proton irradiation effects on AlGaN/GaN HEMTs and their potential endurance towards these vulnerable radiations, based on their material structure and intrinsic properties will also be discussed. The sources of radiation and method used to irradiate the HEMTs will also be briefly mentioned at the end of the chapter.

4.2 Radiation Environment and Application of Electronics

Radiation study has been a key to link solid state physics and high energy physics when it comes to the investigation of interaction of energetic particle with solids in an interdisciplinary research. Once the application of semiconductor technology began to be used in space missions and military applications, it became a matter of urgency to study the effects of radiation on the semiconductor devices. Space comes in front when we mention about the application of electronics in radiation environments. The other radiation environments include plasma fusion facility, high-energy physics experiments, nuclear reactors, *etc*. Space and military applications involve the radiation-harsh environment. The fabrication and testing process of electronic devices may also suffer through ionizing radiation. When a radioactive isotope of a radioactive element goes under nuclear decay due to lack or surplus of neutrons, it may result in the production of beta particles, alpha particles or gamma-rays. These are the primary source of radiation for the terrestrial environment. On the other hand, the primary sources of energetic particles in a space environment are: protons and electrons trapped in the Van Allen belts, heavy ions and transient particles which

include protons and heavy ions of all the elements of periodic table trapped in magnetosphere, galactic cosmic ray protons, protons, heavy ions, electrons and alpha particles produced from solar events such as coronal mass ejections and flares.[1] A representative sketch of the space radiation environment is shown in Fig. 4.1.

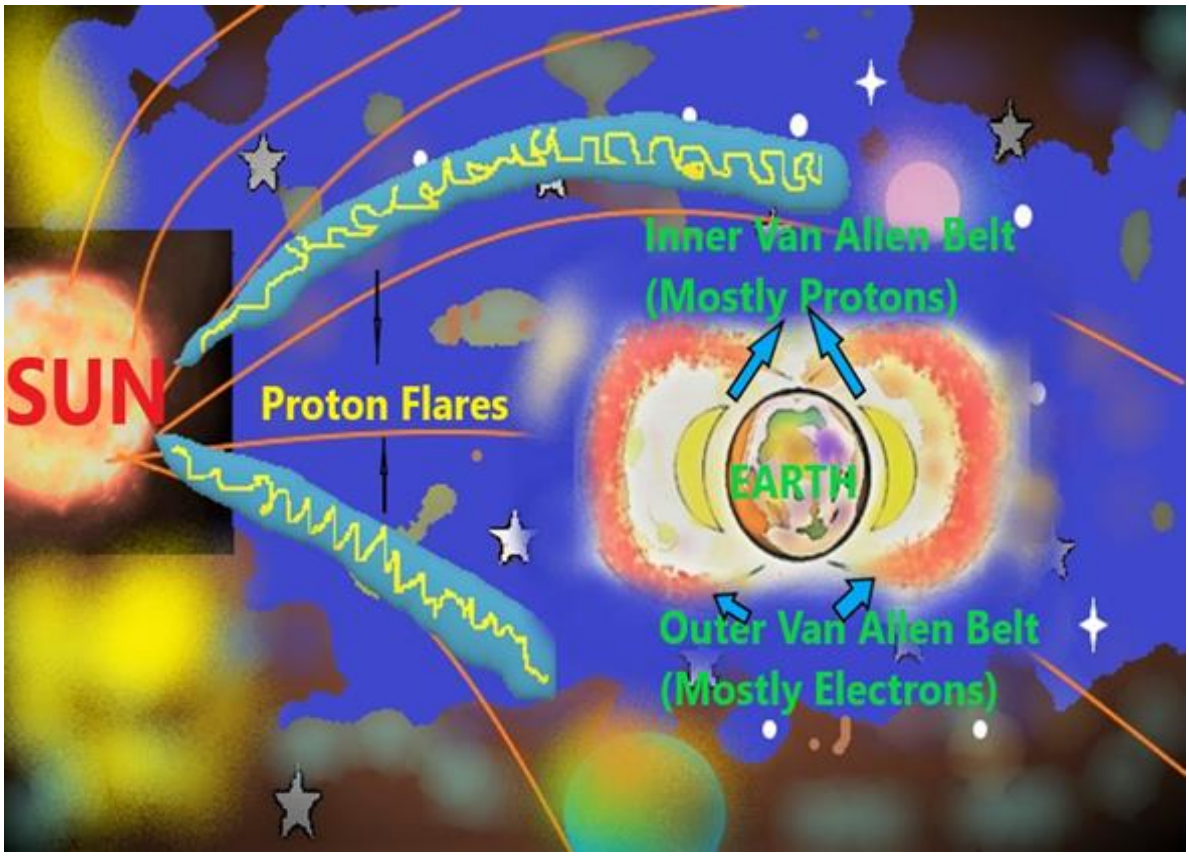

Fig. 4.1. A representative sketch of the space radiation environment.

In the space environment, the main source of radiation is a solar activity which consists of different kinds of particles with energies ranging from keV to GeV and beyond. The Earth's magnetosphere is bombarded by the flux of energetic charged particles constituting 85% of protons, 14% of α-particles, and 1% of other heavier ions of all the elements of periodic table. When they pass through the solar system, most of them are trapped in the magnetic fields of the Earth where their motion is controlled by Lorentz force. Such trapped regions of high energy radiation particles are known as Van Allen belts.[2] There are two radiation belts called the inner belt and outer belt.

The inner belt extends from 100s of km to 6000 km (low altitude) and consists of mainly energetic protons of energy up to 600 MeV together with the electrons up to several MeV. While the outer belt extends at high altitude of up to 60,000 km is comprised of primarily electrons. In addition, there is a plasma filling the entire space, consisting of mainly protons and electrons with energies up to about 100 keV and fluxes around 10^{12} $cm^{-2}s^{-1}$. Therefore, radiation tolerance is critical for electronic devices that are deployed for space applications.

On the other hand, the high energy physics experimental station such as Large Hadron Collider (LHC) at CERN uses high energy protons and electrons to study the elementary particles such as bosons, muons, and quarks.[3] Most of the nuclear reactors involve very high doses and fluxes of gamma-rays (above 1 MRad (Si)) and neutrons. Electronics that are being used in such reactors must be radiation tolerant of preventing the failure of the process. In the natural environment, main source of ionizing radiation is α-particles coming from the radioactive impurities such as uranium and thorium and their byproducts used during the semiconductor processing. In the upper atmosphere, neutrons are generated when atmospheric nitrogen interacts with the cosmic rays protons, part of these neutrons reach to the ground and may affect the high-speed electronic devices.

Various radioactive materials are present in the semiconductors such as actinides that emit α-particles through normal radioactive decay. The concentration of the impurities is however very low that present in metallization, contact metals, packages and even within the semiconductor itself. Also, the modern electronic devices are fabricated following the steps such as ion-implantation, dry etching, e-beam, x-ray lithography, sputtering, ion milling, *etc*. that can introduce radi-

ation damage on them.[4] Electronic devices are shrinking in size with the development of technology, the ultra-thin dielectric is being used in those devices which have higher probability of being damaged due to radiations while they are used in radiation harsh environments.

Therefore, considering the practical application of microelectronic devices both in terrestrial and space environments, their exposure to high energy radiation is unavoidable. One of the practices that are being done is shielding of the core electronic component of the system.[5] However, shielding is falling out of the scope because of many factors one of them is that shielding will add weight and require more volume in the system design and for the space applications, weight and volume are vital factors to consider. Hence, the best choice would be to develop/explore the material that is radiation tolerant and can perform without failure.

4.3 Radiation Effects in Semiconductors and Types of Damages

As discussed above, electronics that needs to operate in a radiation environment get bombarded with the energetic particles of very high energy. So, these energetic particles including protons, electrons, and heavy charged particles may lose their kinetic energy on their trajectory and can cause permanent damage to the material in their path. The degree and nature of damage depend on the dose, energy, type of energetic particle exposed to, and type of material. Irradiation can produce lattice defects, introduce impurities thereby degrading the material causing serious degradation in their performance.

Broadly the nature of damage can be categorized as ionizing and displacement. Ionizing damage is that in which free electron-hole pairs are generated by disrupting electronic bonds. In the case of displacement damage atoms are displaced from their usual lattice site leaving behind a vacancy. To cause the displacement damage much higher energy is required than causing the ionization damage. Other types of radiation effects include single event effect (SEE) and single event

upset (SEU). SEEs are caused by a single energetic particle, and can occur in many forms and is discussed in details in section 4.3.3. SEUs are soft, non-destructive type of errors which normally appear as transient pulses in logic or support circuits, or as bit flips in memory cells. The effects on materials from the natural space radiation environment may be divided into two categories; long term and short term effects. Long term effects can be ionizing and non-ionizing damages whereas short term effects are primarily concerned with single particle ionization and/or secondary particle formation. Occasionally, short term effects might be permanent. Therefore, space ionizing radiation effects can be viewed in two parts: total ionizing dose (TID) and SEE. Different types of damages are briefly discussed in the following subsections.[6]

When an energetic particle (ion) or photon travels through a solid system, it can lose energy in a number of ways that the amount of energy deposited to the solid not only depends on the projectile's mass and energy but also on the atomic number and mass of the target material. The amount of energy deposited per gram of the material is called the dose (D) and expressed in the units of rads or Grays. 1 rad = 100 erg/g = 6.62×10^{13} eV/g and 1 Gray =1 J/Kg = 100 rads. The energy loss also depends on the density of the target, *i.e.* the mass absorption coefficient is not the same for different materials.[7] Therefore, the material in which the total dose was deposited needs to be included for these units [(120 MRad (Air) ~132 MRad (GaN)]. The particle density impinging on the material per unit area and time is called the flux (ϕ, unit: particles cm^{-2} s^{-1}), the integrated flux over the total exposure time is called the fluence (Φ) with the unit particle/cm^2.

4.3.1 Ionizing Damage

An incoming charged radiation particle interacts with the electrons in the target material losing the energy (called ionization loss) which is transferred to an electron. Therefore, an electron absorbs the energy in the valence band and jumps to the conduction band, creating a corresponding

hole in the valence band. Thus, an electron-hole pair is created in the material. The number of electron-hole pair production depends on the energy required for creating a pair. The charged particles such as α, β and proton induce direct ionization while neutral radiations such as gamma-rays and neutrons cause indirect ionization to the material. Nature of bonding of the material determines the susceptibility of the ionization. For the materials with the metallic and ionic bonds, the ionization damage is not permanent but for the materials that possess covalent bond, ionization can easily separate them into their constituent atoms or radicals, leading to the permanent damage.[8]

4.3.2 Total Ionizing Dose (TID)

Total ionizing dose (TID) is a long-term effect which results in a charge build-up at the interfacial regions or boundaries between two different layers due to the ionization of the atoms causing degradation of electronics.[9] Typical effects of TID in semiconductor include threshold voltage shift, increase in leakage current, alternation in the channel carrier, crystal quality degradation, *etc*. Primary sources of TID in the space environment include trapped electrons and protons in the radiation belts and solar protons and secondary particles arising from interactions between these primary particles. Circuit failure is the common TID effect observed in the electronics due to the gradual shift of the parameters.

In semiconductor devices, insulator films are used as barrier layers and to arrest the charge motion between two layers of the semiconductor or conductor. The main threat of high energy, as well as low energy radiation particles to electronic and optoelectronic devices, is that it may: temporarily lower energy barriers and trap some of the charges traveling across the oxide and freeze them in place, producing a semi-permanent charge sheet. This charge sheet will have its own built-in electric field which will cause band bending and will affect the conductivity in charge sensitive

layer around it. Additionally, TID also affects the bonding between insulator-semiconductor interfaces.

AlGaN/GaN HEMTs are relatively immune to TID effects because of the absence of oxide which can trap charges easily.

4.3.3 Single Event Effect (SEE)

Single event effects (SEEs) result from ionization by a single particle as it passes through a critical junction of an electronic device. This event can alter the operational state of a device such as a logic state of a transistor. Environmental sources considered for SEEs include galactic cosmic rays, alpha particles, protons, and neutrons.[10] The SEEs to be considered are single-event upset (SEU)[11] and its example can be taken as unplanned change in a logic state of a digital electronic device. Similary, single-event latch-up (SEL); in this case the device is latched into one logic state and will not change states in response to a logic signal and this happens when SEU activates a parasitic circuit in the device[12]. And another SEE is single-event burnout (SEB); in this case, the current is not limited and device is destroyed, this mainly occurs in power MOSFETs and is the most dangerous form of SEE since it leads to a permanent failure and other types of SEEs are single-event gate rupture (SEGR), and single-event transients (SET).[13]

SEEs are mainly divided into two categories: soft errors and hard errors. Soft errors occur when a transient pulse or bit flip in the device causes an error that appears in the device output characteristics. So, they can be analyzed through their impact on the device output characteristics. Hard errors are not necessarily physically destructive to the device but may cause permanent functional effects.[14]

4.3.4 Non-ionizing Damage (Displacement Damage)

The atomic displacement occurs when an incident particle with the sufficient kinetic energy collides to a target material, it transfers enough energy to move the target atom from its normal lattice position to another position, creating a vacancy in the lattice.[15] The displaced atom resides in an interstitial position, and such one-atom disorder in a crystalline solid is called a point defect (Frenkel defect). This phenomenon caused by the incoming radiation particle is referred to as displacement damage. This type of damage is cumulative, long-term non-ionizing damage caused primarily due to protons, electrons, and neutrons. The amount of displacement damage is dependent on the incident particle type, its energy, and target material.[16] Figure 4.2 below is demonstrating the schematics of the displacement damage causing vacancy and interstitial.

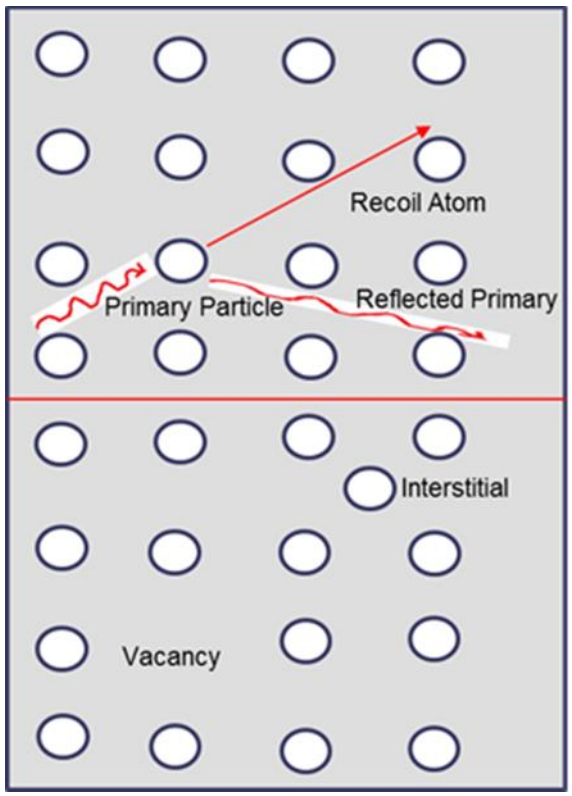

Fig. 4.2. Schematics of displacement damage in a crystal, illustrating the atomic displacement event: vacancy and interstitial.

When the energetic particles scatter off-lattice atoms, locally deforming the material structure, the bandgap structure may change, affecting the fundamental properties of the semiconductor. Primary defects caused due to displacement damage are vacancies, interstitials, Frenkel pairs, antisites and increase in recombination center. The atomic displacement damage initiates when the transferred kinetic energy from the incident particle surpasses the atomic threshold displacement energy (E_d) of the given particular element or compound.[17] This energy is defined as the minimum energy required to displace an atom from its lattice site in a crystal.

The interstitials and vacancies created due to the displacement of an atom from its native site are mobile at sufficiently high temperature due to the increased vibration of the atoms in the lattice with supplied thermal energy. Therefore, the interstitial atoms migrate to the vacancies giving rise to a recombination process.[18] It is reported that in some semiconductors, the annealing process can fix the induced defects due to the displacement damage.[19]

4.3.5 Impurity Production

Electrical and mechanical properties of a semiconductor device are altered by the imperfections induced in the crystal lattice caused by impurities introduced by radiating particles. Particles like electrons and photons can impose the impurities by means of breaking the chemical bonds of the semiconductors. When protons and alpha particles impinge in the semiconductor material, they capture an electron and transform into hydrogen and helium respectively. During the process, they exert pressure on the neighboring atoms causing swelling and blisters in the material.

Neutron also imposes an impurity, when neutrons get captured by a nucleus it forms a new isotope of the element which might be a radioactive isotope and will go to a decay resulting in the different chemical species.

4.3.6 Energy Deposition

An energetic ion penetrating a solid surface goes through elastic collision with the target nuclei and inelastic collision with the electron system. Therefore, it suffers from successive loss of energy during the course. Basically, here the transfer of energy takes place from incoming energetic particle to the target atom. Therefore, most of the radiations impose the energy deposition through the ionization process in compensation for their initial energy.[20] In the case of organic materials, the absorbed energy is mostly used in breaking the chemical bonds while in metals, it appears in the form of heat.

4.4 Gamma-rays and their Interaction with Materials

When a radioactive nucleus decays from its excited state to a lower ground state, it emits electromagnetic radiation. Gamma rays are photons or quanta of high energy electromagnetic radiation emitted during the decay of a radioactive nucleus. In the spectrum of electromagnetic radiation, gamma-rays fall above soft x-rays and have frequencies of greater than 10^{19} Hz. These are the highest em-radiation with average energy greater than 100 keV and wavelength of less than 10 picometers. Gamma-rays interact with matter in three different ways and cause ionization damage: photoelectric effect, Compton scattering, and pair production. On the other hand, charged particles such as protons, electrons, and alpha particles interact by Coulomb scattering causing both ionization and displacements.[21]

Photoelectric effect prevails for low energy photons in which the incident gamma-ray is completely absorbed by a tightly bound atomic electron in K or L shells, and the bound electron is ejected from the atom which is called a photoelectron. Compton scattering occurs for the gamma-rays of higher energies than 0.1-1 MeV depending upon the Z number of the target atom, and it involves an elastic collision with a loosely bound or free electron. However, if the energy of

the incident gamma-ray is high enough scattering can also scatter the bound electrons. In Compton scattering, incident gamma ray photon scatters with reduced energy and the lost energy is transferred to the kinetic energy of the scattered electron. Pair production also prevails for gammas with energies higher than 0.1-1 MeV. In pair production, when gamma-rays pass near a nucleus, it converts into an electron-positron pair. In Si, for the gamma-rays interaction with energy less than 50 keV, photoelectric effect is the dominating phenomena, for energies greater than 20 MeV pair production dominates and Compton scattering dominates at the interval of above energy ranges.[22]

Almost all kind of energetic particles matter interactions generate secondary gamma-photons in the material. And the interaction of ^{60}Co gamma-ray photons with GaN generate Compton electrons with a mean energy of about 600 keV which can dissipate the energy to create a large number of electron-hole pairs.[23] In this respect, gamma-irradiation is equivalent to internal electron irradiation.

The main sources of gamma-rays are radioactive nuclides. The natural sources of gamma rays on the Earth are from the results of radioactive decay and secondary radiation from atmospheric interactions with cosmic ray particles. Also, there are other natural sources, such as terrestrial gamma-ray flashes, that produce gamma-rays from electron action upon the nucleus.[24] The most useful radionuclides for the source of gamma-rays are: cobalt-60 (^{60}Co), cesium-137 (^{137}Cs), technetium-99m (^{99m}Tc), americium-241(^{241}Am), iodine-125 (^{125}I) and iodine-131 (^{131}I). In our experiment, the source we used was ^{60}Co which undergoes decay emitting two-photon lines of energies 1.1732 MeV and 1.3325 MeV with an average of 1.25 MeV.[25] The decay scheme of ^{60}Co is shown in Fig. 4.3 below. The advantages of ^{60}Co gamma-rays over other ionizing radiations include: the created defects on the material are uniformly distributed throughout relatively large specimens, and no secondary radiation is induced by interaction of the material with gamma-rays

at the maximum energy of 1.3325 MeV, and, therefore the samples can be safely handled after the irradiation.

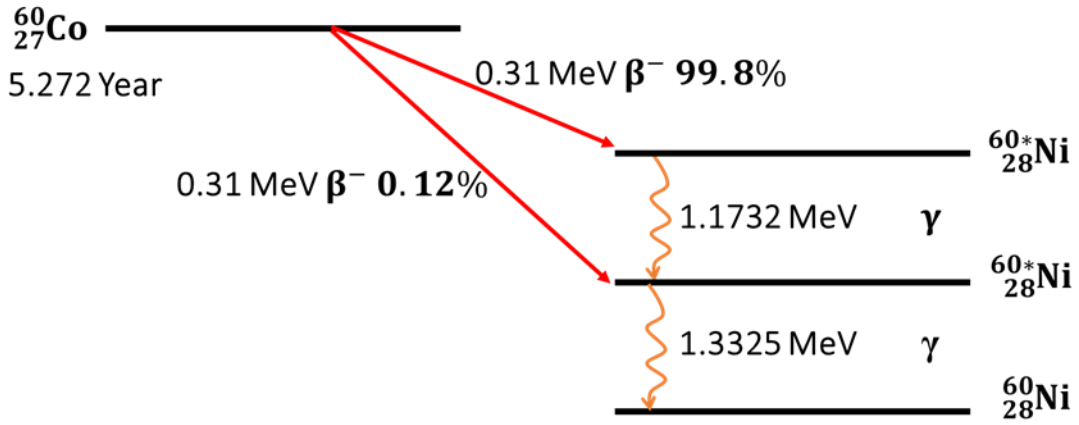

Fig. 4.3. Decay scheme of ^{60}Co radioactive nuclei.

The possible gamma-ray irradiation-induced effects in III-nitrides are the activation of dislocation-related defects, acting as sinks and sources of point defects during irradiation,[26,27] displacement damage: shallow nitrogen vacancy donor like defects,[28] ionization of pre-existing defects by injecting of photo-generated electrons into the channel and trapping of photo-generated holes in the III-N region.[29,30]

For this dissertation work, a high dose (120 MRad) gamma-ray irradiation effects on AlGaN/GaN HEMTs were investigated utilizing material and electrical characterization techniques. SPIV technique was used for the defect analysis. The gamma-ray dose in a material can be calculated using the following relation:

$$D^{material}(in\ Rads) = D^{air}\left(\frac{\mu^{en}}{\rho}\right)^{material} \Big/ \left(\frac{\mu^{en}}{\rho}\right)^{air} \qquad (4.1)$$

where $\left(\frac{\mu^{en}}{\rho}\right)$ is the mass absorption coefficient in cm^2/gm, $D^{material}$ is dose in a particular material in rads. For example: 1 Rad (Si) = 1.095 Rad (GaN).

For the irradiation, ^{60}Co source stored approximately 20-25 foot deep well of water (used for shielding purposes) during non-exposure was used. The ^{60}Co source was remotely brought out

of the water-filled radiation shielding well to irradiate the samples. The American Society for Testing Materials (ASTM) standard and guidelines were used to define the proper dosimetry system and confirmed the field uniformity and intensity of the gamma-rays coming from ^{60}Co panoramic irradiator. MAXX 4000 Standard Imaging Dosimeter was used to measure the dose-rate. The dosimeter was calibrated by comparison to a NIST source using a scintillation detector. During 57 days, a number of samples contained in plastic trays were subjected to ^{60}Co-derived gamma radiation energies of 1.17 MeV and 1.33 MeV. The dose rate was 24.35 Rad/second. The samples were placed in the high-flux region of the irradiator and were exposed continuously with interruptions weekly for source pool maintenance only. The final cumulative dose calculated was 120 MRad. The analysis of the results of the gamma-ray irradiation experiment is presented in chapter six.

4.5 Protons and their Interaction with Materials

A proton is an energetic particle which when accelerated and hits the material, can cause different types of damages in the material. The highly energetic particle will be slowed down by multiple collisions with the atoms and electrons of the target. This process is known as nuclear stopping or electronic stopping which is responsible for the structural defects in the target material. The damage production is dependent on the electronic structure of the target. The energy deposition from proton exposure goes into both displacement and ionization processes. Displacement damage causes increased bulk recombination whereas ionization damage causes surface recombination.[6]

Non-ionizing energy loss by proton includes four different effects: elastic coulomb scattering by the field of nuclei, nuclear elastic scattering, inelastic nuclear scattering, and Lindhard energy partition.[31] The displacement damage factor can be quantified using non-ionizing

energy loss (NIEL) which measures the energy lost due to non-ionizing events per unit length. Most of the proton effects in the materials are dominated by energy loss due to ionization. Fast traveling protons lose energy through inelastic collisions with bound electrons in the atoms and molecules of the stopping material and result in their ionization and excitation. The amount of energy loss (*dE/dx*) is directly related to the ionizing dose (D) delivered by the following relation[32]:

$$D = 1.6 \times 10^{-8} \frac{Rads\,.\,g}{MeV} . \frac{dE}{dx} . \Phi \qquad (4.2)$$

where Φ is called the fluence and is measured in units of particles/cm^2.

The Sun is an effective particle accelerator which is the main source of protons and other energetic particle radiations in the space. Among many other energetic particles ejected during solar activity, protons are the major ones. The solar atmosphere is associated with solar flares, coronal and interplanetary shocks created by the interaction of coronal mass ejections with the solar wind. The coronal mass ejection may generate an interplanetary shock which propagates in the space, deforming the interplanetary magnetic field lines and draping them downstream of the shock. Energetic particles may escape from their acceleration sites and propagate along interplanetary magnetic field lines into the interplanetary space. The encounter of the solar wind with Earth's magnetosphere creates an aerodynamic shock wave forming a bow shape which extends over the polar regions of the Earth. Low energy protons (maximum of 100 keV) are reported upstream of this bow-shock.[33] Therefore, both high energy protons in the range of GeV and low energy protons in the range of keV exist in the space radiation environment.[34]

In this dissertation work, we studied the effects of low energy (100 keV) protons on AlGaN/GaN HEMTs. Due to the nature of the mixed ionic and covalent bond, GaN and its alloys possess high threshold displacement energy than many of the other semiconductors used for power and optoelectronics.[35] Therefore, GaN is most viable semiconductor to be used as a radiation hard

electronics in the harsh radiation environments. For the experimental design, first of all, Stopping and Range of Ions in Matter (SRIM)[36] simulation was performed to estimate the penetration depth, proton dose distribution and total vacancy concentration in the HEMTs. The HEMT samples were irradiated by exposing to a beam of 100 keV protons with the fluences of 1×10^{10}, 1×10^{12} and 1×10^{14} protons/cm^2. Two mounting plates were prepared, holding the various-sized samples using carbon tape. For the irradiation purpose, the first plate was exposed to 100 keV protons produced by the NEC Pelletron 5SDH-2 Tandem Pelletron accelerator running at a terminal potential of .035 MV. The beam was transported to a raster scanner upstream from the sample chamber for uniformity of dose. A beam intensity of 4 nA scanned over an area of 20.32 cm^2 took 8.2 seconds to produce a fluence of 1×10^{10} protons/cm^2. The second plate, using the same mounting and beam energy and scanning parameters, was exposed to a beam intensity of 80 nA took 40.6 seconds to produce a fluence of 1×10^{12} protons/cm^2. The third set of samples were mounted on the same plate as set #1 and, using the same beam energy and scanning parameters, was exposed to an intensity of 60 nA for 541.9 seconds to produce a fluence of 1×10^{14} protons/cm^2.

From SRIM simulation, a total number of vacancies (cm^{-3}) for each fluence was estimated to be in the order of 10^{15}, 10^{17} and 10^{19} respectively for 1×10^{10}, 1×10^{12} and 1×10^{14} protons/cm^2 of 100 keV protons. Figure 4.4 shows the plot of defect densities in GaN layer obtained from SRIM. The detailed experimental procedure, results, and analysis are explained in chapter seven.

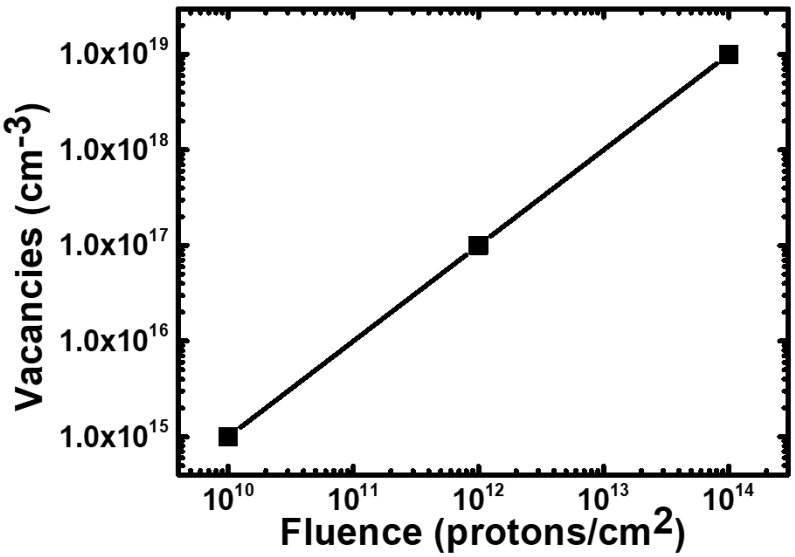

Fig. 4.4. Vacancies on HEMT GaN channel layer estimated from SRIM simulation.

References

[1] Barth, Janet L., C. S. Dyer, and E. G. Stassinopoulos. "Space, atmospheric, and terrestrial radiation environments." *IEEE Transactions on Nuclear Science* 50, no. 3 (2003): 466-482.

[2] Van Allen, James A. "The geomagnetically trapped corpuscular radiation." *Journal of Geophysical Research* 64, no. 11 (1959): 1683-1689.

[3] M. Moll *et al.*, "Development of radiation tolerant semiconductor detectors for the Super-LHC," *Nucl. Instrum. Methods Phys. Res. Sect. Accel. Spectrometers Detect. Assoc. Equip.*, vol. 546, no. 1–2, pp. 99–107, Jul. 2005.

[4] Johnston, A. H. "Radiation effects in advanced microelectronics technologies." *IEEE transactions on Nuclear Science* 45, no. 3 (1998): 1339-1354.

[5] O. Zeynali, D. Masti, and S. Gandomkar, "Shielding protection of electronic circuits against radiation effects of space high energy particles," p. 6, 2012.

[6] C. Claeys and E. Simoen, *Radiation Effects in Advanced Semiconductor Materials and Devices*. Springer Science & Business Media, 2013.

[7] Johnston, Allan. *Reliability and radiation effects in compound semiconductors*. World Scientific, 2010.

[8] Raymond, J. P., and E. L. Petersen. "Comparison of neutron, proton and gamma ray effects in semiconductor devices." *IEEE Transactions on Nuclear Science* 34, no. 6 (1987): 1621-1628.

[9] T. R. Oldham and F. B. McLean, "Total ionizing dose effects in MOS oxides and devices," *IEEE Trans. Nucl. Sci.*, vol. 50, no. 3, pp. 483–499, Jun. 2003.

[10] S. Buchner, D. McMorrow, J. Melinger, and A. B. Camdbell, "Laboratory tests for single-event effects," *IEEE Trans. Nucl. Sci.*, vol. 43, no. 2, pp. 678–686, Apr. 1996.

[11] Reed, R. A., M. A. Carts, P. W. Marshall, C. J. Marshall, O. Musseau, P. J. McNulty, D. R. Roth, S. Buchner, J. Melinger, and T. Corbiere. "Heavy ion and proton-induced single event multiple upset." *IEEE Transactions on Nuclear Science* 44, no. 6 (1997): 2224-2229.

[12] Schwank, J. R., M. R. Shaneyfelt, J. Baggio, P. E. Dodd, J. A. Felix, V. Ferlet-Cavrois, P. Paillet et al. "Effects of particle energy on proton-induced single-event latchup." *IEEE transactions on nuclear science* 52, no. 6 (2005): 2622-2629.

[13] T. R. Weatherfold *et al.*, "Proton and heavy ion upsets in GaAs MESFET devices," *IEEE Trans. Nucl. Sci.*, vol. 38, no. 6, pp. 1460–1466, Dec. 1991.

[14] C. L. Howe *et al.*, "Role of heavy-ion nuclear reactions in determining on-orbit single event error rates," *IEEE Trans. Nucl. Sci.*, vol. 52, no. 6, pp. 2182–2188, Dec. 2005.

[15] Summers, Geoffrey P., Edward A. Burke, and Michael A. Xapsos. "Displacement damage analogs to ionizing radiation effects." *Radiation Measurements* 24, no. 1 (1995): 1-8.

[16] G. C. Messenger, "A summary review of displacement damage from high energy radiation in silicon semiconductors and semiconductor devices," *IEEE Trans. Nucl. Sci.*, vol. 39, no. 3, pp. 468–473, Jun. 1992.

[17] J. R. Srour and J. W. Palko, "Displacement Damage Effects in Irradiated Semiconductor Devices," *IEEE Trans. Nucl. Sci.*, vol. 60, no. 3, pp. 1740–1766, Jun. 2013.

[18] Pearton, S. J., F. Ren, Erin Patrick, M. E. Law, and Alexander Y. Polyakov. "Ionizing radiation damage effects on GaN devices." *ECS Journal of solid state science and technology* 5, no. 2 (2016): Q35-Q60.

[19] X.-M. Bai, A. F. Voter, R. G. Hoagland, M. Nastasi, and B. P. Uberuaga, "Efficient Annealing of Radiation Damage Near Grain Boundaries via Interstitial Emission," *Science*, vol. 327, no. 5973, pp. 1631–1634, Mar. 2010.

[20] W. Wesch, A. Kamarou, and E. Wendler, "Effect of high electronic energy deposition in semiconductors," *Nucl. Instrum. Methods Phys. Res. Sect. B Beam Interact. Mater. At.*, vol. 225, no. 1, pp. 111–128, Aug. 2004.

[21] Wrobel, F. "Fundamentals on radiation-matter interaction." *New Challenges for Radiation Tolerance Assessment, RADECS* (2005): 19-23.

[22] S. M. Goodnick, "Radiation Physics and Reliability Issues in III-V Compound Semiconductor Nanoscale Heterostructure Devices," OREGON STATE UNIV CORVALLIS DEPT OF ELECTRICAL AND COMPUTER ENGINEERING, Nov. 1999.

[23] Emtsev, V. V., V. Yu Davydov, V. V. Kozlovskii, V. V. Lundin, D. S. Poloskin, A. N. Smirnov, N. M. Shmidt et al. "Point defects in-irradiated n-GaN." *Semiconductor science and technology* 15, no. 1 (2000): 73.

[24] Fishman, Gerald J., P. N. Bhat, R. Mallozzi, J. M. Horack, T. Koshut, C. Kouveliotou, G. N. Pendleton et al. "Discovery of intense gamma-ray flashes of atmospheric origin." *Science* 264, no. 5163 (1994): 1313-1316.

[25] Attix, Frank H., and Eugene Tochilin, eds. *Sources, Fields, Measurements, and Applications: Radiation Dosimetry*. Vol. 3. Academic Press, 2016.

[26] Kelly, Brian Thomas. *Irradiation damage to solids*. Oxford: Pergamon Press, 1966.

[27] Krtschil, A., A. Dadgar, and A. Krost. "Decoration effects as origin of dislocation-related charges in gallium nitride layers investigated by scanning surface potential microscopy." *Applied physics letters* 82, no. 14 (2003): 2263-2265.

[28] Q. Zhou, M. O. Manasreh, M. Pophristic, S. Guo, and I. T. Ferguson, “Observation of nitrogen vacancy in proton-irradiated AlxGa1−xN,” *Appl. Phys. Lett.*, vol. 79, no. 18, pp. 2901–2903, Oct. 2001.

[29] J. G. Kelly, T. F. Luera, L. D. Posey, D. W. Vehar, D. B. Brown, and C. M. Dozier, “Dose Enhancement Effects in MOSFET IC’s Exposed in Typical 60Co Facilities,” *IEEE Trans. Nucl. Sci.*, vol. 30, no. 6, pp. 4388–4393, Dec. 1983.

[30] K. G. Kerris and S. G. Gorbics, “Experimental Determination of the Low-Energy Spectral Component of Cobalt-60 Sources,” *IEEE Trans. Nucl. Sci.*, vol. 32, no. 6, pp. 4355–4362, Dec. 1985.

[31] E. A. Burke, “Energy Dependence of Proton-Induced Displacement Damage in Silicon,” *IEEE Trans. Nucl. Sci.*, vol. 33, no. 6, pp. 1276–1281, Dec. 1986.

[32] J. F. Janni, “Energy loss, range, path length, time-of-flight, straggling, multiple scattering, and nuclear interaction probability: In two parts. Part 1. For 63 compounds Part 2. For elements $1 \leqslant Z \leqslant 92$,” *At. Data Nucl. Data Tables*, vol. 27, no. 2, pp. 147–339, Mar. 1982.

[33] T. Terasawa, “Origin of $30 \sim 100$ kev protons observed in the upstream region of the Earth’s bow shock,” *Planet. Space Sci.*, vol. 27, no. 4, pp. 365–384, Apr. 1979.

[34] Barth, Janet L., Kenneth A. LaBel, and Christian Poivey. "Radiation assurance for the space environment." In *2004 International Conference on Integrated Circuit Design and Technology (IEEE Cat. No. 04EX866)*, pp. 323-333. IEEE, 2004.

[35] Ionascut-Nedelcescu, A., C. Carlone, A. Houdayer, H. J. Von Bardeleben, J-L. Cantin, and S. Raymond. "Radiation hardness of gallium nitride." *IEEE Transactions on Nuclear Science* 49, no. 6 (2002): 2733-2738.

[36] J. F. Ziegler, M. D. Ziegler, and J. P. Biersack, “SRIM – The stopping and range of ions in matter (2010),” *Nucl. Instrum. Methods Phys. Res. Sect. B Beam Interact. Mater. At.*, vol. 268, no. 11–12, pp. 1818–1823, Jun. 2010.

Chapter 5

Material Characterization Techniques

5.1 Introduction

In this chapter, different material characterization techniques employed for the characterization of AlGaN/GaN heterostructures and their principles are discussed. Before device fabrication, irradiated and pristine epi-layers were characterized using atomic force microscopy (AFM), scanning electron microscopy (SEM), x-ray diffraction (XRD), x-ray photoelectron spectroscopy (XPS), micro-Raman spectroscopy, and micro-photoluminescence (PL) spectroscopy.

5.2 Atomic Force Microscopy (AFM)

Atomic force microscopy (AFM) is a technique which allows for high-resolution imaging of surfaces with atomic layer depth resolution and lateral resolution in nanometer scale. Hence, topographical information about the sample surface can be obtained. AFM gives information on surface roughness, friction, thickness, conductivity, capacitance, dislocations, and homogeneity of the scanned surface. The base of the AFM is a sharp tip fixed on the cantilever which scans over the surface of the sample. The laser beam focused on the back side of the cantilever is reflected the surface of the position sensitive photodiode. When the cantilever scans over the sample surface, a small deflection of the cantilever will tilt the reflected beam and change the position of the beam on the photodiode.[1]

The magnitude of the force between the tip and the sample surface is minimal. The tip is maintained at a constant force (or height) above the surface due to the piezoelectric scanners enabled feedback mechanism. Based on the interaction of the tip and the sample surface, AFMs are categorized as contact mode (repulsive) and non-contact mode (attractive), or tapping mode.[2] For the work in this research, the non-contact mode scan was performed.

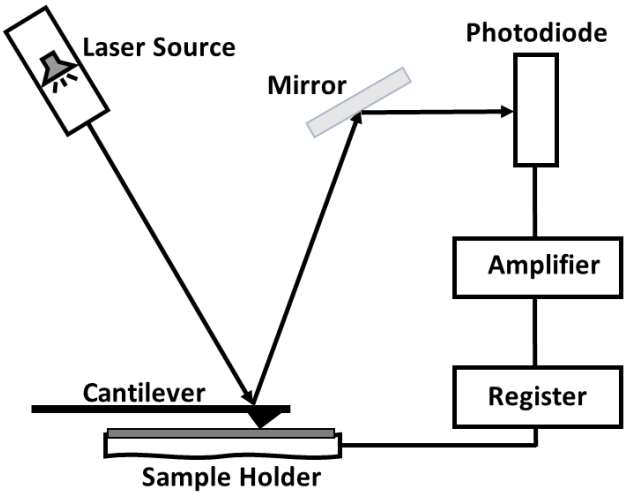

Fig. 5.1. Schematics of atomic force microscopy (AFM).

Contact mode scan provides the high resolution than the non-contact mode but the electrostatic and tension surface forces pull the scanning tip toward the surface, and that can damage the sample and distort the image data. Tapping mode is used for scanning very soft and fragile samples without inducing destructive forces but still reaching high-resolution images. Using Park Systems' XE7 AFM, we scanned over 10 × 10 μm^2 area to measure the root-mean-square (*rms*) surface roughness (R_q) of the HEMT samples, and the results are presented in chapter seven.

5.3 Scanning Electron Microscopy (SEM)

In scanning electron microscopy (SEM), a focused beam of electrons interacts with the atoms of the specimen by elastic and inelastic scattering, and secondary electrons are ejected. The reflected beam is sent to the detector, and the detected signals are used to image the morphology with resolution much higher than the optical methods, less than 5 nm.[3] SEM uses the methods based on the injection of charge carriers by the electron beam to measure the properties of semiconductors such as carrier lifetime or diffusion length or to study the surface topography by imaging methods. If incident electron beam undergoes elastic scattering, it continues its path after the interaction without losing kinetic energy (or energy loss is insignificant). When inelastic scattering

occurs, the incident electron loses part of its kinetic energy and it can activate other electrons or can excite atoms of the specimen. Figure 5.2 illustrates the interaction of the incident electron beam with the specimen. In this research, we aimed to observe the differences in surface morphology of the irradiated and pristine HEMTs. The obtained images and the analysis of the results are presented in chapter seven.

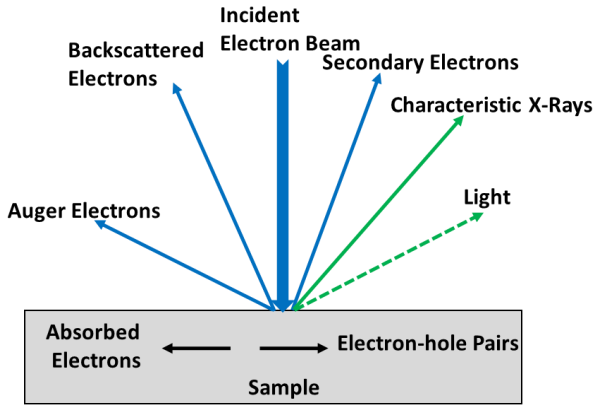

Fig. 5.2. Schematics of electron beam interaction with the specimen.

5.4 X-ray Diffraction (XRD)

X-ray diffraction (XRD) is one of the most commonly used methods for obtaining the crystal information such as thickness, alloy composition, dislocation density, and strain state of different layers in a crystal structure. The atomic planes of a crystal cause scattering of an incident beam of x-rays to constructively interfere with one another as they leave the crystal at angle θ, this phenomenon is called x-ray diffraction. Diffraction only occurs when Bragg's law (equation 5.1) is satisfied for constructive interference from crystal planes with spacing d.[4]

$$2d\ sin\theta = n\lambda \tag{5.1}$$

where d is the interplanar spacing, θ is the Bragg's angle, λ is the wavelength of the x-ray, and n is the fringe order in the interference pattern.

X-rays are produced whenever high-speed electrons ejected from a hot filament are accelerated and collide with a metal target. Bombarding electrons knock out the electrons from K-shell

(n = 1), which are filled by electrons in higher shells. Electrons falling from L-shell (n = 2) give rise to K_α lines, whereas electrons falling from M-shell (n = 3) give rise to K_β lines and so on. The intensity of K_α lines is usually higher and also have the shorter wavelength than L and M lines therefore it is less likely to be absorbed and most suitable for x-ray diffraction, K_α has doublets $K_{\alpha 1}$ and $K_{\alpha 2}$. A filter is used to get the monochromatic convergent K_α x-ray beam. Mostly used metal targets are copper (Cu), Aluminum (Al), Molybdenum (Mo) and Magnesium (Mg).[5]

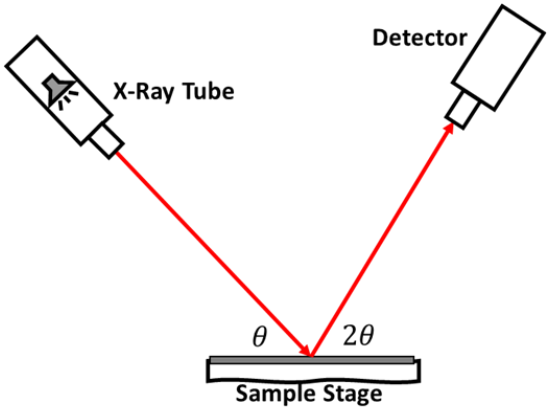

Fig. 5.3. Schematic diagram of a simple XRD system setup.

By sweeping the x-ray incidence and detection angles and identifying intensity peaks representing the constructive interference using fitting software, the lattice constant can be calculated for all the layers within the penetration depth. For cubic structures, the distance between the planes d is given by:

$$d = \frac{a}{\sqrt{h^2 + k^2 + l^2}} \tag{5.2}$$

where a is the length of the unit cell, h, k l, are the Miller indices. For hexagonal structures, it is given by:

$$d = \sqrt{\frac{1}{\frac{4}{3}\frac{h^2 + hk + k^2}{a^2} + \frac{l^2}{c^2}}} \tag{5.3}$$

where a and c are the length of axes of the unit cell.

We used Proto-AXRD $\theta - \theta$ diffractometer with an x-ray $K\alpha$ line from the Cu target with 40 kV at 30 mA to probe the AlGaN/GaN HEMTs from a symmetrical lattice plane (0002). Experimental results are presented in chapter seven.

5.5 X-ray Photoelectron Spectroscopy (XPS)

According to Einstein's theory of photoelectric effect, when light is an incident on a sample, an electron can absorb a photon and escape from the material with maximum kinetic energy given by:

$$K.E. = h\nu - E_B - e\phi \tag{5.4}$$

where ν is the frequency of the incident photon, h is Planck's constant, E_B is the binding energy of electron and ϕ is the work function of the material.

When x-rays (short wavelength/high energy photons) are incident on the crystal surface, the core electrons are knocked out of the atoms as shown in the illustrative Fig. 5.4. As the specimen is irradiated by x-ray of energy hν, electrons are emitted from inner atomic energy levels which were bound to the atomic nuclei with the binding energy E_B. Spectrum is obtained by measuring the characteristics of electrons that escape from the surface, and this spectroscopic method is called x-ray photoelectron spectroscopy (XPS). Analysis of binding energy and intensity of a photon peak also provides the information about the elemental identity, chemical state, information about the chemical bonds, and quantity of detected element. The average probing depth for an XPS measurement is approximately 5-10 nm.[6]

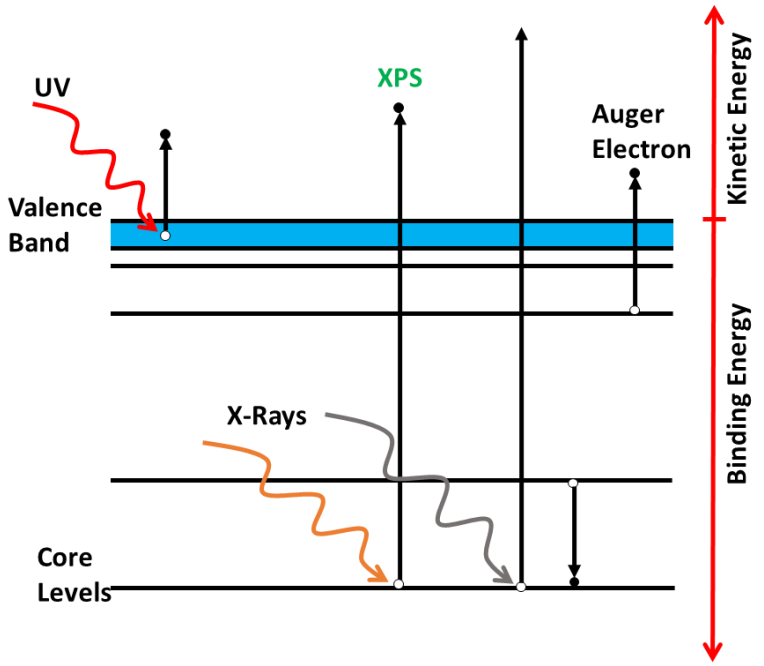

Fig. 5.4. Photoelectron emission due to an incident photon interaction with the specimen.

For this dissertation work, we used a load-locked Kratos XSAM 800 surface analysis system equipped with a hemispherical energy analyzer. A water-cooled, non-monochromatic dual anode x-ray gun equipped with Al window was used to excite the photoelectrons. MgKα of energy 1253.6 eV was used as radiation. The results and analysis of the XPS spectra obtained from pristine and proton irradiated HEMT samples are presented in chapter seven.

5.6 Raman Spectroscopy

Raman scattering is one of the main spectroscopic technique employed to detect vibrations in molecules. It is widely used to provide information on chemical structures and physical forms to identify from the characteristic spectral patterns. Although Raman scattering has the history dated back[7] to 1920s, the useful analytical role of the technique has been only utilized since the development of lasers.

When light interacts with matter, photons may be absorbed or scattered, or sometimes passes through it. When the light gets scattered, the vast majority of scattered photons are elastically scattered which is referred to as Rayleigh scattering, *i.e.* there is no shift in energy compared to the incident photon. Another scattering process is inelastic scattering which involves an exchange of energy with the matter which includes: Raman scattering and photoluminescence (OR fluorescence). The first order phonon Raman scattering takes place at the Γ point of the reciprocal lattice. The illustrative diagram of all these scattering is in Fig. 5.5. As it is seen in the figure, in the case of Rayleigh scattering, the incident and scattered photon have the same energy. In Raman scattering, the incident photon interacts with the molecule and distorts (polarizes) the cloud of electrons around the nuclei to form a short-lived state called a virtual state, which then decays leaving a change in vibrational energy. Two types of Raman scattering events are possible: Stokes and anti-Stokes scattering. In Stokes scattering, the crystal lattice absorbs the energy resulting in the emission of photons of lower energy than the incident light. In anti-Stokes, the crystal lattice loses phonon energy due to the excitation of the lattice by incident light, and higher energy photons are emitted. The energy differences associated with the changes in the frequency of the scattered light are directly attributed to the vibrational and rotational energy levels in the crystal which are called the phonon modes. Stokes and anti-Stokes peaks occur symmetrically about the laser line (frequency shifted up and down). The energy changes that we detect in vibrational spectroscopy are those required to cause nuclear motion.[8]

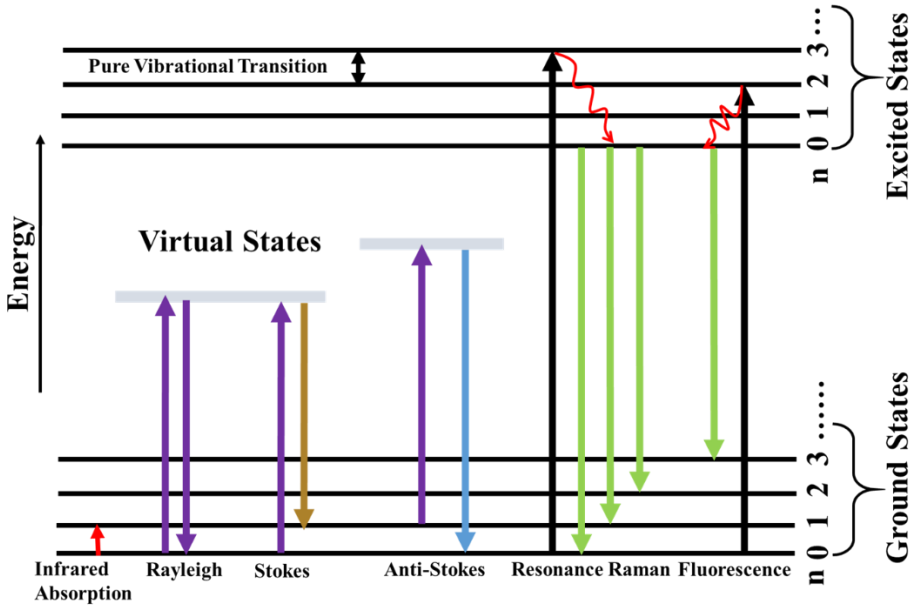

Fig. 5.5. Light-matter interaction and scattering process illustrative diagram.

Wurtzite crystal structures belong to the C_{6v}^4 space group containing the elements representing the translation reflection and rotation operations. According to group theory, 12 normal phonon modes (irreducible representation) exist at the Γ-point of the Brillouin zone. Among those, $A_1(z) + E_1(x, y) + 2B_1 + 2E_2$ are optical modes and the remaining modes are acoustic. The A_1 and E_1 modes are both Raman and infrared (IR) active, $2E_2$ modes belong to only Raman active phonons, whereas B_1 modes are silent modes. Due to the macroscopic electric field affiliated with the longitudinal modes, the polar $A_1$and E_1 modes split into transverse optical (*TO*) and longitudinal optical (*LO*) phonon modes with different frequencies.[9] In *TO* mode, dipoles do not add each other; rather they sum along the direction of propagation of *LO* mode.

The atomic displacements for A_1 and B_1 modes are along *c*-axis, and they are perpendicular to the *c*-axis for E_1 and E_2 modes. The displacement for B_1 and E_2 modes are a comparison of atoms, rather than a shear force which gives rise to the higher oscillation frequency. Therefore, both E_2 and B_1 modes are categorized as low and high. As mentioned earlier, B_1 are silent modes.

For wurtzite structures, the Raman tensor possesses only diagonal components for A_1 mode because this can be observed when the incident light and scattered light have a parallel polarization, in the case of E_1 mode it is observed only in cross polarization geometry. However, in the case of E_2 mode, both the diagonal and off-diagonal components are observed in Raman tensor.[10] In Raman spectroscopy, based on the directions of polarization and propagation of incident and scattered photons with respect to the suitable frame of reference, *i.e.* crystal axes, there is a convention to describe these directions which were proposed by Porto and called as Porto notation.[11] The general geometry of an experiment is described as *i(jk)l* where *j* and *k* are the polarization directions of the incident and scattered light respectively, and *i* and *l* are the propagation direction of the incident and scattered lights respectively. For a backscattered geometry, similar to the one we used in our experiment, *i* and *l* are antiparallel. For a linearly polarized laser *j* can be assigned to the x-direction. For the *k* values, if an analyzer is fitted to the spectrometer and is parallel to the incident light, assigned to *x*, but if perpendicular it is assigned in the *y*-direction. When there is no analyzer is used, then spectrometer is sensitive to all incoming polarizations, so *k* may be denoted by a dash (-). Theoretically permitted modes according to the different polarizations and scattered directions for a wurtzite structure of nitrides are tabulated in Table 5.1 below.[12]

Table 5.1: Theoretically allowed Raman modes in hexagonal nitrides.

Configuration	Allowed Mode
$x\ (y,y)\bar{x}$	$A_1(TO), E_2$
$x\ (z,z)\bar{x}$	$A_1(TO)$
$x\ (z,y)\bar{x}$	$E_1(TO)$
$x\ (y,z)y$	$E_1(TO), E_1(LO)$
$x\ (y,y)z$	E_2
$z\ (y,x)\bar{z}$	E_2
$z\ (y,y)\bar{z}$	$A_1(LO), E_2$
$z\ (x,x)\bar{z}$	$A_1(LO), E_2$
$z\ (x,y)\bar{z}$	E_2

We employed micro-Raman scattering spectroscopy to examine the crystal quality and strain state of the pristine and irradiated samples for the work in this dissertation. Characteristic spectral patterns were analyzed to get the information on physical structure of crystals and to estimate the free carrier concentration in the bulk. The experiment was performed with $z\,(-,-)\bar{z}$ backscattering geometry, and $E_2^{High}$and $A_1(LO)$ modes for GaN along with the E_2^{High}mode for AlN was observed. The results and analysis of the experiment performed at room temperature are presented in chapter six and seven. The schematics of the experimental set up is shown in Fig. 5.6.

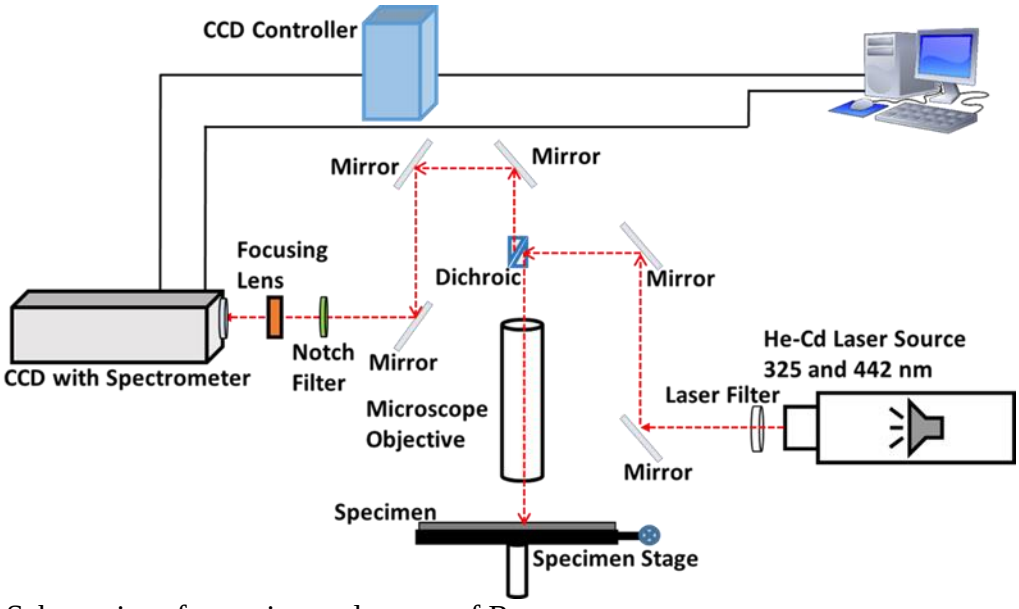

Fig. 5.6. Schematics of experimental set up of Raman spectroscopy system.

The Raman system is equipped with a dual wavelength (blue-442 nm and UV-325 nm) Kimmon He-Cd laser source (power 80 mW and 20 mW). The spectrum was collected by using a thermoelectrically cooled charge-coupled device (CCD) consisting of a spectrometer made by Jobin Yvon. The incident laser beam was focused into micron size diameter of 5-10 μm. Two sets of gratings available in the system has the following groove densities: 3600 lines/mm and 2400 lines/mm.

5.6.1 Crystal Stress Information from Raman Spectroscopy

The shift in phonon frequency can be used to extract the stress in the crystal since the shift of the phonon frequencies depends on the chemical bonding and atomic structure. In III-nitrides, three types of stress are typically observed: biaxial stress in the *a*-plane, uniaxial stress, along the *c*-axis and hydrostatic stress. Uniaxial and biaxial stresses arise due to the thermal expansion mismatch between the hetero-epitaxial layers, deposited films, and the substrate, lattice mismatch, and the distortion. Native defects and incorporated impurities in the material can cause the lattice distortion and result in hydrostatic stress.[12] The space group symmetry of the structure is always preserved even under these deformations, only the position of the frequency of the phonon shifts. The in-plane ($\epsilon_{xx} = \epsilon_{yy}$) and the normal ($\epsilon_{zz}$) components of the strain tensor can be expressed in terms of the lattice constants *a* and *c* (a_0 and c_0 are the equilibrium values) as follows[13]:

$$\epsilon_{xx} = \epsilon_{yy} = (a - a_0)/a_0 \tag{5.5}$$

$$\epsilon_{zz} = (c - c_0)/c_0 \tag{5.6}$$

The stress which is defined as the force applied per unit area and according to Hooke's law, the components of stress tensor σ and the strain tensor ϵ are related as:

$$\sigma_{xx} = \sigma_{yy} = (C_{11} - C_{12})\epsilon_{xx} + C_{13}\epsilon_{zz} \tag{5.7}$$

$$\sigma_{zz} = 2C_{13}\epsilon_{xx} + C_{33}\epsilon_{zz} \tag{5.8}$$

where C_{ij} is are the independent stiffness constants of the corresponding wurtzite structure. The stress and strain tensors follow the symmetry to eliminate the effects of rotational torque.

The biaxial strain parallel to the *c* axis is characterized by vanishing the forces in this direction *i.e.* $\sigma_{zz} = 0$. Using this in Eq. 5.8, Eq. 5.7 can be re-written as;

$$\sigma_{xx} = \sigma_{yy} = \left[(C_{11} - C_{12})\epsilon_{xx} - \frac{2C_{13}^2}{C_{33}}\right]\epsilon_{xx} \tag{5.9}$$

The elastic constants of GaN are reported as $C_{11} = 390$ GPa, $C_{12} = 145$ GPa, $C_{13} = 106$ GPa, and $C_{33} = 398$ GPa.[14] The phonon frequency shift in Raman modes are associated with the stress and strain and can be estimated using the following relation:

$$\begin{aligned} \Delta\omega_\lambda &= 2a_\lambda \epsilon_{xx} + b_\lambda \epsilon_{zz} \\ &= 2\tilde{a}_\lambda \epsilon_{xx} + \tilde{b}_\lambda \epsilon_{zz} \end{aligned} \tag{5.10}$$

where *a*, *b* and $\tilde{a}$, $\tilde{b}$ are the deformation potentials for the given strain and stress respectively.

For the *LO* and *TO* modes of A_1 and E_1 Raman modes and E_2^{High}mode, the frequency shift in phonon increases as stress and strain in the wurtzite crystal increases. Whereas, E_2^{Low}mode follows the opposite trend. The relative shift in the frequency position of $A_1(LO)$ and E_2^{High}modes are used to derive the tensile or compressive stress of hexagonal GaN. Since E_2^{High}mode generally yields a strong signal compared to other modes; it is used to evaluate the biaxial stress in *c*-plane. An increase in the phonon frequency peak position compared to unstrained GaN indicates compressive stress, and the decrease indicates tensile stress. The information on the crystal quality can be extracted by analyzing the full width at half maximum (FWHM) of E_2^{High}peak. The estimated biaxial stress coefficients are presented in chapter seven.

5.6.2 Carrier Concentration from Raman Spectroscopy

LO phonon-plasmon (*LPP*) modes appear in heavily doped semiconductors because of the resonant coupling of polar phonons and plasmons. When the plasma frequency is close to the longitudinal optical (*LO*) phonon frequency, *LO* frequency interact strongly with a free carrier plasma *via* its longitudinal electric field. Therefore, the free carriers can quench the *LO* phonons in GaN. This effect can be exploited to probe the changes in the free carrier concentration.[15] The frequency dependent dielectric function $\epsilon(\omega)$ given by a sum of the contribution from phonons and plasmons can be expressed as:

$$\frac{\epsilon(\omega)}{\epsilon_\infty} = 1 - \frac{\omega_{LO}^2 - \omega_{TO}^2}{\omega^2 - \omega_{TO}^2} - \frac{\omega_P^2}{\omega^2} \tag{5.11}$$

where ω_{LO} and ω_{TO} are frequencies of *LO* and *TO* phonons, ϵ_∞ *i*s the high-frequency dielectric (optical), and ω_P is the frequency of the free carriers and is given in SI units as;

$$\omega_P^2 = \frac{ne^2}{\varepsilon_0 \varepsilon_\infty m^*} \tag{5.12}$$

where *n* is free carrier density, ε_0 is the permittivity of free space and m^* is the effective mass of a free carrier (electron).

The coupled *LO* modes can propagate for $\epsilon(\omega_{LPP}) = 0$, at this condition, equation 5.11 will have two roots which will define high- and low- frequency *LPP* branches, *i.e.* LPP_+ and LPP_- respectively separated by a gap equal to the *LO-TO* splitting. When the plasmon frequency is lower than the uncoupled *LO* phonon frequency, the LPP_+ mode behaves like a plasmon, while the LPP_- mode is phonon-like. The frequency of LPP_+ mode increases with the carrier concentration, and eventually at higher concentration, corresponds to that of the plasmon. Neglecting the damping $\epsilon(\omega_{LPP}) = 0$, the two roots of equation 5.11 are written as[16]:

$$\omega_{LPP}^{\pm} = 1/2 \left\{ \omega_{LO}^2 + \omega_P^2 \pm \sqrt{[(\omega_{LO}^2 + \omega_P^2)^2 - 4\omega_P^2 \omega_{TO}^2]} \right\} \tag{5.13}$$

Rearranging equation 5.12,

$$n = \frac{\varepsilon_0 \varepsilon_\infty m^* \omega_P^2}{e^2} \tag{5.14}$$

Setting $\epsilon(\omega = \omega_{LPP}) = 0$ in equation 5.11,

$$\omega_P^2 = \frac{\omega_{LPP}^2(\omega_{LPP}^2 - \omega_{LO}^2)}{(\omega_{LPP}^2 - \omega_{TO}^2)} \tag{5.15}$$

Combining 5.14 and 5.15 we finally obtain,

$$n\,(x,y) = \frac{\varepsilon_0\, \varepsilon_\infty m *}{e^2} \frac{\omega_{LPP}^2\,(x,y)[\omega_{LPP}^2(x,y) - \omega_{LO}^2]}{\omega_{LPP(x,y)}^2 - \omega_{TO}^2} \tag{5.16}$$

Thus, measuring ω_{LPP} as a function of position (x, y) can be utilized for carrier density mapping with the assumption of negligible spatial variation of ω_{LO}, ω_{TO}, ϵ_∞ and m^*. We used[17] $\epsilon_\infty = 5.35$, $m^* = 0.20$ and[18] $\omega_{TO} = 533$ for the estimation of free carrier concentration using the frequency position of the $A_1(LO)$ phonon mode that we detected in our experiment. The experimentally estimated parameters are reported in chapter seven.

5.7 Photoluminescence (PL) Spectroscopy

Photoluminescence (PL) is an optical process in which light is emitted from a material as a result of the absorption of incident light (photo-excitation). In semiconductors, above bandgap excitation is required because PL relies on the electronic transition within the sample, hence sufficient photon energy ($E > Eg$) is required to excite the electrons into the conduction band.

When the incident photon of with $E > Eg$ gets absorbed, it causes the creation of an electron-hole pair through the promotion of an electron into the conduction band. From this state, the excited electron (hole) begins to relax to de-excite to the lower (higher) energy states in the conduction (valence) band through a process called thermalization, in which excess energy is transferred to the lattice in the form of phonons. Finally, electron-hole pair recombine resulting in the release of a photon with energy approximately equal to the energy separation of the band gap of the material. From this process, we can extract a great deal of information regarding the band structure, insight into material quality, and electronic states of the material. Since the PL is a radiative transisiton technique, a radiative recombination can occur at defect sites in the crystal as well which will reveal the details concerning defect composition and concentration.

Three types of luminescence occur in semiconductors: intrinsic, extrinsic and excitonic. In a direct bandgap semiconductor, for example, GaN, since there is no change in momentum between valence band maximum and conduction band minimum, radiative recombination occurs at

the photon energy equal or greater than bandgap energy. This process is known as intrinsic luminescence. In this case, the electron-hole pair generation rate is the same. On the other hand, for indirect bandgap semiconductors, predominantly phonons are generated so there is less likely to be the radiative recombination unless a highly localized center assists the phonons. This process is known as extrinsic luminescence. The third one which is excitonic luminescence occurs mainly indirect bandgap semiconductors with a high density of defects. An exciton is an electron-hole pair bound by electrostatic interaction and this forms when an electron excites from the valence band to conduction band leaving a hole in the valence band. The electron in the conduction band has large repulsive force from the surrounding electrons; it is attracted to the hole in the valence band by Coulomb force forming a pair. Excitons are mobile and have a short span of life at room temperature because of low binding energy, they ionize (decompose) into a free electron and a free hole. They do not recombine because possibly they cannot have the same wave vector. So, they need a third partner, and they can easily get trapped in lattice defects and then recombine emitting light which is referred to as excitonic luminescence.

For the research in this dissertation, we used PL spectroscopy to examine the crystal quality and study the defects introduced on AlGaN/GaN HEMTs due to high dose gamma-ray and low energy proton irradiation. Room temperature micro-PL was carried out by using a 325 nm line (20 mW) of He-Cd laser as an excitation source. For undoped wurtzite GaN, a typical PL spectrum exhibits three main bands namely yellow luminescence (YL), a shallow donor-shallow acceptor band (SD-SA) with the main peak which is also called as near band edge emission (NBE) and the third one a blue luminescence band (BL).[19] For our samples, we observed only two main bands: an NBE band peaking at ~3.42 eV and BL band at ~2.95 eV and ~2.81 eV. The YL peak which

was absent in our samples is associated with the impurities indicating the purity of them. The detailed analysis of the observed results is presented in chapters six and seven.

References

[1] McClelland, Gary M., Ragnar Erlandsson, and Shirley Chiang. "Atomic force microscopy: General principles and a new implementation." In *Review of progress in quantitative nondestructive evaluation*, pp. 1307-1314. Springer, Boston, MA, 1987.

[2] Morita, Seizo, Franz J. Giessibl, Ernst Meyer, and Roland Wiesendanger, eds. *Noncontact atomic force microscopy*. Vol. 3. Springer, 2015.

[3] Holt, David Basil, and David C. Joy, eds. *SEM microcharacterization of semiconductors*. Vol. 12. Academic Press, 2013.

[4] Ramachandran, Vangipuram Seshachar, and James J. Beaudoin. *Handbook of analytical techniques in concrete science and technology: principles, techniques and applications*, pp. 275–332. Elsevier, 2000 NY: William Andrew Publishing, 2001.

[5] Smith, Joseph V. "X-ray diffraction techniques." In *Feldspar Minerals*, pp. 179-216. Springer, Berlin, Heidelberg, 1974.

[6] Van der Heide, Paul. *X-ray photoelectron spectroscopy: an introduction to principles and practices*. John Wiley & Sons, 2011.

[7] Lewandowska, R., and J. Liu. "Raman Microscopy: Analysis of Nanomaterials." (2010): 1-6.

[8] Smith, Ewen, and Geoffrey Dent. *Modern Raman spectroscopy: a practical approach*. Wiley, 2019.

[9] Irmer, Gert, Christian Röder, Cameliu Himcinschi, and Jens Kortus. "Raman tensor elements and Faust-Henry coefficients of wurtzite-type α-GaN: How to overcome the dilemma of the sign of Faust-Henry coefficients in α-GaN?" *Journal of Applied Physics* 116, no. 24 (2014): 245702.

[10] Loudon, Rodney. "The Raman effect in crystals." *Advances in Physics* 13, no. 52 (1964): 423-482.

[11] Porto, S. P. S., J. A. Giordmaine, and T. C. Damen. "Depolarization of Raman scattering in calcite." *Physical Review* 147, no. 2 (1966): 608.

[12] Harima, Hiroshi. "Properties of GaN and related compounds studied by means of Raman scattering." *Journal of Physics: Condensed Matter* 14, no. 38 (2002): R967.

[13] Wagner, J-M., and F. Bechstedt. "Phonon deformation potentials of α-GaN and-AlN: An ab initio calculation." *Applied Physics Letters* 77, no. 3 (2000): 346-348.

[14] Polian, A., M. Grimsditch, and I. Grzegory. "Elastic constants of gallium nitride." *Journal of Applied Physics* 79, no. 6 (1996): 3343-3344.

[15] Ponce, F. A., J. W. Steeds, C. D. Dyer, and G. D. Pitt. "Direct imaging of impurity-induced Raman scattering in GaN." *Applied physics letters* 69, no. 18 (1996): 2650-2652.

[16] Perlin, P., J. Camassel, W. Knap, T. Taliercio, J. C. Chervin, T. Suski, I. Grzegory, and S. Porowski. "Investigation of longitudinal-optical phonon-plasmon coupled modes in highly conducting bulk GaN." *Applied physics letters* 67, no. 17 (1995): 2524-2526.

[17] Shur, M. S., R. Gaska, and A. Bykhovski. "GaN-based electronic devices." *Solid-State Electronics* 43, no. 8 (1999): 1451-1458.

[18] Kozawa, T., T. Kachi, H. Kano, Y. Taga, M. Hashimoto, N. Koide, and K. Manabe. "Raman scattering from LO phonon-plasmon coupled modes in gallium nitride." *Journal of Applied Physics* 75, no. 2 (1994): 1098-1101.

[19] Reshchikov, M. A., and R. Y. Korotkov. "Analysis of the temperature and excitation intensity dependencies of photoluminescence in undoped GaN films." *Physical Review B* 64, no. 11 (2001): 115205.

Chapter 6

Gamma-ray Irradiation Effects on AlGaN/GaN HEMTs

This chapter is the following paper published in the Journal of Vacuum Science & Technology B **35**, 03D107 (2017):

Electrical and optical characteristics of gamma-ray irradiated AlGaN/GaN high electron mobility transistors

Min P. Khanal[1], Burcu Ozden[1], Kyunghyuk Kim[1], Sunil Uprety[1], Vahid Mirkhani[1], Kosala Yapabandara[1], Ayayi C. Ahyi[1] and Minseo Park[1*]

[1]Department of Physics, Auburn University, Auburn, AL 36849, USA

*Corresponding Author: park@physics.auburn.edu

A comparative study on the direct-current (dc) electrical performance and optical characteristics, of unirradiated and 120 MRad ^{60}Co-gamma-rays (γ-rays) irradiated AlGaN/GaN high electron mobility transistors (HEMTs) were performed. The devices fabricated on irradiated HEMT epi-layer structure show slight degradation/alteration in the dc characteristics such as source-drain current-voltage (I_{DS}-V_{DS}), transfer (I_{DS}-V_{GS}), transconductance and the gate current-voltage (I-V) indicating the presence of radiation-induced defects. Also, we observed a shift in flat-band voltage from the capacitance-voltage (C-V) measurement. Micro-Raman spectroscopy and photolumines-cence (PL) spectroscopy were used to compare the crystal quality of the heterojunction. No shift

in the Raman peak frequency position on both the unirradiated and irradiated samples was observed, which implies that the irradiation did not produce an additional strain to the HEMT layers. However, full width at half maximum (FWHM) of the Raman and near-band-edge PL peaks has increased after irradiation, which suggests the degradation of crystal quality. The spectroscopic photocurrent-voltage (*IV*) study with sub-bandgap and above bandgap illumination confirmed the pre-existence of sub-bandgap defects in the heterostructure and revealed the possibility of their re-arrangement or the introduction of new defects after the irradiation. It was concluded that AlGaN/GaN HEMTs is relatively resistant to high dose (120 MRad) gamma-ray irradiation, but it can introduce additional traps or re-configure the pre-existing traps, influencing the electrical and optical characteristics of AlGaN/GaN HEMTs.

I. INTRODUCTION

The adverse effect of radiation on the electronic instruments used in space communication systems, fusion plasma facilities, and nuclear systems have been a problem. Gallium Nitride (GaN) possess several inherent properties such as a strong ionic-covalent bond[1], large direct bandgap (3.47 eV)[2], excellent thermo-mechanical stability[3], ultrafast carrier relaxation time[4], high displacement energy[5], and higher breakdown field.[6] In addition, wide bandgap of GaN results in relatively low phonon loss and a high threshold for electron-hole pair generation upon ionizing radiation.[7] These properties make GaN a prominent candidate for the electronic applications under high-energy particle radiation, high temperature, and high voltage.[8]

Aluminum Gallium Nitride/Gallium Nitride (AlGaN/GaN) heterostructure holds unique interface driven properties, giving rise to high electron density at the junction.[9] A larger band discontinuity at the AlGaN/GaN interface creates a triangular potential well, and the polarization field (spontaneous and piezoelectric) leads to the formation of a two-dimensional electron gas (2DEG). This structure provides AlGaN/GaN HEMTs a distinct feature to alleviate some of the harmful effects of radiation damage.[10]

Considering the practical application of AlGaN/GaN HEMTs, they are exposed to different types of radiation fluxes ranging from high energy proton and electrons in low earth orbit satellites to neutrons or gamma-rays in nuclear and military systems. The effect of a proton, electron and neutron irradiation on the AlGaN/GaN HEMTs has been investigated by many researchers.[8,11,12,13,14,15] However, only a few reports on high-dose gamma-ray irradiation have been published. For the ^{60}Co- γ rays with 1.17 Mev and 1.33 MeV energies, Compton electrons with a mean energy of about 700 KeV can induce the defects in GaN, which is equivalent to internal electron irradiation.[16] Since all types of energetic particles interacting with matter generate

secondary gamma-photons in the material,[17] it is crucial to study and understand the mechanism of interaction of gamma-rays with the material.[18,19,20] Irradiation study provides the multifaceted opportunity to learn about the spectrum of defects generated in a controlled environment, leading to elucidate the nature of irradiation-induced defects. It is well known that high-dose irradiation on semiconductor device results in the production of vacancies in the lattice, defect clusters, and dislocations near the metal-semiconductor (MS) interface.[21] Koehler *et al.*[11] reported irradiation-induced damage in the form of voids at MS junction. The formation of voids at MS junction leads to the degradation of electrical performance. In addition, irradiation also causes damage to the structure and influences the defect density of the bulk material itself.[8]

In this report, we present the results of a comparative study of dc characteristics and optical properties of unirradiated and gamma-ray irradiated AlGaN/GaN HEMTs. Both the devices with unirradiated and gamma-ray irradiated HEMT layers were characterized by I_{DS}-V_{DS}, gate I-V, CV, spectroscopic photo-IV measurement, Raman and PL spectroscopy. The major purpose of this study is to investigate the influence of gamma-ray irradiation on the device performance and generation/reconfiguration of defects.

II. EXPERIMENTAL

The AlGaN/GaN epitaxial structures which were used for this investigation were acquired from a commercial vendor. The epitaxial structures were grown on the 6″ Si (111) wafers by metal-organic chemical vapor deposition (MOCVD). Initially, 250 nm thick AlN nucleation layer were grown on Si, followed by deposition of the multi-layered AlGaN buffer with varying aluminum (Al) concentration (between 20 and 75%). On top of this buffer layer, a 1 μm thick undoped GaN layer was grown, followed by deposition of a 20 nm AlGaN barrier layer. Finally, a 2 nm ultra-thin GaN cap layer was grown on top of the barrier layer.

The 6-inch HEMT epitaxial wafer was initially diced into 1×1 cm pieces, and those pieces were cut into two halves. The one-half piece was irradiated with ^{60}Co- γ rays to a dose of 120 MRad (Air) (~132 MRad (GaN)) at the rate of 38.83 R/S at room temperature and the other half was left unirradiated. Devices were fabricated after the one month of the irradiation using both, the unirradiated and the irradiated pieces. We were more interested in investigating the radiation damage produced in the bulk semiconductor epilayers rather than the damage produced on the metallic contact layer or at the MS junction. That is why we fabricated the devices after irradiating the epi-layer structure (with no contacts), rather than exposing the fully fabricated devices (with contacts). The pristine and the devices which were fabricated after irradiation of the epi-layer structures will be referred to as "unirradiated" and "irradiated" samples, respectively. Circular device configuration was used to avoid the mesa isolation. Source and drain contacts (Ti/Al/Ni with the thickness of 30/180/40 nm) were deposited *via* dc magnetron sputtering, followed by annealing at 850°C for 30 secs under the nitrogen atmosphere. As a gate contact, 15 nm thick Iridium (Ir) was sputter deposited. Various sized transistor devices were fabricated on the same, and one of the representative device characteristics with a gate aspect ratio (W/L) of 6.62 are presented here. For the purpose of spectroscopic photo-IV measurement, an array of circular semi-transparent (thickness 10-15 nm) Ni Schottky contacts with 600 μm in diameter was deposited on both the pieces.

Transistor current-voltage (I-V) characteristics were measured using Keithley 2400-source meters automated with a LabVIEW program. The room temperature micro-Raman spectroscopy was carried out in back-scattering geometry using 441.563 nm line (80 mW) from the He-Cd laser. The micro-PL measurements were performed at room temperature by exciting the samples with a 325 nm line (20 mW) from the He-Cd laser. Spectroscopic photo-IV measurements were

conducted with above bandgap (280-400 nm) and sub-bandgap (800-400 nm) illumination from a Xenon lamp light source coupled with a monochromator. A Keithley 6487 pico-ammeter with built-in voltage source was used to apply the bias and to collect the photocurrent. The direction of current flow was vertical and was controlled by applying a reverse bias to top Schottky contact with respect to the bottom ohmic contact.

III. RESULTS AND DISCUSSION

A. Raman Spectroscopy

Raman spectral analysis was performed to investigate the effect of gamma-ray irradiation on crystal quality and the strain of the samples. Raman scattering provides information on physical structures from the characteristic spectral patterns. GaN has a hexagonal wurtzite structure and belongs to the C_{6V}^4 space group. Therefore, group theory predicts $A_1(z) + E_1(x,y) + 2B_1 + 2E_2$ modes at the Γ point of the Brillouin zone. $A_1(z), E_1(x,y)\ and\ E_2$ modes belong to Raman active phonons and $A_1(z)\ and\ E_1(x,y)$ modes are also infrared active whereas B modes are silent.[22]

Figure 1 shows the room temperature Raman spectra obtained from the unirradiated and irradiated samples, which were collected using $z(-,-)\bar{z}$ backscattering geometry. We observed E_2^{high}peak around 569 cm^{-1} and $A_1(LO)$ peak around 733 cm^{-1} for both the unirradiated and irradiated samples. The peak positions that we observed are in agreement with the previously reported results.[23]

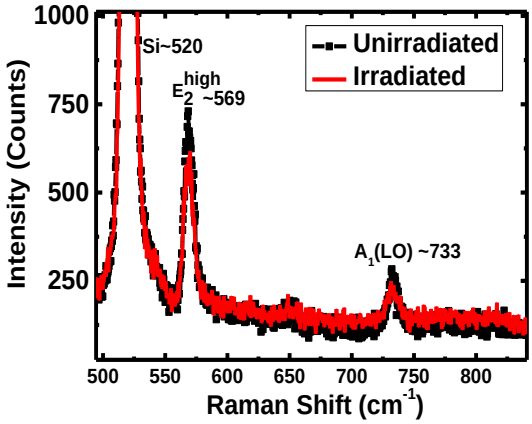

FIG. 1. (Color online) Raman spectra of unirradiated and irradiated samples.

The peak intensities for the irradiated sample were slightly reduced in comparison to the unirradiated samples. It can be seen that the frequency of E_2^{high} phonon mode did not change after the irradiation, which indicates that the strain of GaN layer in the heterostructure was not influenced by the gamma-ray irradiation. However, a slight broadening in the FWHM of this peak was observed after the irradiation in reference to the unirradiated one. The FWHM of E_2^{high} peak for the unirradiated and irradiated sample was respectively measured to be 9.0 cm^{-1} and 10.2 cm^{-1}. The broadening of FWHM of E_2^{high} implies that gamma-ray irradiation may result in degradation of the crystalline quality of the GaN layer in the heterojunction. Additionally, we did not observe any shift in the peak frequency position of the $A_1(LO)$ mode. However, the FWHM of $A_1(LO)$ peak was 9.0 cm^{-1} and 12.8 cm^{-1} for the unirradiated and the irradiated samples, respectively, which also broadened after the irradiation. Abderrahmane *et al.*[24] also reported the broadening of $A_1(LO)$ peak with no shift in its frequency position for the proton irradiated AlGaN/GaN heterostructures. The $A_1(LO)$ mode couples with plasmon and produce a coupled plasmon longitudinal optical (LO) phonon modes, and no substantial change in the peak position was observed, suggesting that the irradiation did not cause any change in the electron density in the bulk GaN layer itself.[15]

Moreover, the broadening of $A_1(LO)$ peak also suggests degradation of crystal quality. It is believed that the degradation of crystal structure occurs *via* the introduction of the additional defects and traps in the GaN crystal, which will eventually lead to a decrease in electron mobility.

B. Photoluminescence

PL spectroscopy was used to study the difference in optical properties of the unirradiated samples and the gamma-ray irradiated samples produced by the possible displacement of the atoms in the crystal lattice and distribution in structural defects by the incident radiation. The PL spectra can be used to examine the quality of the crystal and the defect concentration by studying the electronic transition of the defects between the states.[25] Figure 2(a) shows the full range (UV-visible) and 2(b) shows UV PL spectra of the unirradiated and the irradiated samples. The PL spectra exhibit an interference pattern which arises from the superposition of the light emitted from the contacts and reflected by different interfaces of the heterostructure.[26] Two main bands were observed in the PL spectra: the near-band-edge (NBE) emission with a pronounced peak at 3.42 eV and the blue luminescence (BL) band peaked at around 2.95 eV.

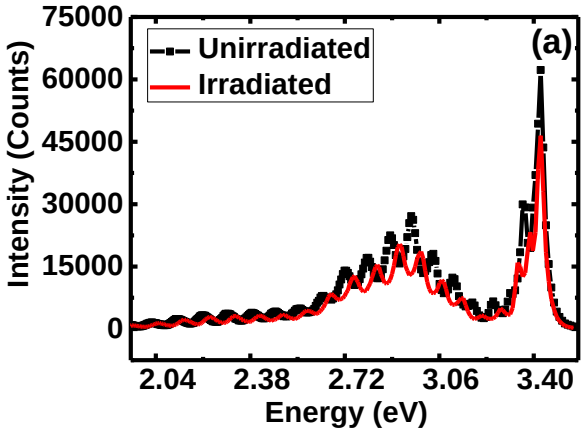

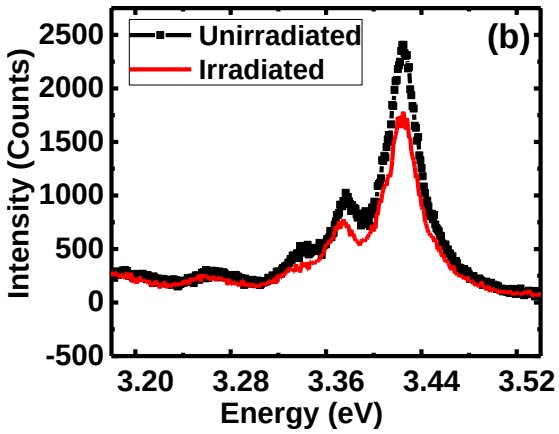

FIG. 2. (Color online) PL spectra of unirradiated and irradiated samples (a) UV-Visible scan (b) UV scan.

The NBE emission is attributed to the excitonic transition whereas the BL band peak is believed to be originated from the donor-acceptor (DA) recombination optical transition from a shallow donor to a deep acceptor.[27] In reference to the unirradiated sample, the decrease in the intensity and increase in the FWHM of all the PL peaks were observed for the irradiated sample. It is well known that both the intensity and the FWHM of PL spectra are related to the crystal quality of a sample. For two comparable samples with the same compositional structure, the broadening of FWHM and reduction in intensity of PL peaks implies that the crystal quality of one has degraded.[15] The widening of FWHM of NBE band is consistent with the broadening of FWHM of Raman E_2^{high} phonon mode. The increase in peak width of NBE was attributed to the increase in impurity and/or defect concentration.[25]

C. Electrical Characterization

Figures 3(a) and 3(b), respectively, show the I_{DS}-V_{DS} output characteristics of unirradiated and irradiated (with a dose of 120 MRad from ^{60}Co- γ ray source) samples. From Fig. 3, it can be seen that the drain saturation current was reduced by more than 50% for the irradiated samples in

comparison to the unirradiated ones. This reduction in the drain saturation current is in consistent with the earlier reports.[28,29]

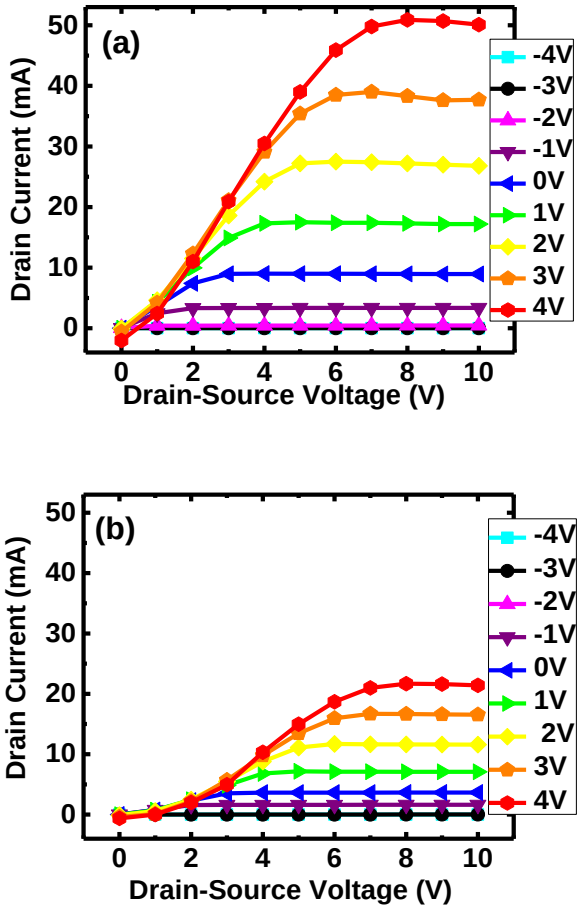

FIG. 3. (Color online) Source-drain current-voltage (I_{DS}-V_{DS}) characteristics of (a) unirradiated sample and (b) irradiated sample.

Figure 4(a) shows the transfer (I_{DS}-V_{GS}) characteristics for unirradiated and irradiated samples. As can be seen from the figure, the drain current (as a function of gate voltage) for the irradiated device is significantly lower than that for the unirradiated one. In addition, the positive threshold voltage shift was observed for the irradiated samples, which can be seen from the inset of Fig. 4(a) and also from Fig. 3. Figure 4(b) shows the comparison of transconductance between

unirradiated and irradiated samples, and the peak transconductance for the irradiated samples is observed to be lower than that for the unirradiated ones.

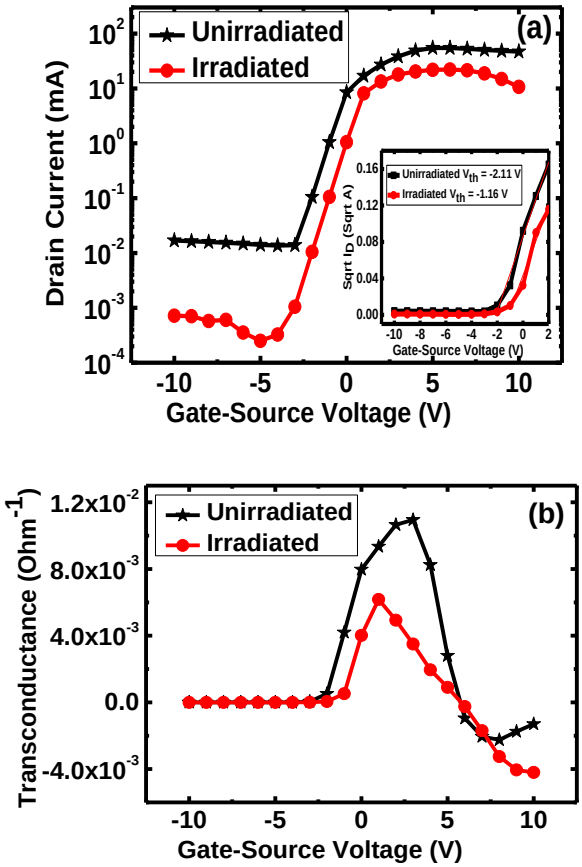

FIG. 4. (Color online) (a) Transfer (I_{DS}-V_{GS}) characteristics and (b) transconductance of unirradiated and irradiated samples. The inset of (a) shows the positive threshold shift on the irradiated sample (Sqrt I_D: square root of drain current).

The observed reduction in drain current and transconductance are thought to be attributed to the decrease in the carrier concentration and mobility in the HEMT channel.[12,18,29] There are variations in the published results about the direction of the threshold voltage shift caused by gamma-ray irradiation of the GaN devices; some researchers reported negative threshold voltage shift,[9,18,19] and others reported positive threshold voltage shift.[28,29,30] Our results are in agreement

with the reports which claim the positive shift in threshold voltage after gamma-ray exposure of the sample.

The positive threshold voltage shift can be attributed to a decrease in Schottky barrier height, mobility, and channel carrier density.[28,29,30] The Schottky barrier height reduction can be caused by the radiation-induced damage in MS interface, which is not applicable to our case since the contacts were prepared after irradiating epi-layer structures. The structural disorder caused by irradiation may introduce the traps which can cause a reduction in mobility.[28] In the present study, the 2DEG carrier density (n_s) in the channel was estimated using the following relation[12];

$$n_s = \frac{\varepsilon\,(V_{GS}-V_{TH})}{e\,t} \qquad (1)$$

where ε is the dielectric constant of AlGaN which is calculated using the model by Ambacher *et al.*,[31] V_{GS} is the gate to source voltage, V_{TH} is the threshold voltage, e is the electronic charge, and t is the thickness of the barrier layer.

The 2DEG carrier densities on the unirradiated and irradiated samples were estimated to be approximately 1.17×10^{13} cm^{-2} and 0.9×10^{13} cm^{-2}, respectively. The estimated 2DEG carrier density of the irradiated sample is 23% lower than that of the unirradiated sample, which is believed to be one of the reasons why the positive threshold voltage shift was observed for the irradiated sample.

The carrier mobility (μ) in the channel was calculated as follows[12];

$$\frac{V_{DS}}{I_{DS}} = R_S + R_D + \frac{L\,t}{W\,\mu\,\varepsilon\,(V_{GS}-V_{TH})} \qquad (2)$$

where V_{DS} and I_{DS} are the drain–source voltage and current, respectively, R_S and R_D are the source and drain access resistances, respectively, and W and L are the gate width and the length, respectively. The mobility is obtained from the reciprocal of the slope of the plot of $\frac{V_{DS}}{I_{DS}}$ *vs.* $\frac{1}{(V_{GS}-V_{TH})}$ in

Eq. (2). The field effect mobility of the carriers in the channel for the unirradiated and irradiated samples is approximately estimated as 2105 cm^2/Vs and 1276 cm^2/Vs, respectively.

As mentioned above, the degradation of the drain saturation current was more than 50%. The 23% reduction in carrier density is not comparable with the decrease in drain saturation current. So, one can conclude that the reduction in drain saturation current is not only produced by the reduction in carrier concentration but also by the reduction of mobility in the channel.[8]

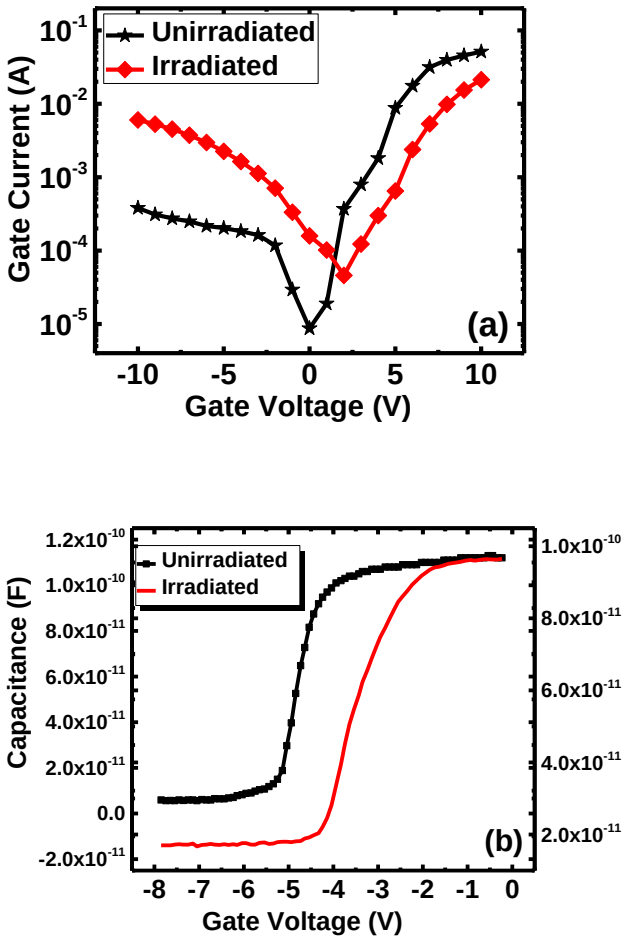

FIG. 5. (Color online) (a) Forward and reverse bias gate I-V characteristics (b) capacitance-voltage characteristics of unirradiated and irradiated samples.

Figure 5(a) illustrates the forward and reverse bias gate I-V characteristics. The forward gate leakage current slightly decreased after the irradiation while the reverse gate leakage current

increased. In addition, it can also be observed that the curve for the irradiated (the current minimum) sample is shifted towards the positive voltage. The high frequency (100 kHz) capacitance-voltage characteristics for unirradiated and irradiated samples are presented in Fig. 5(b), and it shows that both the threshold voltage and the flat-band voltage has been shifted toward the positive value. Although the gate leakage characteristics that we have observed is not commonly reported behavior for the gamma-ray irradiated HEMTs, Kim *et al*.[32] reported a similar trend for GaN devices. The positive shift on the current minimum value provides the indication of the irradiation-induced negative charge trapping.[13] The reduction in leakage current in forward bias regime may be caused by current transport mechanism such as space-charge generation, surface leakage, and deep level tunneling.[32] The most plausible reason for such behavior in our case is the reduction in free carrier concentration. Similarly, it can be speculated that the increased reverse leakage current for the irradiated device might be attributed to an increase in hopping and/or tunneling transport due to the increase in defect density upon gamma-ray irradiation.[14]

The positive threshold voltage shift observed from the capacitance-voltage measurement is in good agreement with the I_{DS}-V_{GS} measurement. Ionizing radiation may create the acceptor-like (negatively charged) traps, creating the negative space charge. Therefore, we conclude that this positive shift is caused by such traps introduced from gamma-ray irradiation.[8,33] The positive shift of flat-band voltage can also be explained by a decrease in carrier concentration caused by radiation-induced defect sites and/or damage in the AlGaN barrier layer causing the alternation in fixed charges.[34,35]

Post-irradiation annealing has been studied to observe the thermal effect on the irradiated GaN devices.[16,36,37,38,39] Some reports[36,37] claim the recovery of the irradiation-induced effects during the post-irradiation annealing, but there are several other reports [38,39] that claim the device

performance was not recovered even after the high-temperature post-irradiation annealing. Yadav *et al.*[38] reported the post-irradiation annealing device recovery of the gamma-ray exposed devices depends on the radiation dose and they also mentioned no post-irradiation annealing recovery for the 100 kRad gamma-ray exposed HEMTs. As we mentioned earlier, our samples were also annealed at 850°C during the ohmic contact metallization after relatively high dose (120 MRad) of gamma-ray irradiation. However, a reduction in the output current was observed for the irradiated samples in comparison to the unirradiated samples, which is in agreement with the earlier reports.[38,39]

D. Spectroscopic Photo-IV

Spectroscopic photo-IV measurement is a complementary technique to PL and was used to study the spectral and in-depth distribution of defects.[40]The purpose of this measurement is to detect the deep level-to-band electronic transition of charge carrier. The spectroscopic photo-IV technique is sensitive to both radiative and non-radiative transitions while the PL is sensitive to only radiative transition. The electronic transition will be induced as a consequence of photon absorption from the incident light. In the case of spectroscopic photo-IV measurement with sub-bandgap illumination, the traps with the different activation energy (from low to high deep level-to-band transition energy) were sequentially probed by changing the wavelength of light from long to short wavelength. In the case of spectroscopic photo-IV measurement with above-bandgap illumination, probing depth will gradually increase as the wavelength of the light increases.

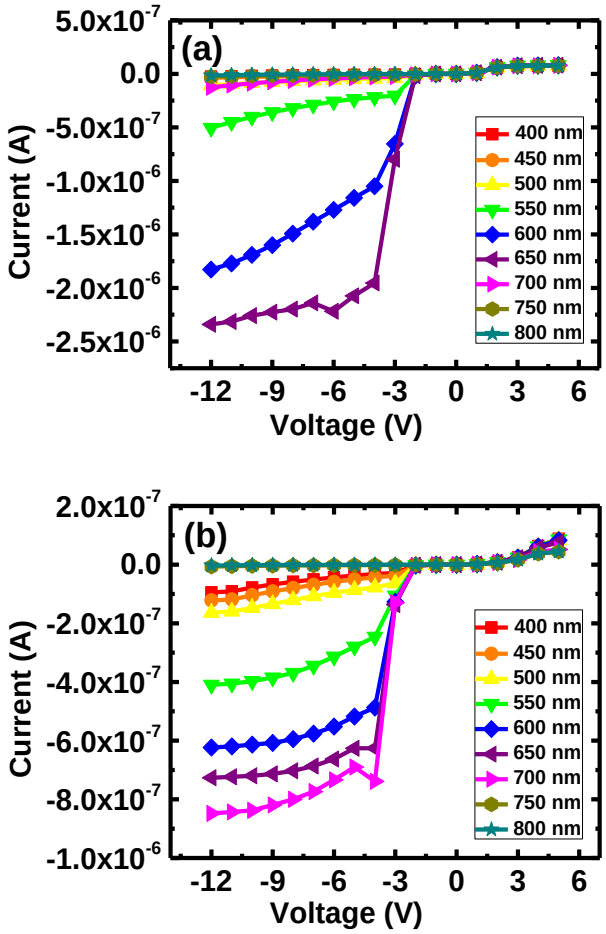

FIG. 6. (Color online) Sub-bandgap illumination spectra of (a) unirradiated sample (b) irradiated sample.

Figures 6(a) and 6(b) show the sub-bandgap spectroscopic photo-IV data for the unirradiated and irradiated samples, respectively. Figure 7 shows the normalized spectroscopic photo-IV spectra chosen at -10 V from Fig. 6 for the corresponding wavelengths and then normalized with the optical power. The wavelength of the light was varied from 800 nm to 400 nm with a step of 50 nm.

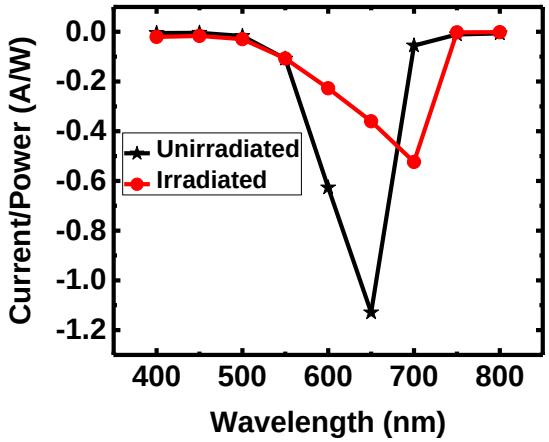

FIG. 7. (Color online) Normalized photo-current response for sub-bandgap illumination.

The sub-bandgap illumination provides the information about sub-bandgap energy levels of defects within the bandgap by relating the change in photocurrent level in response to the wavelength of the light. It is well known that persistent photoconductivity is prevalent in GaN and related materials.[41,42] Therefore, sequential photocurrent measurement will produce a systematic reduction in photocurrent. If there are no sub-gap defects, the photo-IV spectra will simply follow the pattern of gradual reduction of photocurrent as the measurement is repeated. However, as can be seen from Fig. 6(a), distinct photocurrent spectra were observed, which confirms the pre-existence of sub-bandgap defects in the unirradiated samples. The spectroscopic photo-IV measurement was also performed on the irradiated samples. As can be seen from Fig. 6(b) (and also in Fig. 7), strikingly different spectra with the reduction and shift in peak intensity position were collected for the irradiated sample, which possibly implies that the gamma-ray irradiation may induce the generation of new sub-gap states and/or spectral re-configuration of the existing defects.[8,9,39] The reduction in the intensity of the photo-IV spectra might be attributed to the quenching of persistent photoconductivity caused by irradiation-induced defects.[42]

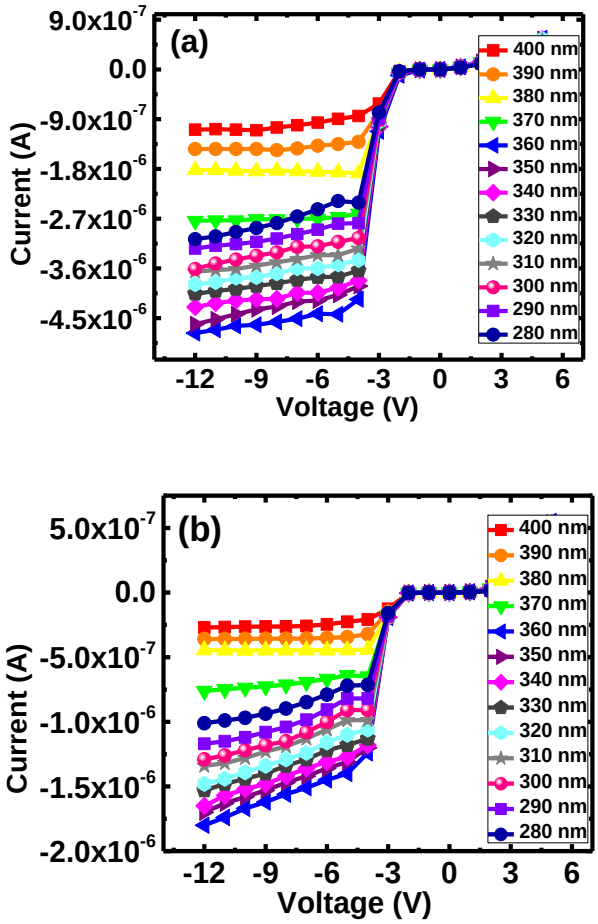

FIG. 8. (Color online) Above bandgap illumination spectra of (a) unirradiated sample (b) irradiated sample.

Figures 8(a) and 8(b), respectively show the above bandgap illumination photocurrent spectra of unirradiated and irradiated samples. During the measurement, the wavelength of the light was varied from 280 nm to 400 nm at the steps of 10 nm. The above bandgap illumination spectroscopy utilizes the fact that the penetration depth of the light varies as a function of the wavelength, as is presented by Beer-Lambert law;

$$\text{Penetration depth } (d) = 1/\alpha \tag{3}$$

where α is the absorption coefficient and can be calculated as follows;

$$\alpha = 4\pi K/\lambda \tag{4}$$

where K is the extinction coefficient and λ is the wavelength of light.

We did not observe any substantial spectral difference in the photocurrent spectra of unirradiated and irradiated samples for above bandgap illumination although there was a difference in absolute photocurrent level. All the states in the bandgap will be photoionized since the photon energy is higher than that of the bandgap.[43] As we increase the wavelength of light, the probing depth increases, as is predicted by the Eqs. (3) and (4). Thus, the in-depth spatial distribution of sub-gap states can be sequentially probed.

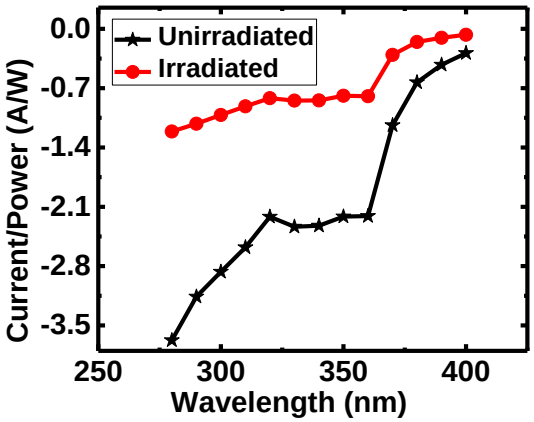

FIG. 9. (Color online) Normalized photo-current response for above bandgap illumination.

The normalized photocurrent spectra for both the unirradiated and irradiated samples are shown in Fig. 9, which were obtained by extracting the photocurrent value at -10 V from the data in Fig. 8. We also observed a slight decrease in the intensity of photocurrent on the irradiated sample with respect to the unirradiated one. This result again supports the aforementioned idea that the irradiation can cause quenching of the persistent photoconductivity.

Based on the experimental results of spectroscopic photo-IV measurements, it is confirmed that the sub-bandgap defects were present in the HEMT heterostructure and the gamma-ray irradiation induces the generation of additional defects and/or re-configure the pre-existing defects.

IV. SUMMARY AND CONCLUSIONS

The effect of gamma-ray irradiation (120 MRad dose) on AlGaN/GaN heterojunctions have been investigated. The results of transistor IV characteristics, CV, micro-Raman, PL and spectroscopic photo-IV measurement from unirradiated and irradiated samples were compared. It was found that the electrical characteristics of the irradiated HEMT samples were slightly degraded compared to the unirradiated ones. It was also observed that the gamma-ray irradiation causes a decrease in 2DEG carrier density and introduces acceptor-like deep level traps. The GaN layer was not additionally strained by the gamma-ray irradiation. In addition, it appears that the gamma-ray irradiation has quenched the persistent photoconductivity. Since we can exclude the possible radiation damage at MS junction and metal contacts, it can be conjectured that the observed degradation is produced by alteration of crystal quality in the bulk epi-layer structure. Based on these observations, it was concluded that AlGaN/GaN HEMTs is relatively resistant to high dose (120 MRad) gamma-ray irradiation, but it can introduce additional traps or re-configure the pre-existing traps, influencing the electrical and optical characteristics of AlGaN/GaN HEMTs.

ACKNOWLEDGMENTS

The author would like to thank Max Cichon for gamma-ray irradiation of the samples. And Park would like to thank Walter Professorship.

References

[1] K. Trachenko, "How the nature of the chemical bond governs resistance to amorphization by radiation damage," *Phys. Rev. B*, vol. 71, no. 18, 2005.

[2] V. Cimalla, J. Pezoldt, and O. Ambacher, "Group III nitride and SiC based MEMS and NEMS: materials properties, technology and applications," *J. Phys. Appl. Phys.*, vol. 40, no. 20, p. 6386, 2007.

[3] I. Yonenaga, "Mechanical Stability of Power Device Materials High Temperature Hardness of SiC, AlN and GaN," p. 3.

[4] C.-K. Sun, "Ultrafast electron dynamics study of GaN," *Phys. Rev. B*, vol. 59, no. 21, pp. 13535–13538, 1999.

[5] A. Ionascut-Nedelcescu, C. Carlone, A. Houdayer, H. J. von Bardeleben, J. L. Cantin, and S. Raymond, "Radiation hardness of gallium nitride," *IEEE Trans. Nucl. Sci.*, vol. 49, no. 6, pp. 2733–2738, Dec. 2002.

[6] I. B. Rowena, S. L. Selvaraj, and T. Egawa, "Buffer Thickness Contribution to Suppress Vertical Leakage Current With High Breakdown Field (2.3 MV/cm) for GaN on Si," *IEEE Electron Device Lett.* vol. 32, no. 11, pp. 1534–1536, Nov. 2011.

[7] C. A. Klein, "Bandgap Dependence and Related Features of Radiation Ionization Energies in Semiconductors," *J. Appl. Phys.*, vol. 39, no. 4, pp. 2029–2038, Mar. 1968.

[8] S. J. Pearton, F. Ren, E. Patrick, M. E. Law, and A. Y. Polyakov, "Review — Ionizing Radiation Damage Effects on GaN Devices," vol. 5, no. 2, 2016.

[9] S. A. Vitusevich, A. M. Kurakin, R. V. Konakova, A. E. Belyaev, and N. Klein, "Improvement of interface properties of AlGaN/GaN heterostructures under gamma-radiation," *Appl. Surf. Sci.*, vol. 255, no. 3, pp. 784–786, Nov. 2008.

[10] B. D. Weaver *et al.*, "Editors' Choice—On the Radiation Tolerance of AlGaN/GaN HEMTs," *ECS J. Solid State Sci. Technol.*, vol. 5, no. 7, pp. Q208–Q212, Jan. 2016.

[11] A. D. Koehler *et al.*, "Proton Radiation-Induced Void Formation in Ni/Au-Gated AlGaN/GaN HEMTs," *IEEE Electron Device Lett.*, vol. 35, no. 12, pp. 1194–1196, Dec. 2014.

[12] X. Hu *et al.*, "Proton-irradiation effects on AlGaN/AlN/GaN high electron mobility transistors," *IEEE Trans. Nucl. Sci.*, vol. 50, no. 6, pp. 1791–1796, Dec. 2003.

[13] E. J. Katz *et al.*, "Neutron irradiation effects on metal-gallium nitride contacts," *J. Appl. Phys.*, vol. 115, no. 12, p. 123705, Mar. 2014.

[14] C.-H. Lin *et al.*, “Neutron irradiation effects on gallium nitride-based Schottky diodes,” *Appl. Phys. Lett.*, vol. 103, no. 16, p. 162106, Oct. 2013.

[15] R. X. Wang *et al.*, “Micro-Raman and photoluminescence studies of neutron-irradiated gallium nitride epilayers,” 2005.

[16] Emtsev, V. V., V. Yu Davydov, V. V. Kozlovskii, V. V. Lundin, D. S. Poloskin, A. N. Smirnov, N. M. Shmidt et al. "Point defects in-irradiated n-GaN." *Semiconductor science and technology* 15, no. 1 (2000): 73.

[17] S. Tavernier, *Experimental Techniques in Nuclear and Particle Physics*. Springer Science & Business Media, 2010.

[18] B. Luo *et al.*, “Influence of 60Co γ-rays on dc performance of AlGaN/GaN high electron mobility transistors,” *Appl. Phys. Lett.*, vol. 80, no. 4, pp. 604–606, Jan. 2002.

[19] O. Aktas *et al.*, “60Co gamma radiation effects on DC, RF, and pulsed I–V characteristics of AlGaN/GaN HEMTs,” *Solid-State Electron.*, vol. 48, no. 3, pp. 471–475, Mar. 2004.

[20] S. A. Vitusevich *et al.*, “Effects of γ-irradiation on AlGaN/GaN-based HEMTs,” *Phys. Status Solidi A*, vol. 195, no. 1, pp. 101–105, Jan. 2003.

[21] Ş. Karataş, A. Türüt, and Ş. Altındal, “Effects of 60 Co γ-ray irradiation on the electrical characteristics of Au/n-GaAs (MS) structures,” *Nucl. Instrum. Methods Phys. Res. Sect. Accel. Spectrometers Detect. Assoc. Equip.*, vol. 555, no. 1, pp. 260–265, 2005.

[22] T. Azuhata, T. Sota, K. Suzuki, and S. Nakamura, “Polarized Raman spectra in GaN,” *J. Phys. Condens. Matter*, vol. 7, no. 10, p. L129, 1995.

[23] H. Siegle, “Zone-boundary phonons in hexagonal and cubic GaN,” *Phys. Rev. B*, vol. 55, no. 11, pp. 7000–7004, 1997.

[24] A. Abderrahmane *et al.*, “Effect of proton irradiation on AlGaN/GaN micro-Hall sensors,” *Appl. Phys. Lett.*, vol. 102, no. 19, p. 193510, May 2013.

[25] L. Lv *et al.*, “Proton Irradiation Effects on AlGaN/AlN/GaN Heterojunctions,” *IEEE Trans. Nucl. Sci.*, vol. 62, no. 1, pp. 300–305, Feb. 2015.

[26] B. Ozden *et al.*, “Analysis of Point Defect Distributions in AlGaN/GaN Heterostructures via Spectroscopic Photo Current-Voltage Measurements,” *ECS J. Solid State Sci. Technol.*, vol. 5, no. 4, pp. P3206–P3210, Jan. 2016.

[27] M. A. Reshchikov and H. Morkoç, “Luminescence properties of defects in GaN,” pp. 1–95, 2005.

[28] S. Jha *et al.*, “Stability of submicron AlGaN/GaN HEMT devices irradiated by gamma rays,” *Microelectron. Eng.*, vol. 86, no. 1, pp. 37–40, Jan. 2009.

[29] C. Schwarz *et al.*, "Gamma irradiation impact on electronic carrier transport in AlGaN/GaN high electron mobility transistors," *Appl. Phys. Lett.*, vol. 102, no. 6, p. 062102, Feb. 2013.

[30] H.-Y. Kim, J. Kim, L. Liu, C.-F. Lo, F. Ren, and S. J. Pearton, "Electrical characterization of 60Co gamma radiation-exposed InAlN/GaN high electron mobility transistors," *J. Vac. Sci. Technol. B*, vol. 31, no. 5, p. 051210, Sep. 2013.

[31] O. Ambacher *et al.*, "Two dimensional electron gases induced by spontaneous and piezoelectric polarization in undoped and doped AlGaN/GaN heterostructures," *J. Appl. Phys.*, vol. 87, no. 1, pp. 334–344, Dec. 1999.

[32] J. Kim, F. Ren, D. Schoenfeld, S. J. Pearton, A. G. Baca, and R. D. Briggs, "High Dose 60 Co γ -Ray Irradiation of W / GaN Schottky Diodes," pp. 124–127, 2004.

[33] L. Ling *et al.*, "Neutron irradiation effects on AlGaN/GaN high electron mobility transistors," *Chin. Phys. B*, vol. 21, no. 3, p. 037104, 2012.

[34] Z. Bi *et al.*, "The effects of proton irradiation on the electrical properties of NbAlO/AlGaN/GaN MIS-HEMT," *Sci. China Phys. Mech. Astron.*, vol. 55, no. 1, pp. 40–43, Jan. 2012.

[35] K. K. Allums *et al.*, "Effect of Proton Irradiation on Interface State Density in Sc2O3/GaN and Sc_2O_3/MgO/GaN Diodes," *J. Electron. Mater.* vol. 36, no. 4, pp. 519–523, Apr. 2007.

[36] G. A. Umana-Membreno *et al.*, "Annealing of C60o gamma radiation-induced damage in n-GaN Schottky barrier diodes," *J. Appl. Phys.*, vol. 101, no. 5, p. 054511, Mar. 2007.

[37] A. Y. Polyakov, S. J. Pearton, P. Frenzer, F. Ren, L. Liu, and J. Kim, "Radiation effects in GaN materials and devices," *J. Mater. Chem. C*, vol. 1, no. 5, pp. 877–887, 2013.

[38] A. Yadav *et al.*, "Effect of Annealing on Electronic Carrier Transport Properties of Gamma-Irradiated AlGaN/GaN High Electron Mobility Transistors," *ECS Trans.*, vol. 61, no. 4, pp. 171–177, Mar. 2014.

[39] N. M. Shmidt *et al.*, "Effect of Annealing on Defects in As-Grown and γ-Ray Irradiated n-GaN Layers," *Phys. Status Solidi B*, vol. 216, no. 1, pp. 533–536, Nov. 1999.

[40] F. Tong *et al.*, "Spectroscopic photo I-V diagnostics of nitride-based high electron mobility transistor structures on Si wafers," *Electron. Lett.* vol. 49, no. 24, pp. 1547–1548, Nov. 2013.

[41] J. Z. Li, J. Y. Lin, H. X. Jiang, M. Asif Khan, and Q. Chen, "Persistent photoconductivity in a two-dimensional electron gas system formed by an AlGaN/GaN heterostructure," *J. Appl. Phys.*, vol. 82, no. 3, pp. 1227–1230, Aug. 1997.

[42] A. Castaldini, A. Cavallini, and L. Polenta, "Radiation-induced effects in GaN by photoconductivity analysis," *Phys. Status Solidi A*, vol. 202, no. 15, pp. 2912–2919, Dec. 2005.

[43] B. Ozden *et al.*, "Depth-resolved ultra-violet spectroscopic photo current-voltage measurements for the analysis of AlGaN/GaN high electron mobility transistor epilayer deposited on Si," *Appl. Phys. Lett.*, vol. 105, no. 17, p. 172105, Oct. 2014.

Chapter 7

100 keV Proton Irradiation Effects on AlGaN/GaN HEMTs

This chapter is the following paper published in JOURNAL OF APPLIED PHYSICS **124**, 215702 (2018):

Impact of 100 keV proton irradiation on electronic and optical properties of AlGaN/GaN high electron mobility transistors (HEMTs)

Min P. Khanal[1], Sunil Uprety[1], Vahid Mirkhani[1], Shiqiang Wang[2], Kosala Yapa-bandara[1], Ehsan Hassani[3], Tamara Isaacs-Smith[1], Ayayi C. Ahyi[1], Michael J. Bozack[1], Tae-Sik Oh[3] and Minseo Park[1,1)]

[1]*Department of Physics, Auburn University, AL 36849, USA*

[2]*Department of Electrical and Computer Engineering, Auburn University, AL 36849, USA*

[3]*Department of Chemical Engineering, Auburn University, AL 36849, USA*

Proton irradiation-induced effects on AlGaN/GaN high electron mobility transistors (HEMTs) was studied by emulating a certain space radiation environment (upstream the earth's bow shock) using relatively low energy (100 keV) proton beam with fluences of 1×10^{10}, 1×10^{12}, and 1×10^{14} protons/cm^2. In order to isolate radiation-induced effects produced by the modification of the epi-layer from the effects produced by the change in device structure (such as contacts), the epi-layers were irradiated prior to device fabrication, followed by material/device characterization. Proton irradiation-induced sub-gap traps were detected by spectroscopic photocurrent-voltage (SPIV) measurement. Raman study revealed that the proton irradiation had induced strain relaxation on the AlGaN/GaN HEMTs epi-layer. No substantial change in the crystal quality of the epi-layer

[1)] Author to whom correspondence should be addressed. Electronic mail: park@physics.auburn.edu

was indicated by Raman and PL studies. With increasing proton fluences, increasing charge carrier density was observed, which was estimated *via* Raman spectroscopy and the charge-control model analysis. The magnitude and direction of the transistor threshold voltage shift were also dependent on proton fluence. Overall, the degradation of transistor output characteristics of the fabricated HEMTs was observed with increasing proton fluence. However, based on the observed performance and the level of influence on material/device characteristics by 100 keV protons, it can be suggested that the AlGaN/GaN HEMTs have high endurance for exposure to relatively high fluences of the low-energy proton beam.

I. INTRODUCTION

Radiation can be distinguished into two categories; those containing charged particles (α-particles, β-particles, protons, *etc*.) and those of a neutral nature (neutrons and γ-rays). Electronic devices exposed to space and terrestrial radiation environment interact with the energetic particles, resulting in detrimental effects on their characteristics. The main effects can be categorized as follows; (1) Single event effects (SEE) in which passage of a single highly-ionizing particle alters the operational state of a semiconductor device (*e.g.*, reverse the data state of a memory cell, change the logic state of a transistor). (2) Displacement damage (DD) effects where the collisions between irradiating particles and lattice atoms take place and cause atomic displacement in the material, resulting in the formation of Schottky or Frenkel defects in the crystal lattice. (3) Total ionization damage (TID) effects which are the long-term effects and result in a charge build-up at interfacial regions or boundaries between different layers due to ionization of the atoms.[1] It is necessary to identify and control the fault generating mechanisms if the semiconductor materials are to be used reliably as electronic devices in a hostile radiation environment such as space.[2]

The threshold displacement energy, E_d (typically used as an indicator for radiation hard-ness) varies inversely with the lattice constant of a semiconductor.[2] The reported values[3,4] of E_d for AlN and GaN, are 25 eV and~19.5 eV fitting the empirical relation for various semiconductors shown in Fig.1. This implies that the radiation hardness of III-N materials is higher than most of the semiconductor materials and other III-V materials such as GaAs, making the III-N devices excellent choices for radiation-hard applications. In addition, inherent material properties such as a strong ionic-covalent bond, large direct bandgap, excellent thermomechanical stability, ultrafast carrier relaxation time, high displacement energy, low phonon loss and higher breakdown field prompt III-N materials intrinsically viable for radiation hard electronics.[5] The heterostructure

guided features such as internal piezoelectric field[6] and formation of two-dimensional electron gas (2DEG) in a small confined cross section[7] are some of the uniqueness of aluminum gallium nitride/gallium nitride (AlGaN/GaN) high electron mobility transistors (HEMTs) structures, which provide additional radiation hardness.

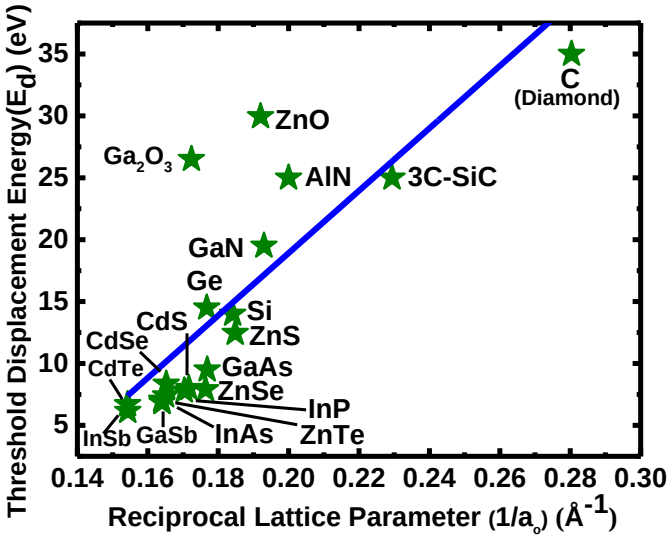

FIG. 1. The empirical relation between the mean threshold displacement energy (E_d) with the lattice parameter of various semiconductors. (Data were taken from Refs. 2-4).

Several studies have been reported on the effect of proton irradiation (or implantation) with various energies on AlGaN/GaN HEMTs.[8,9,10,11,12,13] However, only a few experimental reports have been released on the study of the effect of 100 keV protons on GaN and other III-V materials.[12,13] To the best of our knowledge, no research has been published on the study of the effect of 100 keV protons on AlGaN/GaN heterostructures.

In order to bypass the lethal radiation zone in Van Allen belts when launching a spacecraft/satellite, an alternate path (called as a polar escape route) has been proposed.[14,15] When supersonic solar wind encounters the earth's magnetosphere, it forms an aerodynamic shock wave in front of the nose of the magnetopause, and it extends over the polar regions of the earth, producing the so-called bow shock. Whenever interplanetary fields connect the spacecraft and the

earth's bow shock, protons with the cut off the energy of 100 keV are reported to be found up-stream from bow shock.[16,17]As a result, even if the polar escape route is chosen, electronics will still be exposed to protons. On the other hand, even though the high energy protons are present in space environments, electronic devices will not directly be exposed to such high energy protons. There will always be some shielding materials which prevent the energetic particles from directly entering into the electronics and during the course, energetic protons will slow down and lose the energy. Also, it has been reported that the degradation of electronic devices by low energy protons is more severe than the high energy protons.[18] Therefore, it is consequential to investigate the effects of low energy (100 keV) protons in the semiconductor materials.

In this research, the study was carried out on the effects of irradiation of 100 keV protons (with fluences of 1×10^{10}, 1×10^{12}, and 1×10^{14} protons/cm^2) on materials and device characteristics of AlGaN/GaN HEMTs. The pristine and irradiated AlGaN/GaN HEMTs were characterized by comparing the phenomenological changes in the electrical and optical properties, which was augmented by trap distribution analysis *via* the spectroscopic photocurrent-voltage technique.[19] The epitaxial layers were irradiated before constructing the devices because the primary interest of this study was to examine proton irradiation effects on the epi-layer itself rather than just the device characteristics although, metallic contacts need to be used in the actual applications of electronic devices. By irradiating the epilayers with no contacts, the effects of proton irradiation on the epi-layer itself can be isolated from any extra effects of energetic particles on metal-semiconductor (MS) interface and possible influence on the device characteristics caused from the irradiation-induced void formation on MS junction.[20] The surface compositional analysis was performed *via* x-ray photoelectron spectroscopy (XPS), and surface morphology was inspected using atomic force microscopy (AFM) and scanning electron microscopy (SEM). The crystal quality was

examined with x-ray diffraction (XRD) analysis and micro-Raman spectroscopy. The possible effects on defects/traps were probed using photoluminescence (PL) spectroscopy and the spectroscopic photocurrent-voltage (SPIV) techniques. The SPIV technique is one of the unique methods of mapping the defect distribution on the nitride-based semiconductors. Additionally, the conventional transistor current-voltage (I-V) measurements were performed on HEMTs to relate the material's fundamental properties to the device performance.

II. EXPERIMENTAL

The HEMT heterostructures were grown on 6 in. Si (111) wafers *via* metal-organic chemical vapor deposition (MOCVD) by a commercial wafer vendor. AlN nucleation layer was grown on top of Si, and AlGaN buffer multilayer with varied aluminum (Al) concentrations between 20%-75% was deposited on top of the AlN layer. An undoped GaN layer of thickness 1μm was deposited on top of the AlGaN buffer layer, followed by a 20 nm AlGaN barrier layer. A GaN cap layer with a thickness of 2 nm was grown on top of the barrier layer.

To irradiate the HEMT epitaxial layers with a proton beam, the 6 in. wafer was diced into 1 × 1 cm pieces, and those pieces were further diced into four 5 × 5 mm pieces. One of the pieces was left unirradiated (hereafter to be called pristine) and the other three pieces were irradiated at room temperature with 100 keV proton beam of 1×10^{10}, 1×10^{12} and 1×10^{14} protons/cm^2 fluences generated from a 2 MV dual source Tandem Pelletron accelerator located at Auburn University. The accuracy of the proton beam energy (monitored by the beam current) was maintained at 99.9%. The Stopping and Range of Ions in Matter (SRIM)[21] simulator was used to estimate the penetration depth, distribution of protons and the total vacancy concentration in AlGaN/GaN HEMTs structure. For 100 keV protons, the penetration depth of the proton beam was estimated to be 0.57 μm with a straggle of 883 Å, for the HEMTs structure under study. Therefore, the

maximum proton distribution was at the undoped GaN layer where the beam was stopped. The total number of vacancies (in cm^{-3}) for each fluence was estimated to be in the order of 10^{15}, 10^{17} and 10^{19} respectively for 1×10^{10}, 1×10^{12} and 1×10^{14} protons/cm^2. The transistor devices with varying dimensions were fabricated, and circular geometry was used to avoid mesa isolation. Source and drain Ohmic contacts (Ti/Al/Ni) were deposited using direct-current (dc) magnetron sputtering, followed by rapid thermal annealing at 850 ^oC for 30 s under a nitrogen atmosphere. Finally, Iridium (Ir) metal was sputter-deposited as a gate contact. In order to perform the SPIV experiment, an array of circular semitransparent Ni Schottky contacts with a diameter of 600 μm were constructed on the HEMTs wafers.

The electrical characteristics of transistor devices were studied at room temperature on an H-100 Signatone probe station equipped with a Keithly 2400-source meters automated with LabVIEW program. Micro-Raman spectroscopy was performed on both the pristine and irradiated samples at room temperature by employing back-scattering geometry using the 442 nm line (80 mW) of a dual wavelength Kimmon He-Cd laser. The spectra were dispersed using a diffraction grating with 3600 lines/mm groove density. The room temperature micro-PL measurements were carried out by exciting the samples with the 325 nm line (20 mW) of He-Cd laser. XPS measurements were performed in a load-locked Kratos XSAM 800 surface analysis system equipped with a hemispherical energy analyzer. The photoelectrons were excited by a water-cooled, conventional (*i.e.*, non-monochromatic) dual anode X-ray gun equipped with an Al window. MgK_α (1253.6 eV) radiation was used exclusively. The surface composition was calculated based on the Scofield cross-sectional values accounting for the instrumental transmission function in the FAT mode of operation. The XRD analysis was performed using Proto-AXRD theta-theta diffractometer with X-ray K_α line from the Cu target with 40 kV@ 30 mA. The SPIV measurements were performed

by illuminating the samples using a Xenon lamp light source coupled with a monochromator to vary the wavelength. Samples were vertically biased, applying a reverse voltage to the top Schottky contacts. Keithly 6487 picoammeter with a built-in voltage source was used for biasing and collecting photocurrent.

III. RESULTS AND DISCUSSION

A. Raman Spectroscopy

Raman scattering in solids is an inelastic process which depends on the change in polarizability of the material caused by optical excitation of phonons or plasmons. Valence electrons in covalent crystals are less localized compared to the ones in ionic crystals, so larger fluctuation of electric susceptibility leads to a higher change in polarizability induced by the annihilation and creation of phonons which gives a higher scattering efficiency for covalent crystals compared to ionic ones. Therefore, Raman spectroscopy is a suitable and well established standard technique to study the lattice properties of nitride-based semiconductors whose chemical bonding is a mixture of covalent and ionic bonding.[22] The hexagonal wurtzite structure of GaN belongs to C_{6v}^4 space group and its primitive unit cell contains four atoms. According to group theory, 12 phonon normal modes (irreducible representation) exist at the Γ-point of Brillouin zone. Among those, $A_1(z) + E_1(x, y) + 2B_1 + 2E_2$ are optical modes and remaining modes are acoustic. The A_1 and E_1 modes are both Raman and infrared (IR) active, E_2 modes belong to only Raman active phonons, whereas B_1 modes are silent. Due to the macroscopic electric field affiliated with longitudinal modes, the polar $A_1$and E_1 modes split into transverse optical (TO) and longitudinal optical (LO) phonon modes with different frequencies.[23] In this study, the Raman scattering was employed to examine

the crystal quality, strain, and to estimate the free carrier concentration of the samples. The physical structure of crystals can be examined from the Raman spectroscopy by analyzing the characteristic spectral patterns.

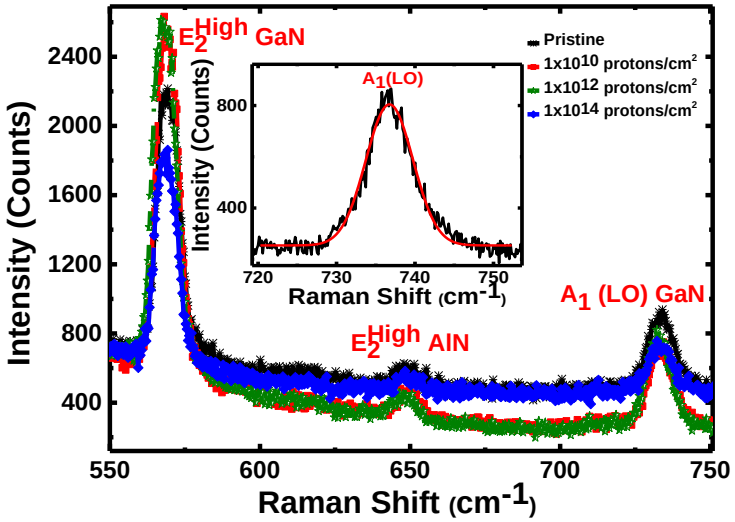

FIG. 2. Raman spectra of the pristine and irradiated samples (inset shows the representative Gaussian fitted curve for carrier concentration calculation from LO phonon mode).

Figure 2 shows the typical Raman scattering spectra of the pristine and proton-irradiated samples collected at room temperature. The experiment was performed with $z\ (-,-)\bar{z}$ back scattering geometry, and E_2^{High} and $A_1(LO)$ modes for GaN along with the E_2^{High} mode for AlN were observed. The observed parameters for collected spectra of pristine and irradiated samples are summarized in Table I. No severe degradation in the crystal quality of heterostructure was observed after 100 keV proton irradiation of AlGaN/GaN heterostructures on Si.

As shown in Table I, there is a small shift in the frequency position towards lower wavenumber and a slight increase in the full width at half maximum (FWHM) of irradiated samples in reference to the pristine sample. From the small shift of the Raman E_2^{High} phonon mode to a lower wavenumber, it can be speculated that proton irradiation has induced a strain relaxation in the heterostructure.[24]

Table I: The extracted parameters from Raman spectra for pristine and proton-irradiated samples

Sample	Peak Position (cm^{-1})		FWHM (cm^{-1})		Free Carrier Concentration (cm^{-3})	Biaxial Stress Coefficient σ_{xx} (GPa)
Fluence (protons/cm^2)	E_2^{high} mode	$A_1(LO)$ mode	E_2^{high} mode	$A_1(LO)$ mode		
Pristine	569.4	736.6	9.0	11.2	9.5×10^{16}	0.44
1×10^{10}	569.0	736.3	9.5	10.8	8.4×10^{16}	0.35
1×10^{12}	568.2	736.7	10.0	11.2	9.9×10^{16}	0.16
1×10^{14}	568.7	736.7	9.7	10.5	9.9×10^{16}	0.27

The frequency position of $A_1(LO)$ phonon mode can be used to calculate the free carrier concentration in the bulk using the following expression[25];

$$n\,(x,y) = \frac{\varepsilon_0\,\varepsilon_\infty m*}{e^2}\frac{\omega_{LPP}^2\,(x,y)[\omega_{LPP}^2(x,y)-\omega_{LO}^2]}{\omega_{LPP(x,y)}^2-\omega_{TO}^2} \quad (1)$$

where n is free carrier concentration, ω_P is the plasmon frequency, ω_{LPP} is the longitudinal optical phonon-plasma frequency, ω_{LO} is the frequency of the longitudinal optical phonon, ω_{TO} is the frequency of the transverse optical phonon, ε_0 is the permittivity of the free space, ε_∞ high frequency (optical) dielectric constant, m^* is the effective mass of free a carrier, and e is a charge of the free carrier.

The free carrier concentration values reported in Table I were calculated using Eq. (1). An increase in free carrier concentration was observed on the samples irradiated with higher proton fluences. However, since the strain can also shift the $A_1(LO)$ peak position, we separated the contribution of free carrier concentration on the position shift of $A_1(LO)$ mode from the contribution of strain relaxation by using the following relations;[26] $\Delta\omega = 4.47\,\sigma_{xx}$ for E_2^{High} and $\Delta\omega = 2.76\,\sigma_{xx}$ for $A_1(LO)$ modes. For this calculation, the shift was considered with respect to the stress

free frequencies of 567.6 cm^{-1} and 734.0 cm^{-1} for E_2^{High} and $A_1(LO)$ GaN Raman modes, repectively.[23] After the strain correction, an increase in n value was observed and the strain relaxation can be claimed on the basis of reported values of σ_{xx} in Table I.

B. Photoluminescence

Photoluminescence spectroscopy can be used to examine the crystal quality and the impurity levels in the semiconductors and is also useful in probing their defect distribution. We have employed the PL to study the optical properties and hence to examine the crystal quality and the defects of pristine and proton-irradiated samples. Figures 3(a) and 3(b) respectively show the broad (UV-Visible) range and the short (UV) range scan room-temperature PL spectra for pristine and the three irradiated samples. The PL spectra exhibited two main bands; a near band edge (NBE) emission with the pronounced peak at ~3.42 eV and a broad blue luminescence (BL) band peaking at around 2.81 eV. The NBE band emission is associated with the recombination process involving the annihilation of free excitons and excitons bound to shallow donors[27] whereas the origin of BL band is assigned to the donor-acceptor (DA) recombination, *i.e.*, transitions from the conduction band or a shallow donor to a relatively deep acceptor.[28,29,30] The GaN featuring BL band is the signature of a material containing a high density of dislocations.[31]

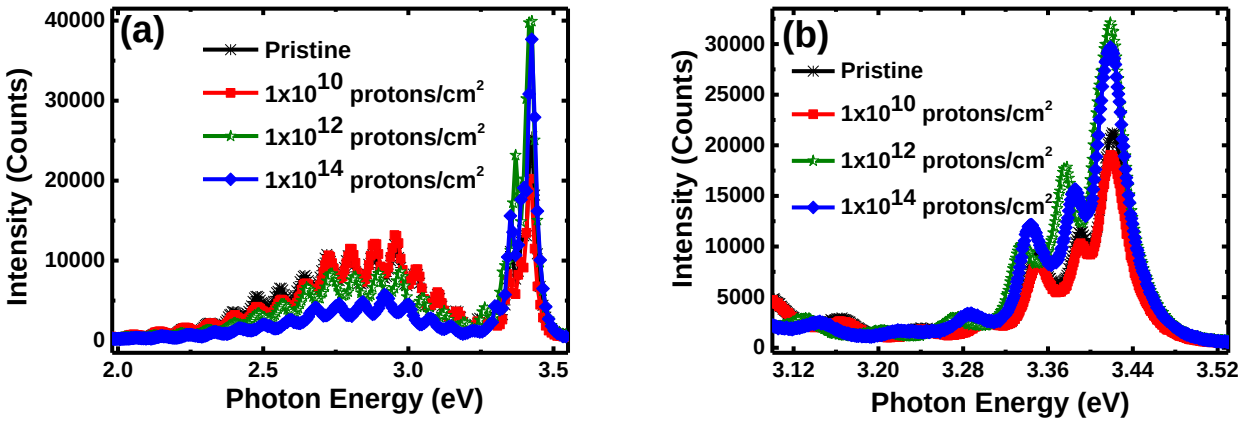

FIG. 3. Photoluminescence spectra of the pristine and irradiated samples (a) broad (UV-Visible) range scan and (b) short (UV) range only scan.

As can be seen from both Figs. 3(a) and (b), the intensity and the peak position of PL spectra for proton irradiation sample with fluence 1×10^{10} protons/cm^2 and pristine sample are nearly identical. However, the intensity of BL band was slightly quenched after proton irradiation with the higher fluences (1×10^{12} and 1×10^{14} protons/cm^2), which possibly indicates the formation of new deep centers leading to the dominance of non-radiative recombination. The enhancement in the intensity of the NBE emission is observed for the HEMTs with the higher fluences. The observed results are similar to previously reported results.[32] The increase in the intensity of NBE emission needs to be further investigated considering how radiation-induced defects modulate the origin of recombination centers.

C. X-ray Diffraction

Figure 4 shows the XRD data probed from a symmetrical lattice plane (0002) for the pristine and proton irradiated AlGaN/GaN HEMT structures. Since HEMT structure has multilayer geometry, the diffraction pattern includes multiple peaks; the main peak from GaN layer and consecutive peaks due to AlGaN layers with different Al to Ga ratio, gradually shifting the peak position towards the higher angle with the increasing Al content.[33] In addition, we can observe the peak contributed from the AlN nucleation layer in the heterostructure. Similar to PL data, the XRD data show that the difference in peak position and the intensities of 1×10^{10} fluence irradiated and pristine samples is relatively negligible, indicating that the crystal structure variation for lower fluence is quite small. The peak intensities of the samples irradiated at the higher fluences 1×10^{12} and 1×10^{14} seem to be enhanced, and the observed oscillation in the peak position for all curves is attributed to the slight variation in Al content during the growth/or chemical stability of AlGaN

layer upon irradiation.[34] It is expected that proton irradiation would normally produce a large number of defects.[35] However, the observed increase in XRD intensity indicates the reduction in defect concentration, which might be due to the defects being annealed out if the electronic energy loss of bombarded proton is higher than the nuclear energy loss.[36]

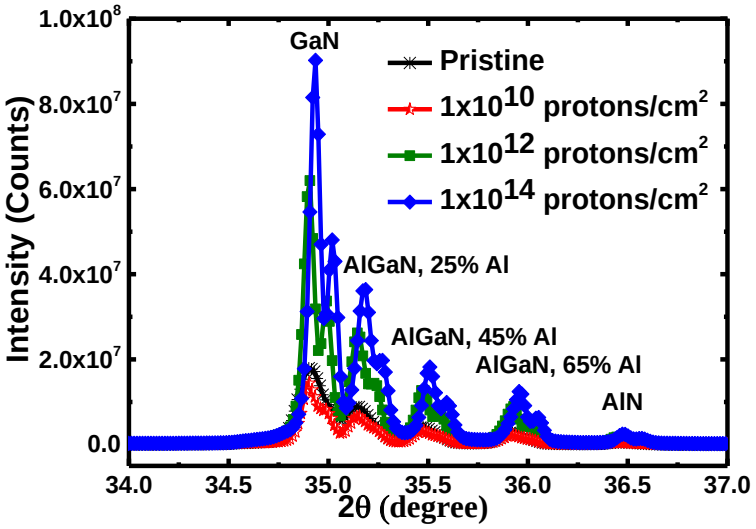

FIG. 4. XRD θ-2θ patterns of AlGaN/GaN heterostructures.

A. X-ray Photoelectron Spectroscopy

The XPS survey spectra recorded from the pristine and proton-irradiated samples are presented in Fig. 5(a). In addition, Fig. 5(b) shows the high-resolution XPS spectra of Ga-3d core-level. The survey spectra indicate the presence of peaks related to core-levels from Ga-3d, Ga-3p, Ga (LMM), C-1s, N-1s, and O-1s. The presence of oxygen and carbon on the surface are due to adsorption of common atmospheric gases during the epilayer growth and device processing steps. Analysis of Ga-3d region is useful to elucidate the nature of chemical bonding in GaN and related materials.[37] *No significant change* (in both the peak intensity and the binding energy) was observed in the Ga-3d spectra of proton-irradiated samples in comparison to the spectra from the pristine one.

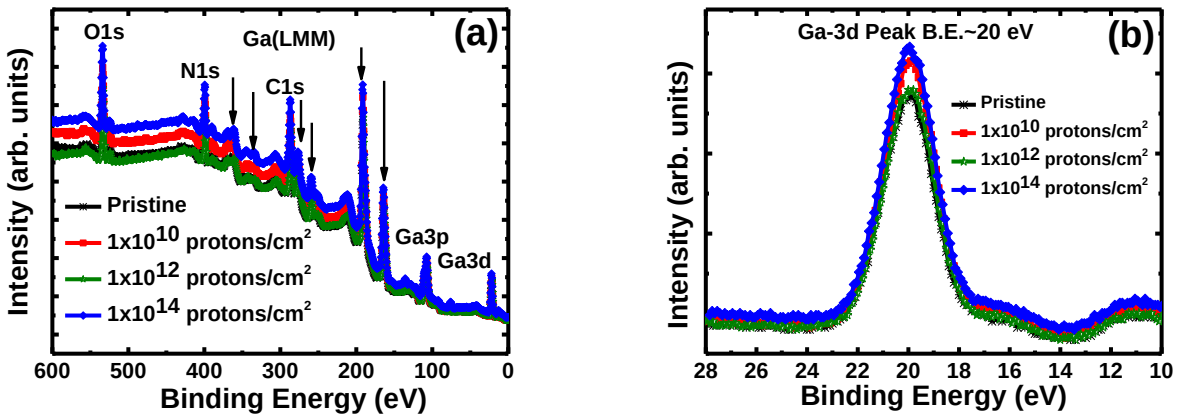

FIG. 5. (a) XPS survey spectra of all three samples (b) high-resolution XPS scan spectra of Ga-3d region.

Table II: The measured binding energy and FWHM of the Ga-3d XPS peak for pristine and proton-irradiated samples.

Sample	Ga-3d peak		Surface Elemental Composition (%)			
Fluence (protons/cm^2)	Binding Energy (eV)	FWHM	Ga	N	C	O
Pristine	19.92	2.40	24.2	13.8	48.5	13.5
1×10^{10}	20.03	2.38	21.7	13.7	51.2	13.4
1×10^{12}	19.97	2.40	22.8	12.9	49.8	14.5
1×10^{14}	20.02	2.25	20.3	15.3	50.4	14.0

The measured FWHM and the binding energy (BE) of Ga-3d core-level spectra for the pristine and the proton-irradiated samples are tabulated in Table II. No variation in the B.E. of the Ga-3d region signifies that the Ga-N bonding was not affected by proton irradiation.[38] Since the surface elemental composition of the pristine and irradiated samples are very close to each other. Therefore, it can be inferred that the surface composition of the samples was not altered by the proton irradiation.

B. Atomic Force Microscopy

Figure 6 shows the representative two-dimensional (2D) AFM images (10×10 μm^2) of Al-GaN/GaN heterostructures. Figure 6(a) shows the AFM image of the pristine sample whereas the

Figs. 6(b)-6(d) show the surface morphologies of 1×10^{10}, 1×10^{12} and 1×10^{14} protons/cm^2 irradiated samples, respectively. The root mean square value of surface roughness (Rq) for the pristine sample was 0.804 nm and for proton-irradiated samples, it was 1.935 nm, 1.460 nm and 1.060 nm for 1×10^{10}, 1×10^{12} and 1×10^{14} protons/cm^2, respectively. In comparison to the pristine sample, the surface roughness of the irradiated samples has increased, which might have been caused by the introduction of point defects and increased local disorder of the material.[32,39]

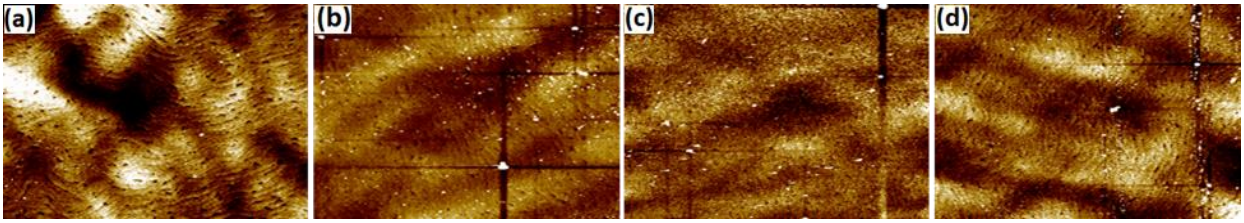

FIG. 6. Typical AFM images (10×10 μm^2 scan) of AlGaN/GaN heterostructures (a) pristine sample; and samples irradiated with fluence of (b) 1×10^{10} protons/cm^2 (c) 1×10^{12} protons/cm^2 and (d) 1×10^{14} protons/cm^2.

C. Scanning Electron Microscopy

Figure 7 shows the top surface view of the scanning electron microscopy (SEM) micrographs of AlGaN/GaN HEMTs heterostructures. The surface morphology of both the pristine and the irradiated samples appears relatively uniform. However, the surface roughness of proton-irradiated samples seemed to be increased in reference to the pristine sample. From the close inspection of the images, the decreasing trend of roughness on the irradiated samples appears to agree with the AFM results.

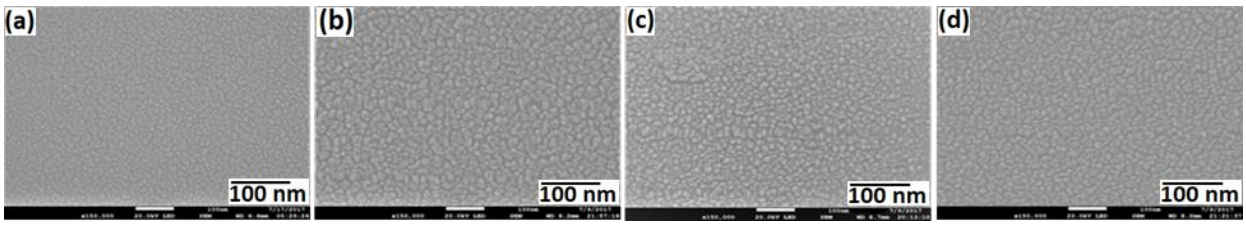

FIG. 7. HEMTs heterostructure SEM images of (a) pristine sample; and samples irradiated with fluence of (b) 1×10^{10} protons/cm^2 (c) 1×10^{12} protons/cm^2 and (d) 1×10^{14} protons/cm^2.

D. Transistor Characteristics

Figure 8 illustrates the drain *I-V* characteristics of the HEMTs devices with their epi-layers irradiated with different fluences. Gate voltage was modulated from -3V to 3V at the steps of 0.5V. The reduction in drain saturation current for the proton-irradiated samples can be seen in Fig. 8. The drain current was reduced by about 27% for proton irradiated sample with lower fluence (1×10^{10} protons/cm^2). In contrast, the reduction in drain saturation current for the devices with higher fluences (1×10^{12} and 1×10^{14} protons/cm^2) of proton irradiation was much higher (about 45% and 43%).

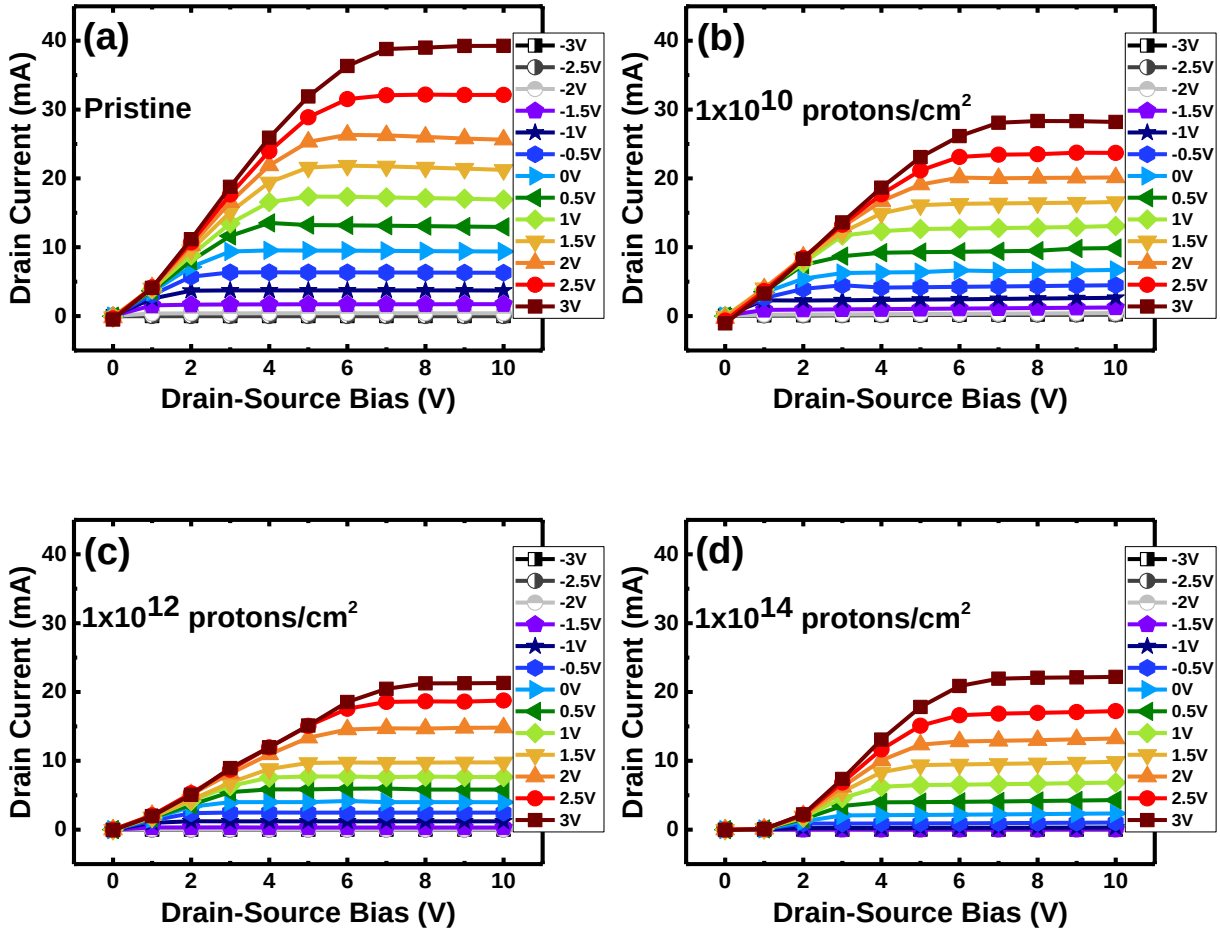

FIG. 8. Drain-source current-voltage characteristics of (a) pristine sample; and samples irradiated with fluence of (b) 1×10^{10} protons/cm^2 (c) 1×10^{12} protons/cm^2 and (d) 1×10^{14} protons/cm^2.

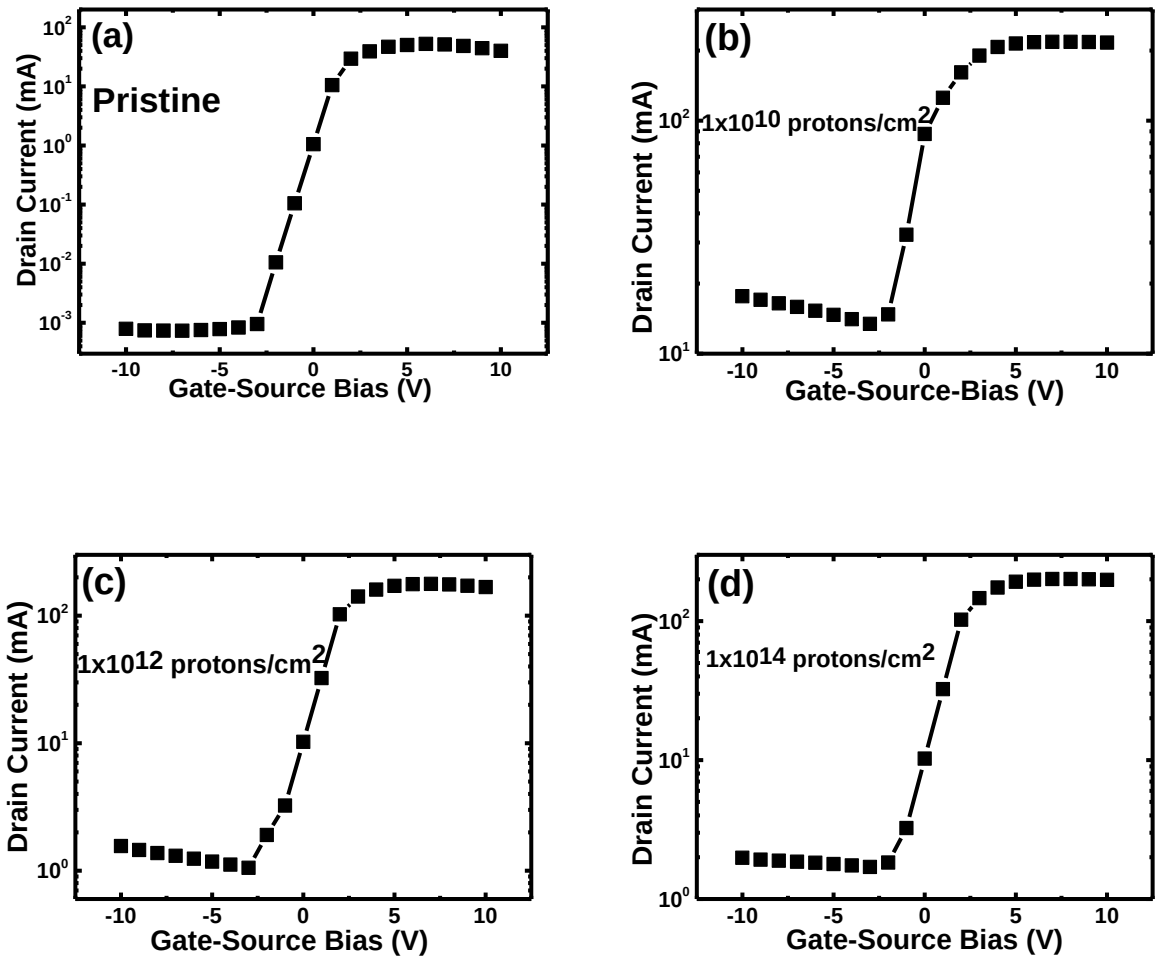

FIG. 9. Transfer characteristics of (a) pristine sample; and samples irradiated with fluence of (b) 1×10^{10} protons/cm^2 (c) 1×10^{12} protons/cm^2 and (d) 1×10^{14} protons/cm^2.

Figure 9(a) shows the transfer characteristics of the pristine sample and Figs. 9(b)-9(d) show the transfer characteristics of proton irradiated HEMTs devices for fluences of 1×10^{10}, 1×10^{12}, and 1×10^{14} protons/cm^2, respectively. The threshold voltage (V_{TH}) was calculated from the extrapolation of the square root of drain current *vs.* gate-source voltage plot in the saturation region. The proton-irradiated devices with a fluence of 1×10^{10} protons/cm^2 showed a positive shift in V_{TH} with respect to the pristine sample (-1.49 V to -1.07 V), which is commonly observed in many of the earlier published reports.[40,41,42] However, the negative shift in the threshold voltage of

proton irradiated HEMTs has also been reported.[43,44,45] Our experimental results (V_{TH} = -1.99 V) of proton irradiated devices with the higher fluences (1×10^{12} and 1×10^{14} protons/cm^2) is consistent with later reports. According to the previous reports, the direction of the threshold voltage shift for proton irradiated HEMTs can be either positive or negative. Various parameters such as growth condition, the energy of protons, fluence of the proton beam, and the damage might affect the direction of threshold voltage shift.[43]

The AlGaN/GaN system under this study can be analogous to the GaAs-HEMT system, thus can be described using the charge-control model.[46] According to the charge-control model, the sheet carrier density (n_s) and the sheet carrier mobility (μ) of the 2DEG can be simply estimated using the following relation[40]:

$$n_s = \frac{\varepsilon(V_{GS} - V_{TH})}{qt} \tag{2}$$

where ε is the dielectric constant of AlGaN, V_{GS} is the gate-source voltage where 2V is used for the calculation ($V_{TH} \leq V_{GS} \leq V_{GS,max}$), and V_{TH} is the threshold voltage, q is the electronic charge, and t is the thickness of the AlGaN barrier layer.

The sheet carrier mobility is calculated from the reciprocal of the slope of the $\frac{V_{DS}}{I_{DS}}$ *vs.* $\frac{1}{(V_{GS}-V_{TH})}$ the plot of Eq. (3).

$$\frac{V_{DS}}{I_{DS}} = R_S + R_D + \frac{L\,t}{W\,\mu\,\varepsilon\,(V_{GS} - V_{TH})} \tag{3}$$

where V_{DS} and I_{DS} are the drain–source voltage and current, respectively, R_S and R_D are the source and drain access resistances, respectively, and W and L are the gate width and the length, respectively. The $\frac{V_{DS}}{I_{DS}}$ is calculated in the linear region (low drain voltage) of the *I-V* curve, the slope of the curve related to the sheet carrier mobility, and the intercept is related to R_S and R_D.

The calculated values of the sheet carrier density (n_s) and the mobility are listed in Table III below. The mobility of the irradiated samples was significantly degraded; possibly due to carrier scattering caused by charged defects introduced by protons.[40] The reduction in the sheet carrier density was observed for the low proton fluence irradiated sample while an increase in n_s is observed for proton irradiated samples with the higher fluences. These changes in 2DEG sheet carrier density are in agreement with the direction of V_{TH} shift. The increase in carrier density was also reported earlier for proton irradiated HEMTs grown on Si, under similar doses but with a different proton energy.[47] The trend in the change of sheet carrier density is similar to the trend of changes in the free carrier concentration estimated earlier *via* micro-Raman analysis. It is speculated that protons have an influence on the migration and recombination of mobile defects and may release additional carriers from the traps in the channel. Also, proton irradiation may shift or pin the Fermi level near or in the conduction band leading to an increase in the carrier density.[48]

The irradiation-induced displacement damage may reduce the carrier density and mobility of 2DEG, resulting in a decrease of drain saturation current. It is not surprising to consider that both Ga-vacancy and N-vacancy related defects likely contribute[49] to the radiation response in GaN. Furthermore, both donor and acceptor trap formation during proton irradiation had been reported.[50] As can be seen from Table III, both sheet carrier density and mobility of the irradiated sample with fluence 1×10^{10} protons/cm^2 has been decreased, which is mainly due to the displacement damage induced by ion bombardment. These changes can produce a positive shift in the threshold voltage.[43,44] Therefore, the positive V_{TH} shift for the low proton fluence can be attributed to the increasing number of acceptor-like traps. However, V_{TH} shifted towards the same negative value for proton irradiated samples with the higher fluences (1×10^{12} and1×10^{14} cm^{-2}). The negative shift of V_{TH} can be caused by an increase in positive charge and/or a decrease in a pre-existing

negative charge. At higher proton fluences, the impurities like oxygen may lead to the creation of new donor traps[50], leading to a negative V_{TH} shift. Based on the simulation results from SRIM, the penetration depth of 100 keV protons used was 0.57 μm with a straggle of 883 Å. However, the total thickness of the layers above the GaN channel was just 0.022 μm and the GaN channel layer itself was 1 μm thick. Therefore, the maximum and the end of range distribution of protons was away from the thin 2DEG layer and the high concentration of proton induced defects would lie in a region away from the 2DEG region[51] and hence the impact of protons on 2DEG will be minimal. Consequently, the radiation induced effects on device level performance of HEMTs was relatively small.

The Schottky barrier height (Φ_B) was calculated from the forward gate *I-V* characteristics of HEMTs devices using the following expression;

$$\Phi_B = \frac{k_B T}{q} \ln\left(\frac{AA^* T^2}{I_s}\right) \tag{4}$$

where k_B is Boltzmann's constant, T is the temperature, q is the electronic charge, A is gate area, A^* is Richardson's constant and I_s is the saturation current which was determined by extrapolating the semilog *I vs V* curve to *V* = 0 in Eq.(5). The current through a Schottky diode can be written as follows:

$$I = I_s\left[e^{\frac{qV}{nk_BT}} - 1\right] \tag{5}$$

The slope of this plot is related to the ideality factor (n) and is expressed by;

$$n = \frac{q}{(2.3k_BT)slope} \tag{6}$$

Table III: The extracted parameters from electrical measurements of pristine and proton- irradiated samples

Fluence (protons/cm^2)	Sheet carrier density n_s (cm^{-2})	Mobility μ (cm^2/V.s)	Schottky barrier height Φ_B (eV)	leality factor (n)	Threshold Voltage V_{TH} (V)
Pristine	0.99× 10^{13}	1739	0.30	67.70	-1.49
1×10^{10}	0.87× 10^{13}	801	0.32	63.33	-1.07
1×10^{12}	1.14× 10^{13}	486	0.32	62.77	-1.99
1×10^{14}	1.14× 10^{13}	111	0.32	55.11	-1.99

Band bending on the AlGaN/GaN heterostructures due to proton irradiation has been reported earlier which can eventually affect the Schottky barrier height.[52] An increase in the value of Schottky barrier height on the irradiated samples in comparison to the pristine sample was observed. The calculated ideality factor is much higher than the expected value. When the materials with a large lattice mismatch form a heterojunction, a high density of trap states can be expected, which might result in an abnormally high ideality factor.[53] The pre-existence of traps in the samples were also confirmed by the SPIV experiment described in a later section Sec. III H.

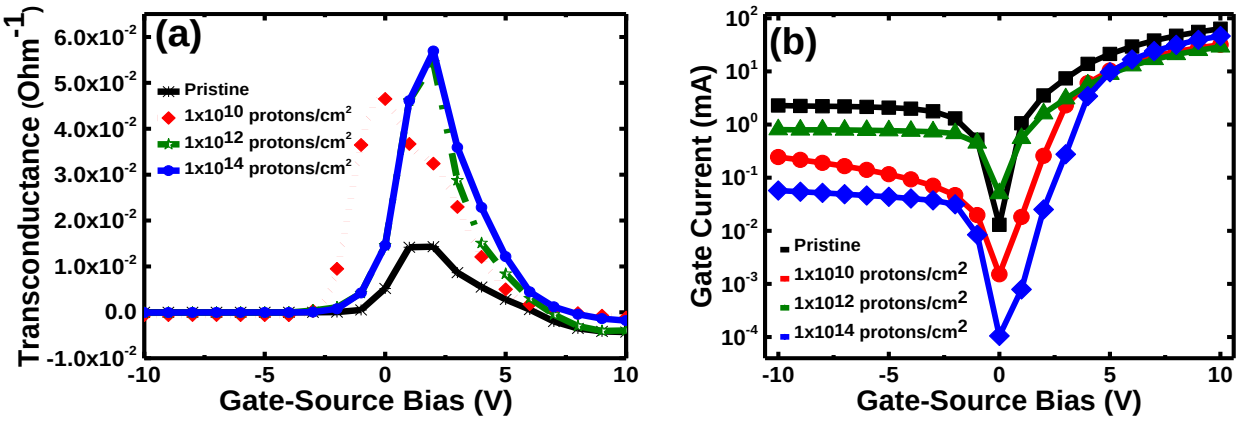

FIG. 10. (a) Transconductance and (b) forward and reverse gate bias I-V characteristics of pristine and irradiated samples.

From Fig. 10(a), it was observed that the transconductance of proton-irradiated devices increased. The increase in the transconductance can be attributed to the irradiation-induced strain

relaxation AlGaN/GaN HEMTs.[8,54] Further, irradiation-induced strain relaxation can result in the generation of additional defects or structural reordering of native defects[24] which is presented in the later SPIV section. The strain relaxation might be another plausible reason for the degradation in drain saturation current,[55] as shown in Fig. 8.

Figure 10(b) illustrates the forward-reverse gate bias *I-V* characteristics. Both the forward and reverse bias leakage currents decreased after proton irradiation with respect to the pristine samples. Proton irradiation can induce voids at the MS junction, resulting in a decrease of effective gate area and the gate leakage current.[20] This possibility can be ruled out in this study because the contacts were formed after proton irradiation of the epi-structures. The calculated values of Schottky barrier heights for the pristine and proton-irradiated samples are listed in Table III. The increase in Φ_B can be attributed to decreased gate leakage current as seen in Fig. 10(b).

As explained in the experimental section, during the process of ohmic contact metallization, the annealing was unavoidable for AlGaN/GaN HEMTs. Annealing of the proton irradiation-induced defects and partial recovery of the device characteristics have been reported previously.[9,10,45] However, for high doses of low energy proton implantation on GaN, the induced defects are more permanent and have higher thermal stability.[12] In presented results, for the devices irradiated with higher fluences, the level of device degradation was higher even after the annealing. Therefore, we believe that these results support the later claim.

E. Spectroscopic Photo-IV

The spectroscopic photo-IV method relies on the principle of an optical technique called "photoionization-spectroscopy" which has been used to probe the deep traps in AlGaN/GaN HEMTs.[56] When photons carrying energies above the threshold trapping energy fall into deep traps, the trapped carriers will be released, leading to the deep level-to-band electronic transition

of carriers, consequently increasing the output current. Photoluminescence spectroscopy only probes the radiative transition of carriers. However, in spectroscopic photo-IV, both radiative and non-radiative transitions of charge carriers can be analyzed to probe the in-gap trapping states. Moreover, the in-depth distribution of defects can be probed by varying the wavelength of incident light. The details of the technique can be found elsewhere.[57]

Figure 11 shows the spectroscopic photo-IV spectra with the sub-bandgap illumination of the pristine [Fig. 11 (a)] and the irradiated [Fig. 11(b, c, d)] samples. The wavelength was varied from 800 nm to 400 nm with a step of 50 nm. The sub-bandgap illumination excites the carriers from the deep traps and hence contributes to the photocurrent. So, by analyzing the spectral variation in response to the wavelength of light, information about the sub-bandgap energy levels of the defects within the bandgap can be extracted.

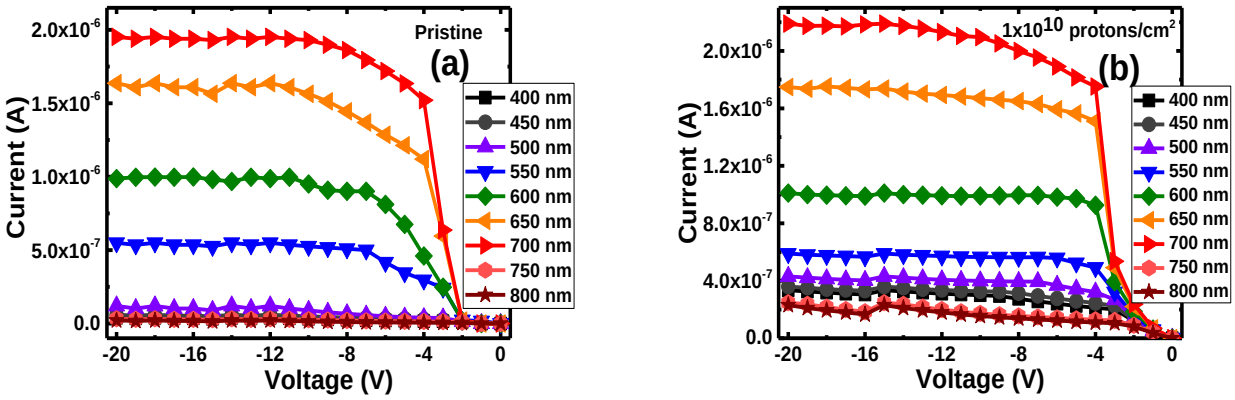

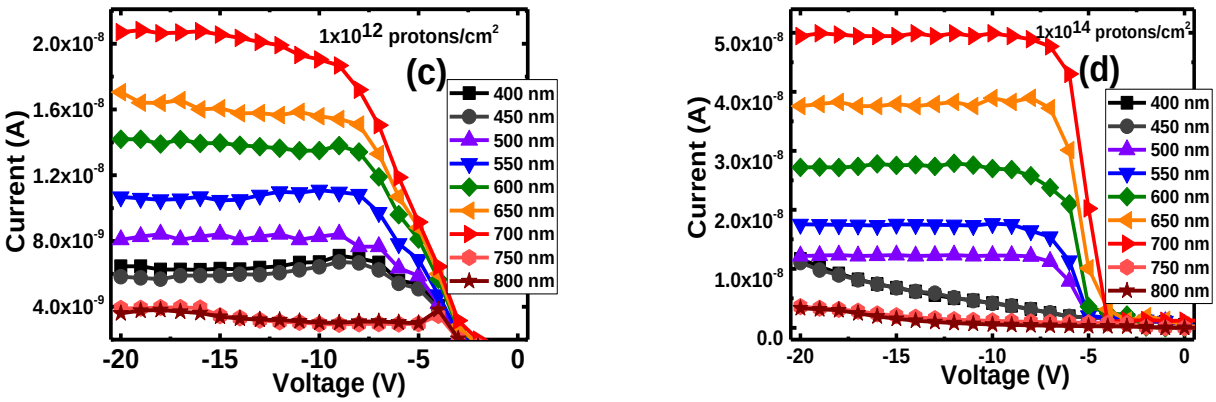

FIG. 11. Spectroscopic photo-IV (absolute) data with sub-bandgap illumination of (a) pristine sample; and samples irradiated with fluence of (b) 1×10^{10} protons/cm^2 (c) 1×10^{12} protons/cm^2 and (d) 1×10^{14} protons/cm^2.

Figure 12 shows the photocurrent response (normalized with an optical power of the lamp used as a source) for sub-bandgap illumination, where representative data for each bias at -12 V were chosen. Because of the well-known phenomena called "persistent photoconductivity" in GaN and related materials, the reduction in photocurrent is expected during the sequential measurements. Therefore, due to the presence of sub-gap defects in the sample, the photocurrent spectra should exponentially reduce as the measurement is repeated.[58] The categorical photocurrent spectra can be observed in Fig. 11(a), confirming the existence of sub-bandgap native defects in the pristine sample. From Fig. 12, it can be observed that there is no shift in spectral peak position even after proton irradiation in reference to the pristine sample. However, a significant increase in the absolute value of photocurrent response can be observed [Fig. 11(c, d) and Fig. 12] for the irradiated samples with the higher fluences. This increase might clue in the addition of more trap centers (near the pre-existing traps) due to the higher fluence of proton irradiation. This assumption is supported by the fact that the generated point defects in GaN are highly mobile and can easily be rearranged[47] and since the trapped carriers in those traps are excited by an absorbed photon,

hence they contribute to the increase in the level of photocurrent. The presence of native defects and their spectral location in the sub-gap region of the pristine sample has been confirmed. In addition, after the irradiation of 100 keV proton with the fluences of 1×10^{10}, 1×10^{12}, 1×10^{14} protons/cm^2, and the creation of additional traps whose energy levels are close to those of the pre-existing traps was speculated.

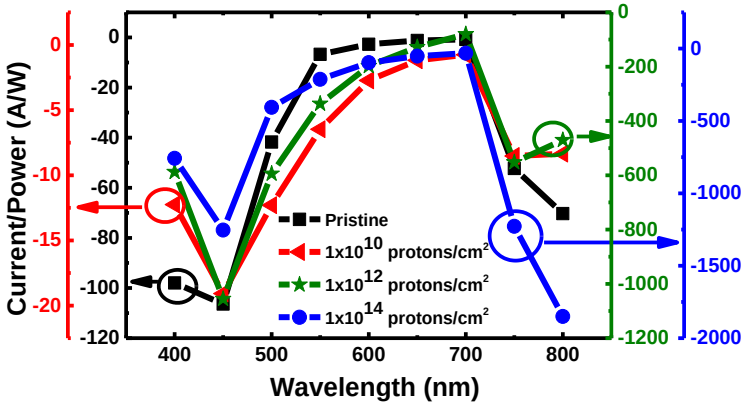

FIG. 12. Normalized photocurrent response with sub-bandgap illumination at -12V bias.

In addition to the sub-bandgap illumination, the depth-resolved ultraviolet spectroscopic photo-IV (DR-UV-SPIV) technique[59] was also implemented to study the in-depth distribution of sub-gap defects. In this technique, the light with above bandgap photon energy is illuminated on the samples under measurement. According to the Beer-Lambert law, the penetration depth of the light varies as a function of absorption coefficient (and wavelength);

$$\text{Penetration depth } (d) = 1/\alpha \tag{7}$$

where α is the absorption coefficient and is related to the wavelength of the light as follows;

$$\alpha = 4\pi K/\lambda \tag{8}$$

where K is the extinction coefficient, and λ is the wavelength of light.

Figure 13(a) represents the above-bandgap illumination photocurrent spectra of the pristine sample whereas Figs. 13(b)-(d) represent the photocurrent spectra with above-bandgap illumination for proton-irradiated samples with different fluences. No substantial change in the spectral signature was observed for proton-irradiated samples with above-bandgap illumination. The wavelength of light was varied by sweeping from 280 nm – 400 nm with the steps of 10 nm. Since the photon energy is higher than the bandgap of the material, all the states in the bandgap are supposed to be photo-ionized. As the wavelength of light is increased, the penetration depth increases so that the in-depth spatial distribution of the in-gap states can be sequentially probed.

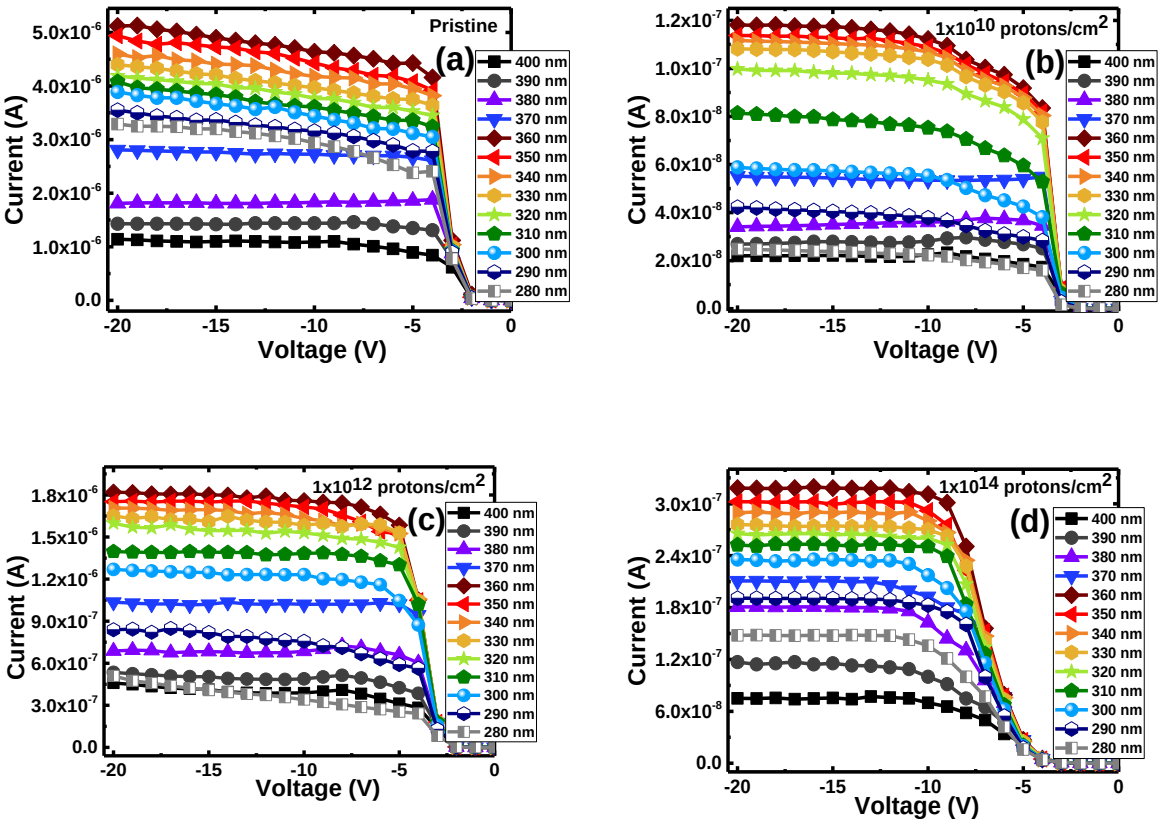

FIG. 13. Spectroscopic photo-IV (absolute) data with above-bandgap illumination of (a) pristine sample; and samples irradiated with fluence of (b) 1×10^{10} protons/cm^2 (c) 1×10^{12} protons/cm^2 and (d) 1×10^{14} protons/cm^2.

The above-bandgap illumination photocurrent spectra normalized with an optical power of the light source is shown in Fig. 14. Each data points of the photocurrent were extracted at -12 V from the data in Fig. 13. It can be observed from these data that the absolute value of photocurrent has decreased.

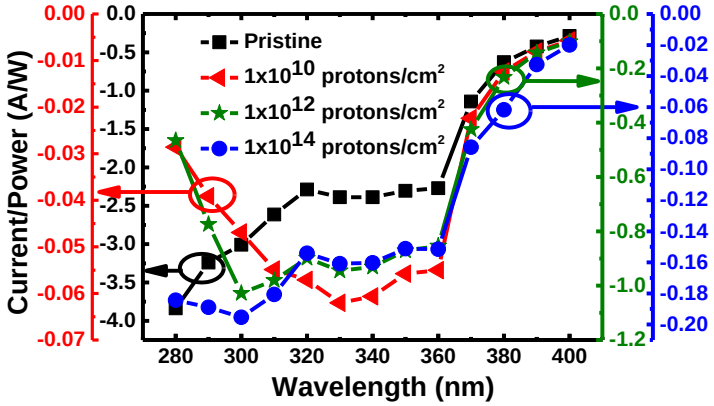

FIG. 14. Normalized photocurrent response with above-bandgap illumination at -12 V bias.

Since there is no change in the spectral distribution of photocurrent, no change in the trap location due to proton irradiation could be speculated. Contrary to the sub-bandgap photo-IV, a reduction in the absolute value of photocurrent was observed, which can be attributed to the quenching of persistent photoconductivity caused by irradiation.[60]

The spectroscopic photo-IV measurement confirms the existence of native sub-gap traps in AlGaN/GaN HEMTs. In addition, protons of 100 keV energy with higher fluences (1×10^{12} and 1×10^{14} protons/cm^2) can result in the generation of additional sub-gap trap centers without compensating or relocating the native sub-gap traps.

IV. SUMMARY AND CONCLUSIONS

The effect of proton irradiation on the materials/device characteristics of the AlGaN/GaN HEMTs was studied. Low-energy proton beam with low to high fluences was used to simulate a

certain aspect of the space environment. The energy of the proton beam was fixed to 100 keV while three different fluences (1×10^{10}, 1×10^{12}, and 1×10^{14} protons/cm^2) were used. The device output characteristics were not affected by the effects of protons on MS junction because the contacts were formed after the epilayer irradiation. The analyzed results from the outcomes of micro-Raman, PL, XRD, XPS, AFM, SEM, conventional transistor characterization, and SPIV experimental techniques were compared between the pristine and proton-irradiated samples. Micro-Raman study suggested the strain relaxation while no observable degradation in the crystal lattice was noticed. A slight increase in surface roughness upon irradiation was detected. Ga-N bonding was not affected due to proton irradiation, and no change in the surface composition of elements was detected by XPS. From the transistor device characteristics, the minimal degradation in drain output current was observed for the irradiated samples with lower fluence whereas the degradation was more intense for the irradiated samples with higher fluences. A large reduction in mobility was observed upon proton irradiation. Coulomb scattering from charged defects, introduced by protons, was accounted responsible for carrier mobility reduction in the irradiated devices. The 2DEG sheet carrier density and the bulk carrier concentration decreased after irradiation of a proton with a fluence of 1×10^{10} protons/cm^2 but increased for 1×10^{12}, and 1×10^{14} protons/cm^2 fluences. This change in carrier density is attributed to a decrease in irradiation-induced strain relaxation and the effect of protons on migration and recombination of mobile defects. Also, the direction of the threshold voltage shift was found to be consistent with the changes in carrier density.

Additionally, we performed a trap analysis of proton irradiated HEMTs using our unique and novel technique for trap characterization, SPIV. From this analysis, the pre-existence of sub-gap defects on the pristine samples were detected, and the introduction of new traps due to proton-

irradiation was confirmed. Also, the proton irradiation did not affect the trap states of the in-gap region. The SPIV analysis has indicated the possible migration and recombination of mobile defects upon proton irradiation. The fluence dependent effects of 100 keV protons on the threshold voltage shift, carrier concentration, trap distribution, dc performance and the strain states of AlGaN/GaN HEMTs were investigated using different experimental techniques, and detailed analysis was presented. The maximum distribution of 100 keV protons was located deeper than the thin 2DEG layer, introducing high defect concentration in a region relatively far from the 2DEG. This led to a relatively less degradation on the electrical performance of the HEMTs devices. Based on these results, it can be concluded that AlGaN/GaN HEMTs have high endurance for exposure to the relatively high fluence of the low-energy proton beam, which makes the device suitable for the space applications.

ACKNOWLEDGMENTS

The project was funded by Walter Professorship. The authors thank Mr. Naresh Shahi for SEM measurements, Mr. Benjamin Schoenek for AFM measurements and Mr. Max Cichon for proton irradiation. Also, the authors would like to acknowledge Dr. Sarit Dhar for valuable discussions.

References

[1] C. Claeys and E. Simoen, *Radiation Effects in Advanced Semiconductor Materials and Devices* (Springer Science & Business Media, 2013).

[2] J.H. Crawford and L.M. Slifkin, *Point Defects in Solids: Volume 2 Semiconductors and Molecular Crystals* (Plenum Press, New York, 1975).

[3] S.O. Kucheyev, J.S. Williams, J. Zou, C. Jagadish, M. Pophristic, S. Guo, I.T. Ferguson, and M.O. Manasreh, J. Appl. Phys. **92**, 3554 (2002).

[4] A. Johnston, *Reliability and Radiation Effects in Compound Semiconductors* (World Scientific, 2010).

[5] M.P. Khanal, B. Ozden, K. Kim, S. Uprety, V. Mirkhani, K. Yapabandara, A.C. Ahyi, and M. Park, J. Vac. Sci. Technol. B **35**, 03D107 (2017).

[6] B.D. Weaver, P.A. Martin, J.B. Boos, and C.D. Cress, IEEE Trans. Nucl. Sci. **59**, 3077 (2012).

[7] J.D. Greenlee, P. Specht, T.J. Anderson, A.D. Koehler, B.D. Weaver, M. Luysberg, O.D. Dubon, F.J. Kub, T.R. Weatherford, and K.D. Hobart, Appl. Phys. Lett. **107**, 083504 (2015).

[8] B.D. White, M. Bataiev, L.J. Brillson, B.K. Choi, D.M. Fleetwood, R.D. Schrimpf, S.I. Pantelides, R.W. Dettmer, W.J. Schaff, J.G. Champlain, and A.K. Mishra, IEEE Trans. Nucl. Sci. **49**, 2695 (2002).

[9] S.J. Cai, Y.S. Tang, R. Li, Y.Y. Wei, L. Wong, Y.L. Chen, K.L. Wang, M. Chen, R.D. Schrimpf, J.C. Keay, and K.F. Galloway, IEEE Trans. Electron Devices **47**, 304 (2000).

[10] B. Luo, J.W. Johnson, F. Ren, K.K. Allums, C.R. Abernathy, S.J. Pearton, R. Dwivedi, T.N. Fogarty, R. Wilkins, A.M. Dabiran, A.M. Wowchack, C.J. Polley, P.P. Chow, and A.G. Baca, Appl. Phys. Lett. **79**, 2196 (2001).

[11] B. Luo, J.W. Johnson, F. Ren, K.K. Allums, C.R. Abernathy, S.J. Pearton, R. Dwivedi, T.N. Fogarty, R. Wilkins, A.M. Dabiran, A.M. Wowchack, C.J. Polley, P.P. Chow, and A.G. Baca, J. Electron. Mater. **31**, 437 (2002).

[12] A.Y. Polyakov, A.S. Usikov, B. Theys, N.B. Smirnov, A.V. Govorkov, F. Jomard, N.M. Shmidt, and W.V. Lundin, Solid-State Electron. **44**, 1971 (2000).

[13] N. Chandrasekaran, T. Soga, Y. Inuzuka, H. Taguchi, M. Imaizumi, T. Ohshima, and T. Jimbo, Jpn. J. Appl. Phys. **43**, L1302 (2004).

[14] H.J. Schaefer, J Aerosp Med **30**, 631 (1959).

[15] W.F. Hilton, in *Space Flight Re-Entry Trajectories* (Springer, Vienna, 1962), pp. 325–333.

[16] R.P. Lin, C.-I. Meng, and K.A. Anderson, J. Geophys. Res. **79**, 489 (1974).

[17] T. Terasawa, Planet. Space Sci. **27**, 365 (1979).

[18] W. Rong, G. Zengliang, Z. Xinghui, and Z. Zuoxu, Sol. Energy Mater. Sol. Cells **77**, 351 (2003).

[19] F. Tong, K. Yapabandara, C.- Yang, M. Khanal, C. Jiao, M. Goforth, B. Ozden, A. Ahyi, M. Hamilton, G. Niu, D.A. Ewoldt, G. Chung, and M. Park, Electron. Lett. **49**, 1547 (2013).

[20] A.D. Koehler, P. Specht, T.J. Anderson, B.D. Weaver, J.D. Greenlee, M.J. Tadjer, M. Porter, M. Wade, O.C. Dubon, K.D. Hobart, T.R. Weatherford, and F.J. Kub, IEEE Electron Device Lett. **35**, 1194 (2014).

[21] J.F. Ziegler, M.D. Ziegler, and J.P. Biersack, Nucl. Instrum. Methods Phys. Res. Sect. B Beam Interact. Mater. At. **268**, 1818 (2010).

[22] H. Harima, J. Phys. Condens. Matter **14**, R967 (2002).

[23] G. Irmer, C. Röder, C. Himcinschi, and J. Kortus, J. Appl. Phys. **116**, 245702 (2014).

[24] A.M. Kurakin, S.A. Vitusevich, S.V. Danylyuk, H. Hardtdegen, N. Klein, Z. Bougrioua, B.A. Danilchenko, R.V. Konakova, and A.E. Belyaev, J. Appl. Phys. **103**, 083707 (2008).

[25] M.J. Matthews, J.W.P. Hsu, S. Gu, and T.F. Kuech, Appl. Phys. Lett. **79**, 3086 (2001).

[26] J.-Y. Lu, Z.-J. Wang, D.-M. Deng, Y. Wang, K.J. Chen, K.-M. Lau, and T.-Y. Zhang, J. Appl. Phys. **108**, 123520 (2010).

[27] J.A. Freitas, W.J. Moore, B.V. Shanabrook, G.C.B. Braga, S.K. Lee, S.S. Park, and J.Y. Han, Phys. Rev. B **66**, 233311 (2002).

[28] C.H. Seager, A.F. Wright, J. Yu, and W. Götz, J. Appl. Phys. **92**, 6553 (2002).

[29] M.A. Reshchikov and H. Morkoç, J. Appl. Phys. **97**, 061301 (2005).

[30] M.A. Reshchikov, F. Shahedipour, R.Y. Korotkov, B.W. Wessels, and M.P. Ulmer, J. Appl. Phys. **87**, 3351 (2000).

[31] M. Albrecht, H.P. Strunk, J.L. Weyher, I. Grzegory, S. Porowski, and T. Wosinski, J. Appl. Phys. **92**, 2000 (2002).

[32] L. Lü, Y. Hao, X. Zheng, J. Zhang, S. Xu, Z. Lin, S. Ai, and F. Meng, Sci. China Technol. Sci. **55**, 2432 (2012).

[33] H.-P. Lee, J. Perozek, L.D. Rosario, and C. Bayram, Sci. Rep. **6**, 37588 (2016).

[34] S.I. Bahn, C.M. Lee, S.J. Lee, J.I. Lee, C.S. Kim, S.K. Noh, B.S. Oh, and K.J. Kim, J. Korean Phys. Soc. **43**, 381 (2003).

[35] S.J. Pearton, Mater. Sci. Rep. **4**, 313 (1990).

[36] P. Arivazhagan, R. Ramesh, M. Balaji, K. Asokan, and K. Baskar, J. Alloys Compd. **679**, 94 (2016).

[37] W.R.L. Lambrecht, B. Segall, S. Strite, G. Martin, A. Agarwal, H. Morkoç, and A. Rockett, Phys. Rev. B **50**, 14155 (1994).

[38] V. Thakur and S.M. Shivaprasad, Appl. Surf. Sci. **327**, 389 (2015).

[39] V.V. Emtsev, E.E. Zavarin, M.A. Kozlovskii, M.F. Kudoyarov, V.V. Lundin, G.A. Oganesyan, V.N. Petrov, D.S. Poloskin, A.V. Sakharov, S.I. Troshkov, N.M. Shmidt, V.N. V'yuginov, A.A. Zybin, Y.M. Parnes, S.I. Vidyakin, A.G. Gudkov, A.E. Chernyakov, and V.V. Kozlovskii, Tech. Phys. Lett. **42**, 1079 (2016).

[40] X. Hu, A.P. Karmarkar, B. Jun, D.M. Fleetwood, R.D. Schrimpf, R.D. Geil, R.A. Weller, B.D. White, M. Bataiev, L.J. Brillson, and U.K. Mishra, IEEE Trans. Nucl. Sci. **50**, 1791 (2003).

[41] B.-J. Kim, S. Ahn, F. Ren, S.J. Pearton, G. Yang, and J. Kim, J. Vac. Sci. Technol. B **34**, 041231 (2016).

[42] L. Lv, J.G. Ma, Y.R. Cao, J.C. Zhang, W. Zhang, L. Li, S.R. Xu, X.H. Ma, X.T. Ren, and Y. Hao, Microelectron. Reliab. **51**, 2168 (2011).

[43] X. Wan, O.K. Baker, M.W. McCurdy, E.X. Zhang, M. Zafrani, S.P. Wainwright, J. Xu, H.L. Bo, R.A. Reed, D.M. Fleetwood, and T.P. Ma, IEEE Trans. Nucl. Sci. **64**, 253 (2017).

[44] N.E. Ives, J. Chen, A.F. Witulski, R.D. Schrimpf, D.M. Fleetwood, R.W. Bruce, M.W. McCurdy, E.X. Zhang, and L.W. Massengill, IEEE Trans. Nucl. Sci. **62**, 2417 (2015).

[45] C.F. Lo, L. Liu, F. Ren, H.-Y. Kim, J. Kim, S.J. Pearton, O. Laboutin, Y. Cao, J.W. Johnson, and I.I. Kravchenko, J. Vac. Sci. Technol. B Nanotechnol. Microelectron. Mater. Process. Meas. Phenom. **29**, 061201 (2011).

[46] P. Roblin and H. Rohdin, *High-Speed Heterostructure Devices: From Device Concepts to Circuit Modeling* (Cambridge University Press, 2002).

[47] I.H. Lee, C. Lee, B.K. Choi, Y. Yun, Y.J. Chang, and S.Y. Jang, J. Korean Phys. Soc. **72**, 920 (2018).

[48] E.H. Steenbergen, J.A. Massengale, V.M. Cowan, Z. Lin, Y.-H. Zhang, and C.P. Morath, in *Nanophotonics Macrophotonics Space Environ. VII* (International Society for Optics and Photonics, 2013), p. 887609.

[49] T. Roy, E.X. Zhang, Y.S. Puzyrev, D.M. Fleetwood, R.D. Schrimpf, B.K. Choi, A.B. Hmelo, and S.T. Pantelides, IEEE Trans. Nucl. Sci. **57**, 3060 (2010).

[50] R. Jiang, E.X. Zhang, M.W. McCurdy, J. Chen, X. Shen, P. Wang, D.M. Fleetwood, R.D. Schrimpf, S.W. Kaun, E.C.H. Kyle, J.S. Speck, and S.T. Pantelides, IEEE Trans. Nucl. Sci. **64**, 218 (2017).

[51] S. Li, Y.-H. Hwang, Y.-L. Hsieh, L. Lei, F. Ren, S.J. Pearton, E. Patrick, M.E. Law, C. Velez Cuervo, and D.J. Smith, J. Vac. Sci. Technol. B Nanotechnol. Microelectron. Mater. Process. Meas. Phenom. **32**, 021203 (2014).

[52] B.D. Weaver, T.J. Anderson, A.D. Koehler, J.D. Greenlee, J.K. Hite, D.I. Shahin, F.J. Kub, and K.D. Hobart, ECS J. Solid State Sci. Technol. **5**, Q208 (2016).

[53] A. Gokarna, N.R. Pavaskar, S.D. Sathaye, V. Ganesan, and S.V. Bhoraskar, J. Appl. Phys. **92**, 2118 (2002).

[54] J. Lee, A. Yadav, M. Antia, V. Zaffino, E. Flitsiyan, L. Chernyak, J. Salzman, B. Meyler, S. Ahn, F. Ren, and S.J. Pearton, Radiat. Eff. Defects Solids **172**, 250 (2017).

[55] Rashmi, A. Kranti, S. Haldar, and R.S. Gupta, Microelectron. J. **33**, 205 (2002).

[56] P.B. Klein and S.C. Binari, J. Phys. Condens. Matter **15**, R1641 (2003).

[57] B. Ozden, M.P. Khanal, S. Youn, V. Mirkhani, K. Yapabandara, M. Park, M. Zhao, H. Liang, P.K. Kandaswamy, and Y.N. Saripalli, ECS J. Solid State Sci. Technol. **5**, P3206 (2016).

[58] B. Ozden, M.P. Khanal, V. Mirkhani, K. Yapabandara, C. Yang, S. Ko, S. Youn, M.C. Hamilton, M.H. Sk, A.C. Ahyi, and M. Park, J. Nanosci. Nanotechnol. **16**, 7630 (2016).

[59] B. Ozden, C. Yang, F. Tong, M.P. Khanal, V. Mirkhani, M.H. Sk, A.C. Ahyi, and M. Park, Appl. Phys. Lett. **105**, 172105 (2014).

[60] A. Castaldini, A. Cavallini, and L. Polenta, Phys. Status Solidi A **202**, 2912 (2005).

Chapter 8

Conclusions and Future Work

8.1 Conclusions

The main objective of this dissertation was to identify, characterize, and understand the effects of energetic gamma-rays with cumulative high dose exposure and low energy protons with varying fluences on AlGaN/GaN HEMTs. The key focus of the study was to isolate the effects of those radiations on semiconductor itself from the combined effects coming from the fully constructed devices. For this purpose, the epitaxial layers of HEMTs prior to the construction of the devices were irradiated with the gamma-rays of 120 MRad dose and 100 keV protons with three different fluences of 1×10^{10}, 1×10^{12}, and 1×10^{14} protons/cm^2. The irradiated samples were characterized using a variety of materials characterization techniques, and finally the electronic devices (Schottky and transistor) were constructed to examine the response of material irradiation in their electrical characteristics. The spectroscopic photocurrent-voltage (SPIV) measurement technique was the unique method employed to characterize the irradiation-induced defects in AlGaN/GaN HEMTs. For the comparison of the results, the pristine and irradiated samples (chosen adjacent to each other in the six-inch wafer after dicing) were systematically characterized at ambient conditions, and response data were analyzed.

For the high dose gamma-ray exposed HEMTs devices, electrical characteristics were slightly degraded in comparison to the pristine devices. Gamma-rays caused a reduction in 2DEG carrier density and introduced acceptor-like deep level traps in AlGaN/GaN HEMT wafers. The strain state of the GaN channel layer found to be unaffected after the gamma-ray irradiation. The effect of gamma-rays was also observed in persistent photoconductivity which was quenched on devices fabricated on the irradiated samples. The observation and analysis of Raman spectra

showed that the gamma irradiation could degrade the crystal quality of the HEMTs. High dose gamma-ray irradiation introduced traps and/or re-configured the pre-existing traps, influencing the electrical and optical characteristics of AlGaN/GaN HEMTs. However, based on the observed characteristics and analysis of the results it can be concluded that AlGaN/GaN HEMTs is relatively resistant to high dose (120 MRad) gamma-ray irradiation. This claim can be made by comparing the degradation level in the performance of AlGaN/GaN HEMTs with the existing reports on Si-based MOSFETs (80% degradation) exposed to even lower dose (100 MRad) from ^{60}Co source.[1]

Effects of low energy protons (100 keV) on the materials and device characteristics of the AlGaN/GaN HEMTs were analyzed. A low-energy and low to high-fluences protons were used to simulate a certain aspect of the space environment. Detailed comparative analysis of the material and device characteristics from pristine and proton irradiated samples were made prior to and after the construction of the devices. The overall quality of the HEMTs crystal remained unaffected after the proton irradiation. However, from the micro-Raman study, the relaxation in the strain state of the epitaxial layer could be claimed. Regardless of the fluences, low energy proton beam did not affect the Ga-N bonding in the crystal and did not change the abundance of surface elemental composition. However, the surface roughness was increased upon irradiation. Transistor device characteristics were degraded for devices constructed on irradiated epitaxial HEMTs layers. The drain output current was degraded by just about 27% for the irradiated samples with lower fluence whereas the degradation was more intense for the irradiated samples with higher fluences (for 1×10^{12}: 45% and 1×10^{14}: 43%). The calculated result showed a large reduction in mobility after the proton irradiation. The 2DEG sheet carrier density and the bulk carrier concentration decreased after irradiation of the proton with a fluence of 1×10^{10} protons/cm^2 but increased for the 1×10^{12}, and 1×10^{14} protons/cm^2 fluences. These changes were caused possibly in response to the

decrease in dislocation density and the irradiation-induced strain relaxation. The shift in threshold voltage was dependent on the fluence and was consistent with the corresponding variation in the carrier density.

SPIV measurements and analysis of the results revealed the pre-existence of sub-gap defects on the pristine samples, and also the introduction of new traps due to the proton irradiation was confirmed. Additionally, the proton irradiation did not affect the trap states of the in-gap region. In AlGaN/GaN HEMTs, possible migration and recombination of mobile defects upon proton irradiation could be confirmed with the help of SPIV technique. Therefore, fluence dependent effects of 100 keV protons on the material characteristics and dc performance as well as the defect states of AlGaN/GaN HEMTs were investigated using a variety of experimental techniques, and detailed analysis was performed. Based on the energy and fluence exposed to and the level of performance of the irradiated HEMTs devices in reference to the pristine ones, it can be suggested that the AlGaN/GaN HEMTs have high endurance for exposure to the relatively high fluence of the low-energy proton beam.

From SPIV measurements we observed two types of defects with different activation energies, one with ~1.91 eV (650 nm) on the pristine samples used for gamma-ray irradiation and another with ~1.77 eV (700 nm) on the gamma-ray irradiated samples. Also, the activation energies of defects were estimated to be ~1.77 eV on both the pristine and irradiated samples used for proton irradiation study. Therefore, the activation energies of defects introduced by gamma-ray irradiation and proton irradiation were common. It is believed that the defects with the energy level ~1.91 eV is due to the deep level defects and arise by a transition from a donor charge-transfer level to the conduction band.[2] Similarly, the defects having energy level ~1.77 eV is likely an efficient generation-recombination center for 2DEG carriers.[3]

Overall, AlGaN/GaN HEMTs have shown their potentials to be considered as a viable candidate for the electronic applications in harsh radiation environments from the testing of both types: ionizing and non-ionizing types of radiations. The results of this dissertation work can be useful to the scientific community to explore the potential applications of AlGaN/GaN HEMTs for space military and other civilian applications requiring radiation hard electronics.

8.2 Future Work

As an extension of this dissertation work, two clear paths can be suggested for future work. First, we employed SPIV technique to characterize the proton and gamma-ray induced defects but we limited our characterization to only Schottky devices. Transistor devices can also be tested using a modified version of the system to observe the response in drain current. In addition, we have added additional components to the system so that it is capable of measuring spectroscopic photo-capacitance voltage (SPCV) of the devices. Measuring SPCV will deliver much more useful information regarding the charge states of the defects.

Second, as it is well known, there are different types of energetic particles in the space and other radiation environments, and they influence the device characteristics in different ways and impose different types of defects. So, applying the SPIV and SPCV techniques, it can be suggested that comparative study can be performed on the same material with different types of particle irradiation (such as electron, neutron, proton, gamma, alpha) and defects can be quantified. Also, it is worth mentioning that during the fabrication of transistor devices, annealing was unavoidable. Therefore, irradiated wafers were annealed at 850 ^{o}C during transistor fabrication while the diodes used for SPIV measurements were not annealed. So, some of the device response may not correspond to the same conditions. In future, irradiated wafers without devices can be annealed before fabricating the Schottky contacts.

References

[1] Pushpa, N., K. C. Praveen, AP Gnana Prakash, YP Prabhakara Rao, Ambuj Tripati, G. Govindaraj, and D. Revannasiddaiah. "A comparison of 48 MeV Li3+ ion, 100 MeV F8+ ion and Co-60 gamma irradiation effect on N-channel MOSFETs." *Nuclear Instruments and Methods in Physics Research Section A: Accelerators, Spectrometers, Detectors and Associated Equipment* 613, no. 2 (2010): 280-289.

[2] Chung, S. J., M. S. Jeong, O. H. Cha, C-H. Hong, E-K. Suh, H. J. Lee, Y. S. Kim, and B. H. Kim. "Optical absorption and anomalous photoconductivity in undoped n-type GaN." *Applied Physics Letters* 76, no. 8 (2000): 1021-1023.

[3] Nakano, Yoshitaka, Yoshihiro Irokawa, and Masaki Takeguchi. "Deep-level optical spectroscopy investigation of band gap states in AlGaN/GaN hetero-interfaces." *Applied physics express* 1, no. 9 (2008): 091101.